GROWTH AND GUIDANCE: A STUDY OF NEURON MORPHOLOGY AND HOW IT IS MODIFIED BY FRACTAL AND EUCLIDEAN ELECTRODES *IN VITRO*.

by

CONOR TYE ROWLAND

A DISSERTATION

Presented to the Department of Physics
and the Division of Graduate Studies of the University of Oregon
in partial fulfillment of the requirements
for the degree of
Doctor of Philosophy

March 2023

DISSERTATION APPROVAL PAGE

Student: Conor Tye Rowland

Title: Growth and Guidance: A Study of Neuron Morphology and How it is Modified by Fractal and Euclidean Electrodes *In Vitro*.

This dissertation has been accepted and approved in partial fulfillment of the requirements for the Doctor of Philosophy degree in the Department of Physics by:

Raghuveer Parthasarathy, PhD	Chairperson
Richard Taylor, PhD	Advisor
Jayanth Banavar, PhD	Core Member
Cris Niell, PhD	Institutional Representative

and

Krista Chronister, PhD	Vice Provost for Graduate Studies

Original approval signatures are on file with the University of Oregon Division of Graduate Studies.

Degree awarded March 2023

DISSERTATION ABSTRACT

Conor Tye Rowland

Doctor of Philosophy

Department of Physics

March 2023

Title: Growth and Guidance: A Study of Neuron Morphology and How it is Modified by Fractal and Euclidean Electrodes *In Vitro*.

For well over a century, neuroscientists have been studying the inherent ties between neuronal morphology and functionality. Santiago Ramón y Cajal, in his work that ultimately awarded him a Nobel Prize in 1906, established that neurons function as the fundamental unit of the nervous system. Ramón y Cajal himself recognized the relationship between neuronal form and function by proposing the wiring economy principle, which states that the nervous system's complex network of neurons is efficiently wired in a way that minimizes wiring length. The research within this dissertation works towards the goal of optimizing the design of the electrode-neuron interface of medical implants by building upon Ramón y Cajal's foundational ideas and integrating them with the techniques of fractal analysis.

The dissertation begins by addressing the question of how electrode geometry impacts the morphology of the networks of neurons and glia interfacing with the electrode. This was done by interacting dissociated mouse retinal cell cultures *in vitro* with vertically aligned carbon nanotube (VACNT) electrodes grown on a silicon dioxide (SiO_2) substrate and patterned into Euclidean and fractal geometries. The VACNT-SiO_2 material system was shown to perform exceptionally well at guiding neurons onto the VACNTs and glia onto the surrounding SiO_2. Furthermore, the electrode geometries that performed the best at supporting a healthy network of neurons and glia were those that balanced providing a large VACNT electrode area with maintaining connectedness in the surrounding SiO_2 surface and allowing it to interpenetrate the VACNT electrode.

Following these *in vitro* experiments, three-dimensional models of pyramidal neurons from the CA1 region of the rat hippocampus were reconstructed using confocal microscopy. The fractal properties of the neurons and how these relate to their functionality were then analyzed. It was then demonstrated that the natural, fractal behavior of the neurons, though limited in its scaling range, was sufficient to provide the neurons with an optimal balance between connectivity and building and operating costs.

The dissertation concludes by reviewing the results of these studies, providing directions for future work, and discussing the implications regarding electrode design.

This dissertation includes previously published co-authored material.

CURRICULUM VITAE

NAME OF AUTHOR: Conor Tye Rowland

GRADUATE AND UNDERGRADUATE SCHOOLS ATTENDED:

University of Oregon, Eugene
California State Polytechnic University, Pomona

DEGREES AWARDED:

Doctor of Philosophy, Physics, 2023, University of Oregon
Bachelor of Science, Physics, 2015, California State Polytechnic University

AREAS OF SPECIAL INTEREST:

Fractal Geometry
Fractal Analysis
Neuromorphology
Neural Interfaces
Nanofabrication
Architectural Design

PROFESSIONAL EXPERIENCE:

Graduate Research Assistant, University of Oregon, Eugene, OR (2017-2023)
Graduate Teaching Fellow, University of Oregon, Eugene, OR (2015-2017)
Consultant, Fractals Research LLC, Eugene, OR (2018-2021)

GRANTS, AWARDS, AND HONORS:

Architectural Product of the Year Award (USA, 2019)
Gold in the Nightingale Awards Competition (Healthcare Design Expo, USA, 2019)
Buildings Merit Innovation Award (USA, 2019)
The Interior Design HiP Award (USA, 2019)
The NeoCon Best of Show Innovation Award (USA, 2019)
The Metropolis NYC-DESIGN Award (USA, 2019)
Honorary Interior Design NYC-DESIGN Award (USA, 2019)

PUBLICATIONS:

C. Rowland, J. H. Smith, S. Moslehi, B. Harland, J. Dalrymple-Alford, and R. P. Taylor. Neuron arbor geometry is sensitive to the limited-range fractal properties of their dendrites. *Front Netw Physiol* **3**, (2023).

S. Moslehi, C. Rowland, J. H. Smith, W. Griffiths, W. J. Watterson, C. M. Niell, B. J. Alemán, M.-T. Perez, and R. P. Taylor. Comparison of fractal and grid electrodes for studying the effects of spatial confinement on dissociated retinal neuronal and glial behavior. *Sci Rep* **12**, 17513 (2022).

C. Rowland, B. Harland, J. H. Smith, S. Moslehi, J. Dalrymple-Alford, and R. P. Taylor. Investigating Fractal Analysis as a Diagnostic Tool That Probes the Connectivity of Hippocampal Neurons. *Front Physiol* **13**, 932598 (2022).

S. Moslehi, C. Rowland, J. H. Smith, W. J. Watterson, D. Miller, C. M. Niell, B. J. Alemán, M.-T. Perez, and R. P. Taylor. Controlled assembly of retinal cells on fractal and Euclidean electrodes. *PLOS ONE* **17**, e0265685 (2022).

K. E. Robles, M. Roberts, C. Viengkham, J. H. Smith, C. Rowland, S. Moslehi, S. Stadlober, A. Lesjak, M. Lesjak, R. P. Taylor, B. Spehar, and M. E. Sereno. Aesthetics and Psychological Effects of Fractal Based Design. *Front Psychol* **12**, 3413 (2021).

J. H. Smith, C. Rowland, B. Harland, S. Moslehi, R. D. Montgomery, K. Schobert, W. J. Watterson, J. Dalrymple-Alford, and R. P. Taylor. How neurons exploit fractal geometry to optimize their network connectivity. *Sci Rep* **11**, 2332 (2021).

S. Moslehi, W. J. Watterson, C. Rowland, J. H. Smith, M.-T. Perez, and R. P. Taylor. Physical Guidance of Cultured Retinal Neurons Using Zig-zag Surface Patterns. *Am J Biomed Sci & Res* **11**, 3 (2020).

W. J. Watterson, S. Moslehi, C. Rowland, K. M. Zappitelli, J. H. Smith, D. Miller, J. E. Chouinard, S. L. Golledge, R. P. Taylor, M.-T. Perez, and B. J. Alemán. The Roles of an Aluminum Underlayer in the Biocompatibility and Mechanical Integrity of Vertically Aligned Carbon Nanotubes for Interfacing with Retinal Neurons. *Micromachines* **11**, 546 (2020).

J. Smith, C. Rowland, S. Moslehi, R. Taylor, A. Lesjak, M. Lesjak, S. Stadlober, L. Lee, J. Dettmar, M. Page, and J. Himes. Relaxing Floors: Fractal Fluency in the Built Environment. *Nonlinear Dynamics Psychol Life Sci* **24**, 127–141 (2020).

ACKNOWLEDGMENTS

All that I have accomplished in my life would not have been possible without the unwavering love and support of my parents, Michelle Morales and James Rowland. Your efforts nurturing me throughout all phases of my life will never go unappreciated. To my brother, Cameron Rowland, I will always cherish the bond that we share. While we inevitably butted heads growing up together, these battles were necessary for us to develop and become the men we are today. And hey, without the memories of some of our more tense moments, I wouldn't be able to as deeply appreciate the brotherly love that we now share. To the rest of my extended family, I am thankful for all of your support however near or far you may have been from me in my life.

Of course, in addition to my family, a great number of beautiful people have supported me over the years. I couldn't have survived the trials and tribulations of being a student without the support of my fellow students, colleagues, and mentors alike. To my advisor, Richard Taylor, I am incredibly grateful for all that you have done to support me. Your humor, kindness, tenacity, ingenuity, and guidance have been invaluable in helping me develop both as a scientist and as a person. I would also like to thank my labmates, Saba Moslehi, Julian Smith, Willem Griffiths, and William Watterson. Each of you, in your own individual way, have helped me become a better scientist and made the process of conducting research a more exciting and enlightening one. To the members of my committee, Raghuveer Parthasarathy, Jayanth Banavar, and Cris Niell, I am thankful for your guidance and illuminating discussions as I worked towards completing the research presented in this dissertation.

Lastly, to all the friends that I have made and had the great pleasure of sharing a slice

of spacetime with, your presence has enriched my life and helped me keep hold of my sanity through thick and thin. There are too many of you to name you all here, but I know who you are and I’m certain that you do too. Thank you for everything you’ve done to bring such precious friendships to my life.

The research in this dissertation was funded by the W.M. Keck Foundation, the Living Legacy Foundation, the Ciminelli Foundation, and the Linde Martin Institute.

TABLE OF CONTENTS

LIST OF FIGURES

Figure Page

Figure Page

LIST OF TABLES

Table Page

CHAPTER I

INTRODUCTION

Ever since humans discovered the ability to generate and control electricity, inquiring scientists have been investigating its effects on the body. All the way back in 1755, French physician Charles LeRoy caused a blind patient to perceive flashes of light by sending current through a wire wrapped around the patient's head. Following this in 1791, Luigi Galvani, an Italian physician, laid the foundations of electrophysiology by causing the leg of a frog to contract as current was sent through a bimetallic arc contacting two points on a nerve passing through the leg[1]. Moving forward to the modern day, implants meant to interface with the nervous system have been the focus of broad interdisciplinary research. The functionality of these implants includes stimulating electrical signals in the body's neurons and sensing the signals that are naturally flowing through the neurons. For example, electronic devices have been implanted into human retinas with the aim of restoring vision to patients with degenerative retinal diseases[2–9]. Additionally, more than 150,000 deep brain stimulation implant surgeries have been performed targeting neurological disorders such as Parkinson's disease[10].

While studying the response of neurons to the introduction of implants can lead to enhancements in the performance of medical devices, it also provides information about their fundamental behavior and the degree to which this behavior can be controlled. Such studies should also accommodate interactions with glia, which are prevalent throughout the nervous system[11]. Although neurons and glia were discovered around the same time, research of the latter has been slower to gain momentum[12] even though they play central roles in controlling neuronal network structure and functionality[13]. Specifically, whereas neurons are crucial for carrying the body's electrical signals, glia are equally crucial because of their supporting role as the neurons' life support system. As such, studies examining interactions between implants and neurons without the inclusion of glia may suffer from providing an incomplete understanding of the neurons' natural behavior.

Significantly, implants are frequently referred to as bionic devices in recognition of the importance of bio-inspiration and the need for biocompatibility at the cell-implant interface ('bio' is Greek for 'life'). Regardless of its application, an implant's operation must be sustainable in terms of toxicity, durability, and efficiency. The factors that ensure biocompatibility can be pictured as three legs of a stool, with each leg playing a vital role for stability. The two legs that have received the most attention by researchers are the chemical environment and physical textures established by the implant surface as it interacts with the body. The third leg is the shape of an implant's electrodes and is tied to the central focus of this dissertation. The stimulating electrodes used in conventional implants feature Euclidean geometries like squares, hexagons, and circles, which are fundamentally different to the complex, fractal geometry adopted by neurons that has seen ongoing study for several decades[14]. Motivated by the principle of bio-inspiration, this dissertation provides a study of the morphology of neurons and the impact that fractal and Euclidean electrode geometries have on this morphology. With this aim in mind, it's informative to briefly examine how fractal geometry has been applied to better understand the behavior of other natural systems.

The term 'fractal' was introduced in 1975 by Benoit Mandelbrot to highlight similarities between a diverse range of natural systems and the scale invariant properties of mathematical patterns researched over the previous century[15,16]. Immediately after Mandelbrot introduced the world to the field of fractal geometry, an ever-growing body of research formed that details the fractal scaling properties of a plethora of natural systems. Due to the diversity of morphological complexity across neuron types, fractal analysis has seen successful application as a tool for the classification of neurons[17–22]. In addition to neurons, the apparent ubiquity of fractals in nature has been observed in systems across a vast range of sizes. From the smallest to the largest systems in the universe, fractal scaling properties are abundant. Some commonly cited examples of natural fractals include trees[23], rivers[24], coastlines[25], mountains[26], clouds[27], lightning[28], and snowflakes[29], but the list certainly doesn't end there. Fractal scaling has also been observed in the texture of magnetic domains[30], magnetic monopole excitation dynamics in spin ice[31], nanoparticle aggregation[32], the folding of DNA globules[33], gene expression dynamics[34], ion channel kinetics[35], the growth of bacterial colonies[36], the vasculature of the retina[37], the bronchial tree of the lungs[38], heartbeat[39] and neuronal spike train[40] dynamics, the structure of the cerebellum[41], the folds of the brain's cortical surface[42], graphs of cortical functional connectivity networks[43], the foraging behavior of animals[44], the dynamics of rainfall[45], wind speed[46], and ocean currents[47], the edges of Saturn's rings[48], and the structure of supernovae remnants[49], clouds in the interstellar medium[50], and the cosmic web[51].

Given the prevalence of fractal scaling behavior in natural systems, it's critical to ask what might be driving this. Is there an inherent functional benefit associated with fractal scaling in biological systems? What physical mechanisms are at play in non-biological systems that give rise to fractal scaling? The answer, of course, varies depending on the system of interest. The fractal structure of clouds has been shown to result from turbulent diffusion[52]. Similarly, for clouds in the interstellar medium, magnetohydrodynamic turbulence has been linked to their fractal structure[53]. The intricate, highly ramified branches of fractal river basins has been shown to arise from a global minimization of energy expenditure[54]. The jagged, highly irregular morphology of fractal coastlines has been shown to naturally form over time due to their ability to minimize the eroding power of the ocean[55]. Turning to biological systems, the fractal structure of trees has been tied to their growth rate and ability to efficiently capture light[56]. The lung's fractal structure maximizes its gas-exchange surface area and allows it to optimally adapt to a variety of physiological conditions[57]. The fractal structure of the brain's connectivity networks have been shown to provide a balance between maximizing information transfer while minimizing wiring costs[58]. The densely packed, fractal folding of DNA globules benefit from being largely unknotted, allowing parts of the globule to rapidly unfold and become available for transcription[59].

Recognizing the power of fractal geometry to characterize the behavior of so many natural systems, it straightforwardly follows to question whether interactions of neurons with the artificial electrode surfaces of an implant would benefit from matching the electrode design to the natural, fractal properties of the neurons. Should this proposed matching allow the neurons growing on the electrode surfaces to flourish, the effect can be thought of as a kind of ‘fractal resonance’. While a diverse range of studies have demonstrated the impact of patterning on the behavior of neurons and glia[60–71], these patterning strategies have not included fractal designs. Consequently, these studies investigate neuronal and glial behavior on surfaces patterned into geometries distinctly dissimilar to the geometry adopted by neurons and glia, potentially forcing them away from their natural behavior. Addressing the absence of studies that test fractal designs, the experiments described in this dissertation work towards testing the ‘fractal resonance’ hypothesis.

Following a brief review in chapter II of the relevant background information that forms a basis for understanding and motivating the experiments detailed in this dissertation, chapter III describes experiments that investigated the morphology of the network of neurons and glia that formed on electrodes patterned into the relatively simple H-Tree fractal as well as the Euclidean geometries of rows of lines and a uniform grid. Capitalizing on the H-Tree fractal’s multi-scaled branches, ranging in size from tens of microns to several millimeters, neuronal and glial interactions with an electrode are examined ranging from the individual cell scale to the network scale. Vertically aligned carbon nanotubes are employed as the electrode material due to their biocompatibility and beneficial physical texture. By using *in vitro* co-cultures of neurons and glia, the ‘herding’ of these cells is demonstrated whereby neurons predominately adhere to the electrodes and glia to the gaps surrounding the electrodes. This novel self-assembly prevents glia from dominating the electrode-neuron interface but still allows them to maintain close enough proximity to the neurons on the electrode to continue acting as their life-support system.

Having successfully demonstrated the guidance of neurons to the electrode interface, would growth be enhanced on an electrode that is patterned into a bio-inspired design matching the precise fractal characteristics of the neurons, thereby demonstrating ‘fractal resonance’? To appropriately achieve this however, the precise fractal characteristics of the neuron must first be determined. Although the H-Tree fractal benefits from relative simplicity, it isn’t bio-inspired because its fractal characteristics are distinctly different to those of a neuron. Chapter IV describes experiments that aid the move towards bio-inspired fractal electrodes by investigating the relationship between the fractal properties of neurons and their functionality. Using confocal microscopy to create three-dimensional reconstructions of pyramidal neurons from the CA1 region of the rat hippocampus, the fractality of these neurons is determined to originate from a combination of the scaling of their branch lengths and the forking and weaving behavior of their branches. Distorted versions of these neurons are created to examine the consequences of deviating away from the natural fractal form. It is found that such distortions cause the neurons to deviate away from an optimal balance of connectivity with respect to building and operational costs. Regarding the application of neurons interfacing with the electrode surface of an implant, deviations from this optimal balance are hypothesized to suppress growth.

In chapter V, this dissertation concludes with a review of the conclusions drawn from the experiments detailed in chapters III and IV and provides suggestions for directions forward regarding future experiments that can further test the models of cell behavior presented here. For example, techniques are suggested that can further examine neuronal and glial behavior by quantifying their network topography, distinguishing between different cell types, and identifying neuron-electrode anchor points. Additionally, preliminary results from studies extending the connectivity-cost optimization model developed in chapter IV to retinal bipolar neurons are presented and implications for how this informs electrode designs meant to test the ‘fractal resonance’ hypothesis are discussed.

The work presented throughout chapters III and IV of this dissertation would not have been possible without the combined efforts of my collaborators, for which I am very thankful. The work presented within chapter III has been adapted from previously published co-authored work by Saba Moslehi (SM), Conor Rowland (CR), Julian H. Smith (JHS), William J. Watterson (WJW), David Miller (DM), Cris M. Niell (CMN), Benjamín J. Alemán (BJA), Maria-Thereza Perez (MTP), and Richard P. Taylor (RPT) in *Controlled assembly of retinal cells on fractal and Euclidean electrodes*, PLOS ONE **17**, e0265685 (2022) and by SM, CR, JHS, Willem Griffiths (WG), WJW, CMN, BJA, MTP, and RPT in *Comparison of fractal and grid electrodes for studying the effects of spatial confinement on dissociated retinal neuronal and glial behavior*, Scientific Reports **12**, 17513 (2022). My contributions to the above publications include fabricating VACNT electrodes, developing methods to analyze neuronal and glial cell behavior, and performing retinal cell cultures, immunocytochemistry, fluorescence microscopy, and image analysis. I would like to thank SM, WJW, DM, and BJA for their work developing the VACNT synthesis process. I would like to thank MTP for her work providing retinal cell culture and immunocytochemistry protocols. I would like to thank SM for her contributions to fabricating VACNT electrodes. I would like to thank SM and JHS for their contributions to performing retinal cell cultures, immunocytochemistry, and fluorescence microscopy. I would like to thank SM, WJW, and JHS for their contributions to developing methods to analyze neuronal and glial cell behavior. Finally, I would like to thank SM, JHS, and WG for their contributions to performing image analysis.

The work presented within chapter IV has been adapted from previously published co-authored work by JHS, CR, Bruce Harland (BH), SM, Rick D. Montgomery (RDM), Kristofer Schobert (KS), WJW, John Dalrymple-Alford (JDA), and RPT in *How neurons exploit fractal geometry to optimize their network connectivity*, Scientific Reports **11**, 2332 (2021), by CR, BH, JHS, SM, JDA, and RPT in *Investigating Fractal Analysis as a Diagnostic Tool That Probes the Connectivity of Hippocampal Neurons*, Frontiers in Physiology **13**, 932598 (2022), and by CR, JHS, SM, BH, JDA, and RPT in *Neuron Arbor Geometry is Sensitive to the Limited-Range Fractal Properties of their Dendrites* Frontiers in Network Physiology **3**, 1072815 (2023). My contributions to the above publications include developing methods to analyze the morphological properties of neurons, quantifying parameters related to neuron functionality, generating statistical H-Tree models, and developing the connectivity-cost optimization model. I would like to thank BH and JDA for their work managing animal husbandry and creating neuron reconstructions. I would like to thank JHS for his work developing methods for distorting neuron reconstructions. Finally, I would like to thank SM, RDM, and KS for their contributions to developing methods to analyze the morphological properties of neurons and quantify parameters related to neuron functionality.

CHAPTER II

BACKGROUND

Neuronal Morphology and Functionality

Following Santiago Ramón y Cajal's groundbreaking research that included beautiful illustrations of the complex morphology of neurons[72], a vast body of research has formed around the goal of categorizing the many different types of neurons. Given the incredible range of neuronal morphologies, it is unsurprising that the different types of neurons occupy a wide variety of functional roles. In the retina alone, it is estimated that there are over 100 neuron types[73–75]. The first step towards understanding the relationship between morphology and functionality is to define the basic structural features of a neuron. These include the neuron's cell body (often referred to as the soma), dendrites, and axon. Figure 2-1 provides a diagram labelling each of these features. The collection of all of a neuron's dendrites can be referred to as its dendritic arbor. Similarly, if a neuron's axon bifurcates into multiple branches, this can be referred to as its axonal arbor. Also depicted in Fig. 2-1 are the myelin sheath (which insulates the neuron's axonal arbor and is provided by Schwann cells in the peripheral nervous system or oligodendrocytes in the central nervous system), nodes of Ranvier (which aid in the efficient propagation of action potentials), and synapses (which allow neurons to connect and transfer electrical or chemical signals to each other).

While Fig. 2-1 provides a useful model for understanding the basic structural and functional components of neurons, it doesn't capture the variety of ways in which different neuron types employ these components. Some neuron types feature dense dendritic arbors but sparse axonal arbors, while others don't have any dendrites at all and their primary function is to stimulate other neurons using their axonal arbor. Amazingly, it has been shown that individual neurons within the hippocampus contain up to 60000 synaptic connections[76]. The impressive diversity seen across different neuronal

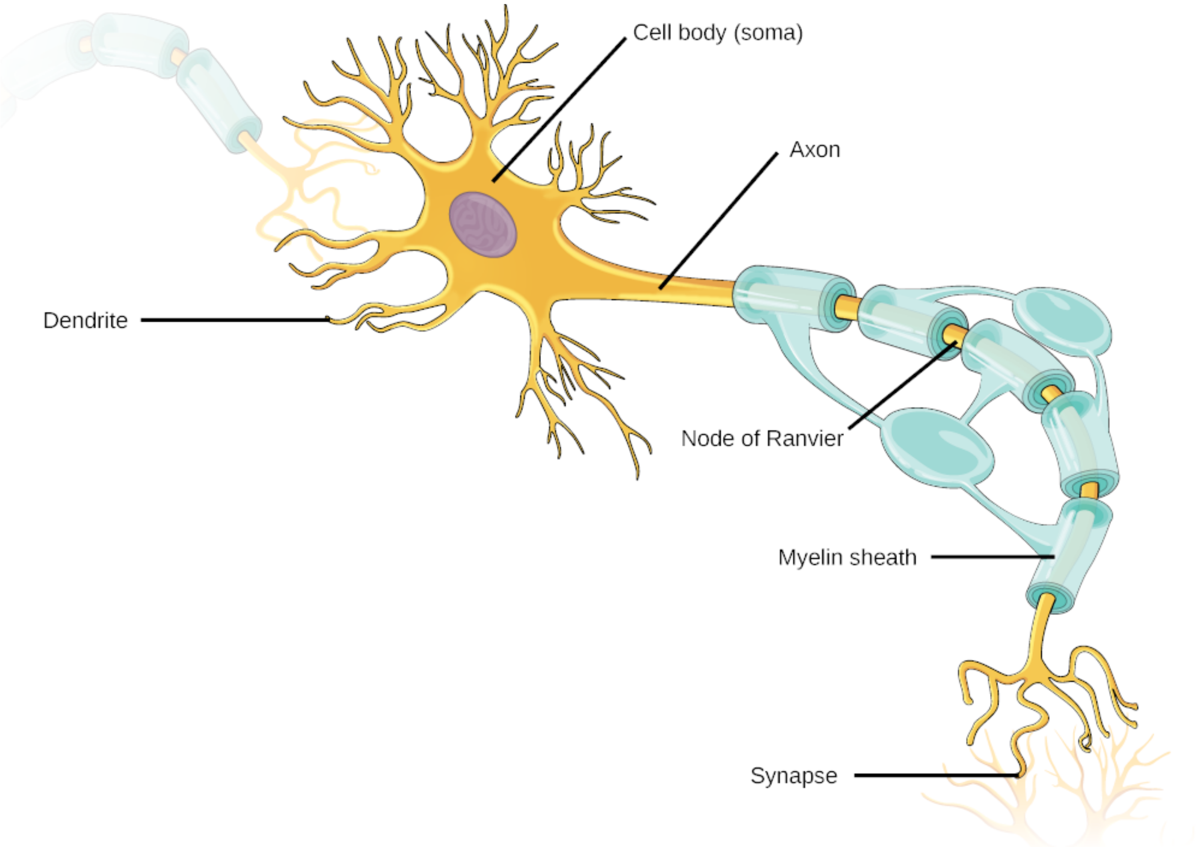

Figure 2-1. Diagram labelling the primary structural features of a neuron. (Adapted from *Biology* by Connie Rye *et al.*[77])

morphologies can instantly be appreciated from the illustrations created by Ramón y Cajal. Figure 2-2 shows one such illustration including several neuron types within the mammalian cerebellum. Given this diversity, it becomes apparent that categorizing different types of neurons must account for neuronal morphology.

While the detailed categorization of the many neuron types is undeniably an important field of research, another valuable approach is to examine universal behavior within and across different neuron types. Such studies provide us with a better understanding of the fundamental principles underlying neuron growth. Building on Ramón y Cajal's wiring economy principle, previous studies have demonstrated that the power-law scaling of various morphological metrics derived from a

Figure 2-2. Illustration of various neuron types within the mammalian cerebellum. (Adapted from *Texture of the Nervous System of Man and the Vertebrates* by Santiago Ramón y Cajal[72])

neuron's dendritic arbor as well as self-similarity within the arbor are tied to the neuron's ability to create optimally wired networks that minimize various costs, including metabolic expenditures[78,79], wire volume[80–82], and signal attenuation and delay[83–85]. However, these studies have relied on extracting power-law and self-similarity scaling exponents using large datasets of neurons. One consequence of this is that these studies do not address how variations in scaling properties across different neurons within a dataset might also be related to their functionality.

Fractal analysis provides a potential avenue for addressing this issue because it allows for a quantification of the self-similarity of an individual neuron's dendritic arbor. Although numerous previous studies have quantified the fractal scaling properties of dendritic arbors, this was typically done measure the complexity of the arbor or to test the effectiveness of fractal analysis at appropriately categorizing neuron types[17,21,86–100]. However, the propensity for neurons to display fractal scaling leads to an important question. Why does the body rely on fractal neurons rather than, for example, the Euclidean wires prevalent in everyday electronics? The research presented in chapter IV of this dissertation addresses this question by charting relationships between the fractal properties of neurons and their functional demands.

Fractal Analysis

The seeds of fractal analysis were sown well before Benoit Mandelbrot coined the term 'fractal'. Starting in the late 1800s to early 1900s, mathematicians like Georg Cantor, Helge von Koch, and Giuseppe Peano, with their analyses of the Cantor set, Koch curve, and Peano curve, challenged the effectiveness of Euclidean geometry to appropriately characterize structures displaying highly disjoint, irregular, or jagged features. Mandelbrot, recognizing that many natural systems display these features, developed fractal geometry to better understand them. Whereas the morphology of coastlines, trees, and clouds was often simply viewed as disordered and irregular, Mandelbrot had the insight to identify the structures' underlying order. Critically, Mandelbrot identified that many natural systems display statistical self-similarity that can be characterized by a fractal dimension, D, that exists in between the integer dimensions associated with Euclidean geometry. Whereas some mathematical fractals like the Peano curve (for which $D = 2$) are still described by integer dimensionality, this is typically not the case for natural systems.

The difference between the 'perfect' self-similarity of many mathematical fractals and the statistical self-similarity of many natural systems can be better understood by examining the behavior of fractal bifurcating trees. The leftmost tree in Fig. 2-3 is generated using a power-law distribution of branch lengths and a constant forking angle. The behavior of higher order branches within the tree are seen to be self-similar to the tree as a whole. The middle-left and middle-right trees in Fig. 2-3 are constructed in the same manner as the leftmost tree except that statistical variations have been inserted into the distribution of branch lengths (middle-left) and the forking angles (middle-right). The rightmost tree in Fig. 2-3 has had a statistically varying weave inserted into its branches but maintains the same branch length distribution and forking angle as the leftmost tree. By inserting these variations into the leftmost tree's branches, the tree deviates away from the self-similar condition and instead displays statistical self-similarity. This statistical self-similarity is further visualized in Fig. 2-4, which shows a tree with weaving branches and statistical variations in its branch lengths and forking angles. By clipping off and zooming in on higher order branches within the tree, the statistical self-similarity of the structure becomes apparent.

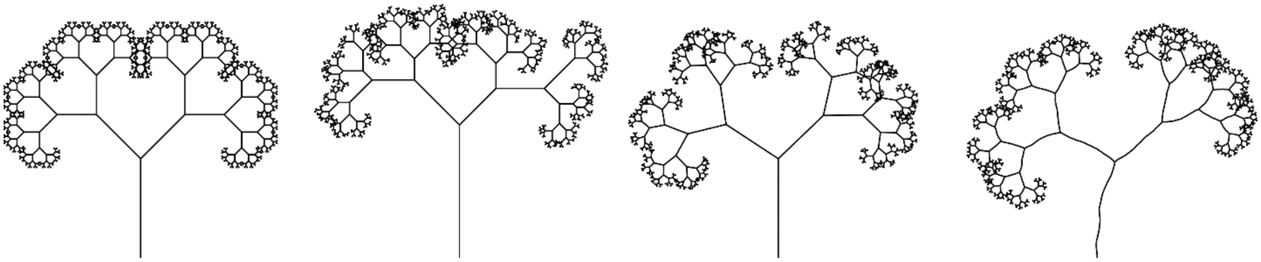

Figure 2-3. Statistical variations of a fractal bifurcating tree.

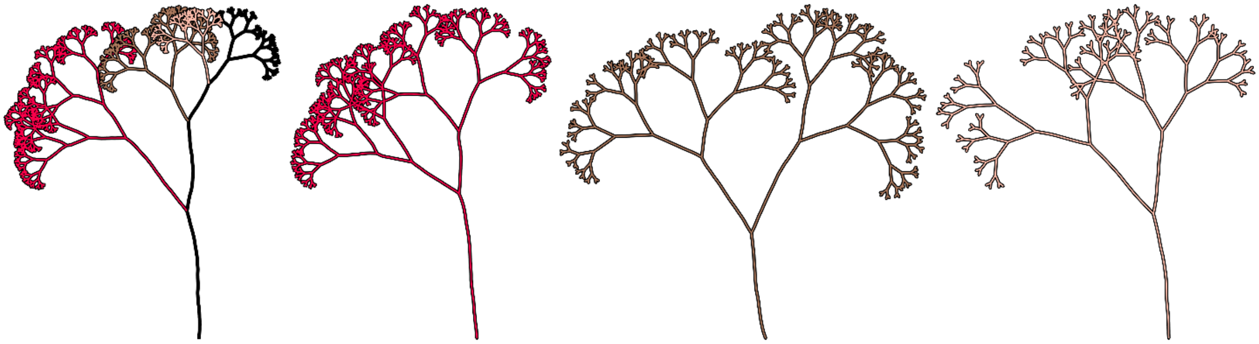

Figure 2-4. Visual demonstration of statistical self-similarity within a fractal bifurcating tree. The leftmost image shows the entire tree, while the three images from middle-left to right show zoom-ins of higher order branches within the tree. The color of each zoom in is shared with the leftmost image to indicate its placement within the tree.

For many natural systems, their statistical self-similarity is tied to their fractal properties and so it is valuable to measure their *D* value. To elucidate the measurement of a structure's *D* value, it is useful to start by examining a simple mathematical fractal. Consider the Koch curve, which is generated by iterative replacement of straight line segments with lines that have a kink in the middle. Figure 2-5A illustrates what the Koch curve looks like as the number of iterations increases. The kinked line that replaces the straight line segments is often referred to as the ‘generator’ of the Koch curve. Figure 2-5B shows what the Koch curve looks like as the sharpness of the generator’s kink is changed. As the kink increases in sharpness, the corresponding *D* value of the Koch curve also increases. These Koch curves provide a visual demonstration of the relationship between *D* and the space-filling properties of a fractal. As *D* increases, so too does the degree to which a fractal fills space.

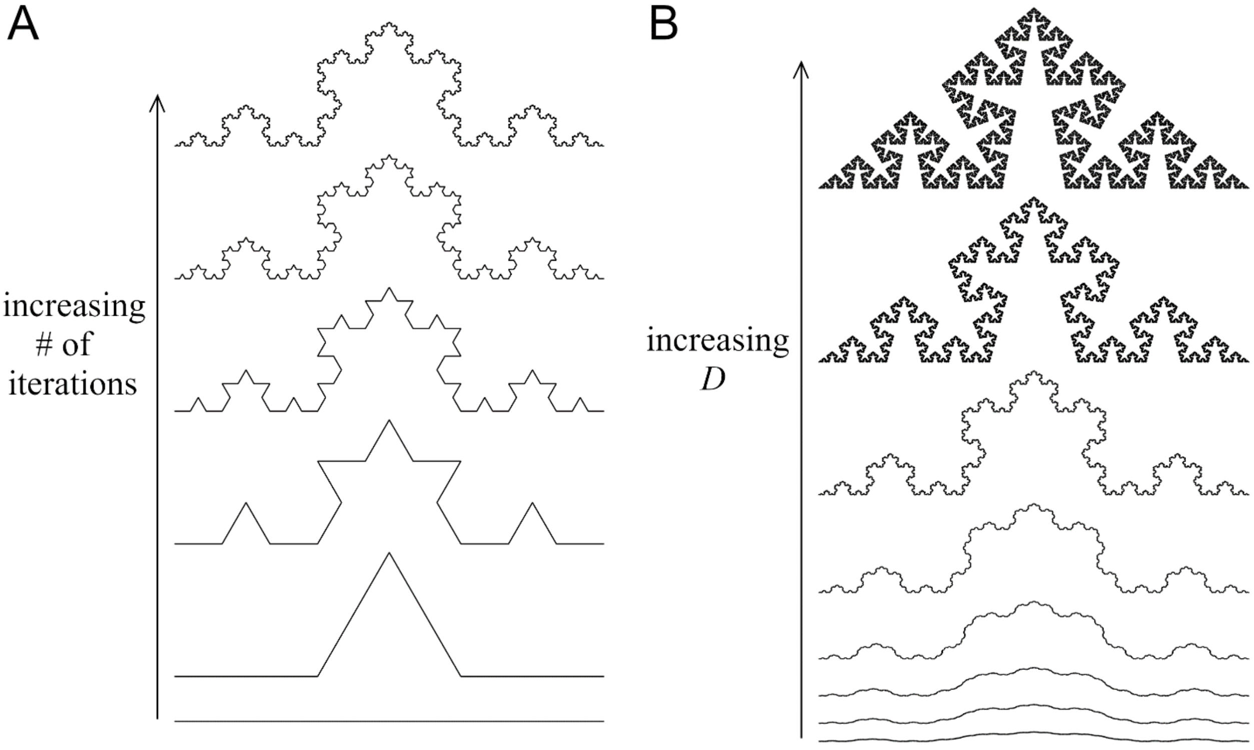

Figure 2-5. Constructing the Koch curve. (**A**) Diagram of a Koch curve as the number of iterations used to generate the curve increases. (**B**) Diagram of multiple Koch curves constructed using different generators. The *D* value of each curve depends on the shape of its generator.

The traditional Koch curve’s generator has a kink corresponding to a 60° angle. Assuming the traditional Koch curve is built starting with a straight line of unit length, the corresponding length of each of the 4 line segments comprising the generator is 1/3. Using the following equation, the theoretical fractal dimension, D_T, of the Koch curve can be calculated:

$$D_T = -\frac{log(N_\varepsilon)}{log(\varepsilon)} \qquad \text{(Eq. 2-1)}$$

Here, N_ε is the number of elements in the generator and ε is the scaling factor of those elements. For the traditional Koch curve, $N_\varepsilon = 4$ and $\varepsilon = 1/3$, which gives a D_T value of approximately 1.26. Though Eq. 2-1 is useful in its application to mathematical fractals displaying regular self-similar scaling in their structure, the question remains as to how D can be measured for physical fractals that instead display statistical self-similarity.

Addressing this question, Mandelbrot adopted a technique employed by Lewis Fry Richardson in his measurements of the scaling properties of coastlines. For structures that can be represented by a continuous curve, such as coastlines, the structure's D value can be measured by counting the number, N_R, of straight rulers of length L_R that are needed to trace it across a range of L_R values. If N_R follows a power-law relationship with L_R (as given by Eq. 2-2 below), then the D value of the curve can be measured over the range of L_R values for which the relationship holds.

$$N_R \propto {L_R}^{-D} \qquad \text{(Eq. 2-2)}$$

Another useful technique that has commonly been employed to measure the D value of a structure is the 'box-counting method'. An important advantage that this technique has over Richardson's 'coastline method' is that it doesn't require any continuity in a structure. The box-counting method simply relies on counting the number of boxes, N_B, occupied by a structure when it is placed in a grid of boxes of side length L_B. Similar to the coastline method, if a power-law relationship between N_B and L_B holds over a range in L_B, then the D value of the structure can be measured as follows:

$$N_B \propto {L_B}^{-D}. \qquad \text{(Eq. 2-2)}$$

Figure 2-6 shows example scaling plots for three different Koch curves as given by the coastline and box-counting methods with the D_T and D values of the corresponding curve indicated at the top of each plot.

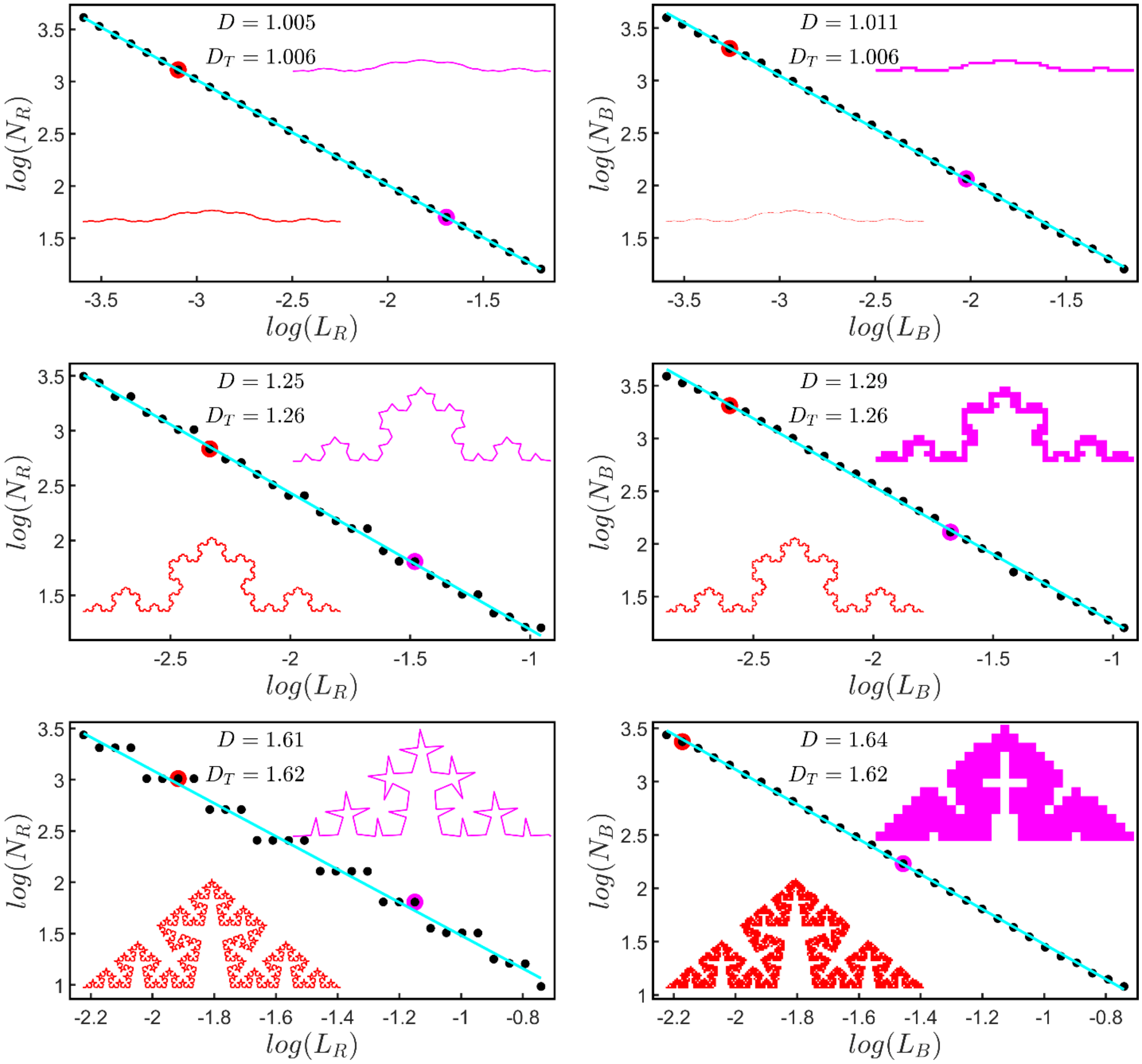

Figure 2-6. Coastline and box-counting fractal analyses applied to three different Koch curves. The left column shows the scaling plots resulting from application of the coastline method to Koch curves constructed from generators with kinks corresponding to 10°, 60°, and 80° angles (from top to bottom). The right column shows the scaling plots resulting from application of the box-counting method to the same three Koch curves. The measured D value is indicated at the top of each plot. Below this, the D_T value of the corresponding Koch curve is also indicated. The bottom-left (red) and top-right (magenta) insets of each plot show what the corresponding Koch curve looks like when represented at small and large size scales. The specific size scales are indicated by the highlighted data points in the scaling plot.

After Mandelbrot's demonstration of the effectiveness of fractal geometry at characterizing the behavior of many natural systems, it was quickly adopted by many researchers. However, as the body of research applying fractal analysis to natural systems grew, an important question became the focus of debate - when is it appropriate to label behavior as fractal? In his seminal work[15,16], Mandelbrot introduced fractality as an umbrella terminology to unite studies of scale invariant behavior in physical and mathematical systems. Importantly, he didn't introduce precise scaling ranges into the definition of fractality. While this was in part because of the clear contrast between the infinite pattern repetition of mathematical fractals and the limited pattern repetition of physical fractals, it crucially was also because the scaling range necessary for fractality to impact functionality varies considerably between physical objects. Addressing this debate, a survey was conducted that revealed published experimental studies of fractality in physical systems typically displayed scale invariance over only 1.3 orders of magnitude[101,102]. Guidelines from the survey authors for whether scaling plots with limited range are useful included: 1) "[it] condenses the description of a complex geometry", 2) "It allows one to correlate in a simple way properties and performances of a system to its structure." As will be demonstrated in chapter IV of this dissertation, investigating the morphology and functionality of neurons using fractal analysis meets these guidelines.

Carbon Nanotubes as an Implant Electrode Material

Carbon nanotubes (CNTs) are a patternable electrode material that simultaneously meet the multiple demands of medical implants that interface with neural tissue. In particular, the material must be biocompatible and follow a stringent set of electrical, chemical, and mechanical properties. Electrically, the electrode must inject sufficiently large currents into the neural tissue, ideally through a purely capacitive means[103]. Chemically, electrode materials must resist degradation in the physiological environment of neural tissue and should support surface functionalization to increase their hydrophilicity, thereby preventing neuronal cell death and stimulating neurite outgrowth[104], and also reduce the voltage threshold needed for neuronal stimulation[105]. Mechanically, they need to be strong and yet flexible to reduce inflammation and glial scarring in the surrounding tissue[106–108]. Furthermore, soft materials (i.e., mechanically compliant)[109,110] and materials with rough, textured surfaces[111,112] can enhance neurite outgrowth, elongation rate, and branching.

CNTs are electrically conductive and have a double-layer capacitance that compares favorably to most other materials[113]. They are mechanically flexible[114–116] yet incredibly strong[117], and their molecular-scale diameter promotes strong adhesion and electrical coupling with neurons[118,119]. Vertically aligned carbon nanotubes (VACNTs) can be patterned and synthesized using chemical vapor deposition (CVD) to form high-aspect-ratio structures with heights exceeding 500 µm[120], and because neurons adhere strongly to CNTs, patterned CNTs can be used as scaffolds to guide neurite growth[121]. Importantly, while the biocompatibility of CNTs depends on the kind of tissue the CNTs interact with as well as the method of CNT synthesis, several types of neural tissue, including hippocampal and cortical neurons, glial cells, and retinal precursor cells[120–124], have been shown *in vitro* to be biocompatible with CNTs. Additionally, CNTs can be chemically functionalized to further improve their biocompatibility. Neurons cultured on functionalized CNTs have been shown to display improved neurite outgrowth and branching[125,126]. Furthermore, previous studies have highlighted CNTs ability to decrease glial scar tissue formation[127] and have demonstrated their capacity to stimulate neurons effectively[105,118,128] and boost signal transmission[129–132]. Due to this combination of useful properties, CNTs have been employed in multi-electrode arrays (MEAs) for epiretinal implants[133,134] and *in vitro* MEA studies where CNTs improved the signal-to-noise ratio, lowered the stimulation threshold, and minimized glial scarring[135].

Throughout chapter III of this dissertation, VACNTs are employed as an electrode material to examine how various electrode geometries impact the morphological properties of *in vitro* cultures of retinal neurons and glia. The specific VACNT preparation that is used was motivated by the beneficial properties associated with CNTs described above and by a previous study (on which I am a co-author) that tested the impact of various VACNT preparations on the growth of retinal neurons[136]. The results of that study indicated that unfunctionalized VACNTs grown via CVD on an aluminum/iron catalyst layer (labelled as Al/Fe) had significantly more neurite growth than similarly grown VACNTs functionalized with oxygen plasma (labelled as Al/Fe+Pl). They also performed better than both functionalized and unfunctionalized VACNTs grown on an iron catalyst layer (labelled as Fe+Pl and Fe, respectively). A qualitative representation of this result is shown in Fig. 2-7.

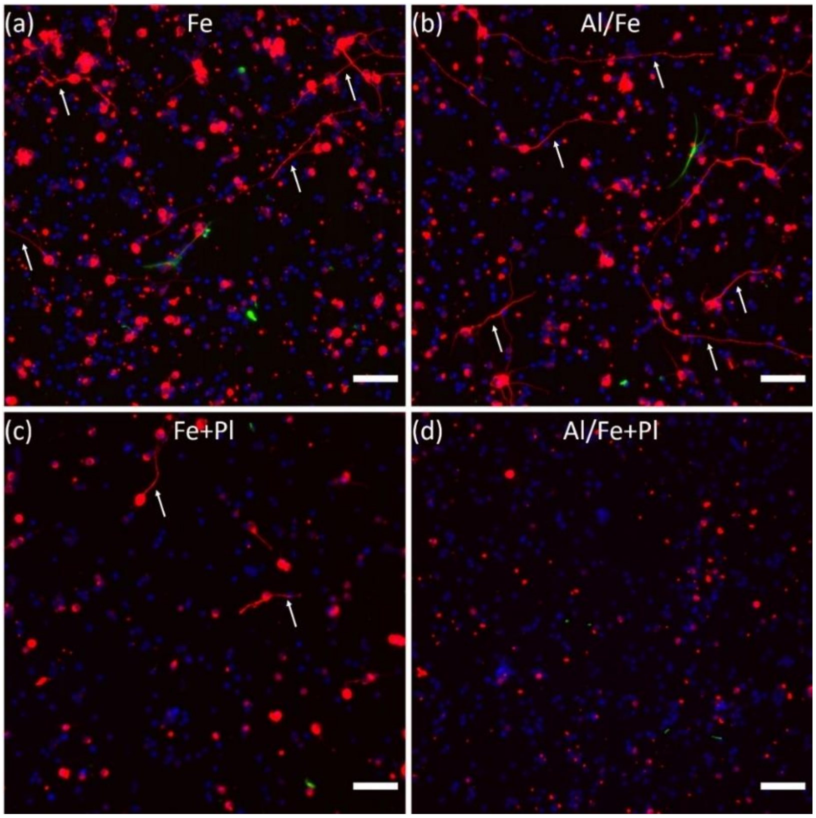

Figure 2-7. Impact of VACNT preparation on neurite growth. Fluorescence images of β-tubulin III labelled neurons (red), GFAP labeled glia (green), and cell nuclei (blue) on multiple VACNT preparations. (**a**) Fe, (**b**) Al/Fe, (**c**) Fe+Pl, and (**d**) Al/Fe+Pl preparations showing the occurrence of neurite-bearing cells and the extent of neurite outgrowth in the different preparations. The arrows in each image indicate examples of neurite growth. The scale bars all correspond to 50 µm. (Figure adapted from *The Roles of an Aluminum Underlayer in the Biocompatibility and Mechanical Integrity of Vertically Aligned Carbon Nanotubes for Interfacing with Retinal Neurons* by Saba Moslehi *et al.*[136])

Surface Patterning as a Mechanism for Controlling Neuronal and Glial Behavior

A diverse range of previous studies have investigated the impact that a surface's various physical properties have on the behavior of neurons and glia. For example, materials with nano-rough surface features as well as those that have been patterned at the micro-scale using lithography have been used to control cell attachment and guidance[66,67,137–141] and test their ability to reduce gliotic responses[142,143]. Neurite growth has been shown to be enhanced by soft, textured surfaces[138,144–146] through their close resemblance to the structure of the extracellular matrix (ECM)[120,147]. In contrast, glial coverage achieved by cell growth and division was seen to be dampened on textured as well as softer substrates as a result of weakened surface interactions[143,148–153]. Consistent with these results, an experiment employing a co-culture of neurons and glia demonstrated that neurons accumulate on rows of nanowires while glia accumulate in the flat regions between them[142]. Despite all these efforts, the mechanisms controlling the interactions of different cell types with various surfaces are yet to be fully understood.

The research presented in chapter III of this dissertation focuses on the importance of the combination of electrode geometry and material properties for controlling neuronal and glial behavior. Whereas fractal surface texturing has been shown to enhance capacitance[103,154] and cell growth[155–158], surfaces employing fractal branch patterns to selectively direct cell growth have not been considered. Most previous studies of directed cell growth have all focused on single-scale (Euclidean) geometries. A critical aim of the research presented in chapter III is to display the capability of patterned VACNT electrodes to 'herd' neurons and glia, where herding implies that neurons preferentially adhere to and form dense networks on the textured, fractal branches of the electrode and glial cells primarily cover the smooth SiO_2 surface of the gaps between the electrode branches.

CHAPTER III

RETINAL CELL ASSEMBLY AT THE LARGE SCALE

The work presented within this chapter has been adapted from previously published co-authored work by S. Moslehi, C. Rowland, J. H. Smith, W. J. Watterson, D. Miller, C. M. Niell, B. J. Alemán, M.-T. Perez, and R. P. Taylor in *Controlled assembly of retinal cells on fractal and Euclidean electrodes*, PLOS ONE **17**, e0265685 (2022) and by S. Moslehi, C. Rowland, J. H. Smith, W. Griffiths, W. J. Watterson, C. M. Niell, B. J. Alemán, M.-T. Perez, and R. P. Taylor in *Comparison of fractal and grid electrodes for studying the effects of spatial confinement on dissociated retinal neuronal and glial behavior*, Scientific Reports **12**, 17513 (2022).

This chapter begins by providing an overview of the experimental methods used to investigate the impact of large-scale lateral patterning of vertically aligned carbon nanotube (VACNT) electrodes on the assembly of retinal neuronal and glial cells *in vitro*. The results of the experiment are then presented qualitatively and quantitatively. Patterns featuring several different Euclidean and fractal geometries are examined. The Euclidean patterns include rows of VACNTs of varying width separated by rows of bare silicon dioxide (SiO_2) of varying width, while the fractal patterns include H-Tree fractals of varying fractal dimension and number of repeating levels. The behavior of the network of neurons that forms on the patterned VACNTs is investigated by measuring the degree of process growth on the VACNT surfaces as well as the surrounding SiO_2 surfaces. In a similar fashion, the behavior of the glial cells is investigated by measuring the degree to which they cover the VACNT and SiO_2 surfaces. A model is presented that details the impact that electrode geometry has on the behavior of the neurons and glia. The implications of the model are then tested by comparing two different pattern geometries, specifically a Euclidean grid and an H-Tree fractal. In general, it is found that the VACNT-SiO_2 material system performs well at supporting neuron growth on the VACNTs while also guiding glial growth onto the surrounding SiO_2 and that electrode geometries which strike a balance between providing a large VACNT surface while also allowing the surrounding SiO_2 surface to interpenetrate the VACNT surface in a manner that maintains the connectedness of the SiO_2 surface are likely to perform the best at supporting healthy networks of neurons and glia over the long term.

Electrode Patterning

In total, 13 unique geometries were used to pattern the VACNT electrodes. Each of these 13 geometries were partitioned into three primary groups. The first group was patterned into Euclidean rows of electrode width, W_{CNT}, and separation, W_{Si}. The second group was patterned into H-Tree geometries of fractal dimension, D, and repeating level, m. Here, repeating level refers to how many different size scales the 'H' pattern are present in the design (i.e. 4 repeating levels means H's at 4 different size scales are used to construct the fractal). The third group was patterned into a Euclidean grid with square chambers of constant width, W_{Si}. For each of these groups, the overall width of the electrode, W, the area covered by the electrode, A_{CNT}, the bounding area of the electrode, $A_{bounding}$, and the area of the SiO_2 surface contained within the bounding area of the electrode, A_{Si}, are all affected by the specific choice of geometric parameters used in the electrodes patterning. Table 3-1 gives a summary of each of these geometric measurements for all of the electrode groups. The naming convention for the subgroups within the Euclidean Rows group (given as S[W_{Si}]C[W_{CNT}]) indicates the W_{Si} and W_{CNT} values corresponding to that subgroup. The naming convention for the subgroups within the Fractal group (given as D-m) indicates the fractal dimension and repeating level corresponding to that subgroup. Figure 3-1 indicates how W_{CNT}, W_{Si}, and W are measured for each of the electrode groups.

Table 3-1. Geometric measurements for each of the patterned electrode groups.

Subgroup	W_{CNT} (μm)	W_{Si} (μm)	W (μm)	A_{CNT} (μm^2)	A_{Si} (μm^2)	$A_{bounding}$ (μm^2)
Euclidean Rows						
S100C100	100	100	6.0×10^3	1.8×10^7	1.7×10^7	3.5×10^7
S75C100	100	75	6.0×10^3	2.0×10^7	1.5×10^7	3.5×10^7
S50C100	100	50	6.0×10^3	2.4×10^7	1.2×10^7	3.6×10^7
S25C100	100	25	6.0×10^3	2.9×10^7	7.0×10^6	3.6×10^7
S75C75	75	75	6.0×10^3	1.8×10^7	1.8×10^7	3.6×10^7
S50C50	50	50	6.0×10^3	1.8×10^7	1.8×10^7	3.6×10^7
S25C25	25	25	6.0×10^3	1.8×10^7	1.8×10^7	3.6×10^7
Fractal						
1.1-4	20	X	6.0×10^3	8.0×10^5	1.8×10^7	1.9×10^7
1.5-4	20	X	6.0×10^3	1.5×10^6	2.1×10^7	2.3×10^7
2-4	20	X	6.1×10^3	2.3×10^6	2.4×10^7	2.7×10^7
2-5	20	X	6.3×10^3	4.6×10^6	2.3×10^7	2.8×10^7
2-6	20	X	6.3×10^3	8.8×10^6	1.8×10^7	2.8×10^7
Grid						
X	20	61	3.5×10^3	5.4×10^6	6.9×10^6	1.2×10^7

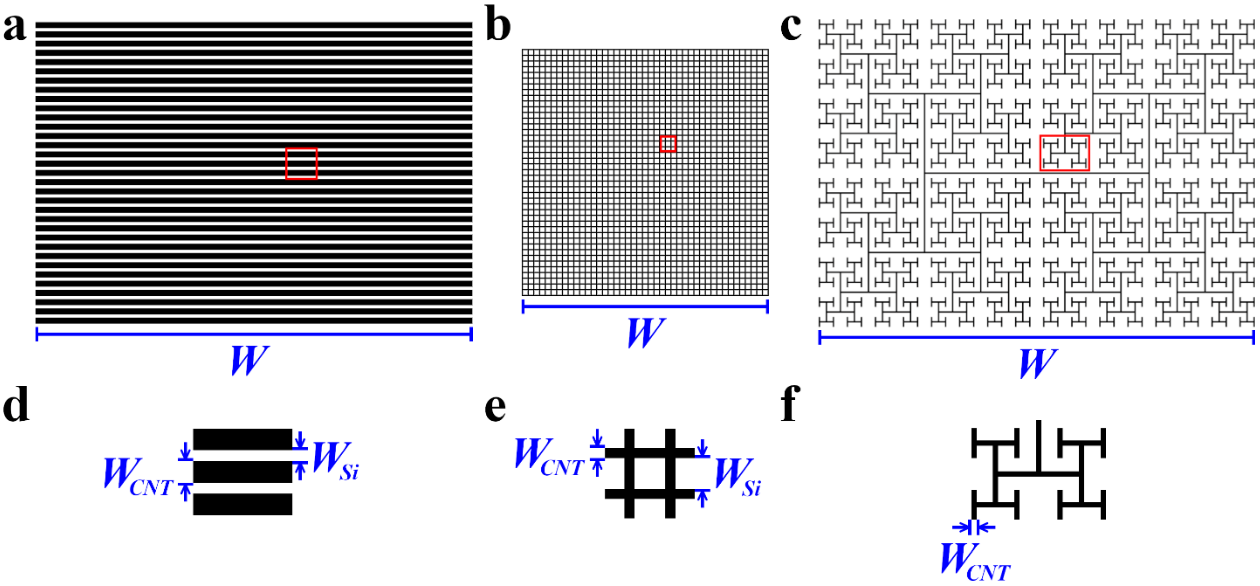

Figure 3-1. Example measurements of various geometric widths on each patterned electrode group. CNT width, W_{CNT}, SiO$_2$ width, W_{Si}, and overall electrode width, W, are indicated on schematics of example patterns from the (**a**) Euclidean Rows, (**b**) Fractal, and (**c**) Grid groups. Panels (**d**), (**e**), and (**f**) show zoom-ins on the regions within the red squares in (**a**), (**b**), and (**c**), respectively.

VACNT Synthesis and Characterization

Microfabrication and lithography techniques were used to synthesize the VACNT electrodes following procedures that have been described in detail elsewhere[136]. Briefly, 2-inch silicon wafers with a 300 nm thermal oxide (SiO_2) top layer were cleaned and patterned using photolithography techniques. After photoresist development, a 2-5 nm aluminum (Al) adhesive layer was deposited thermally followed by an electron-beam deposition of a 3-5 nm iron (Fe) catalyst layer. After 30 seconds of acetone soaking accompanied by sonication to lift off the photoresist layer, the wafer was then cut into individual samples with each sample featuring one electrode. Not all of the fabricated samples were used in the dissociated cell culture experiments. Some samples were eliminated due to visible defects or were saved for further SEM characterization. Chemical vapor deposition (CVD) techniques were used to synthesize VACNTs on the catalyst patterns in a 2-inch quartz tube. A 2:1 mixture of ethylene (C_2H_4):hydrogen (H_2) (200 and 100 SCCM, respectively) accompanied by a 600 SCCM flow of Argon (Ar) was maintained during the 3-minute growth time at 650°C. This technique resulted in patterned electrodes consisting of entangled ‘forests’ of VACNTs (Fig. 3-2 and Fig. 3-3) with heights in the range of 20-45 µm. The electrodes were then stored in integrated circuit trays in a desiccator cabinet. The top surface and sidewalls of the VACNTs, their heights and general conditions were inspected using a ZEISS-Ultra-55 scanning electron microscope. No visual differences were observed between samples from the various electrode designs and fabrication runs. During culture, the samples were placed in 4-well culture plates (Sarstedt, Newton, NC) with one sample per well.

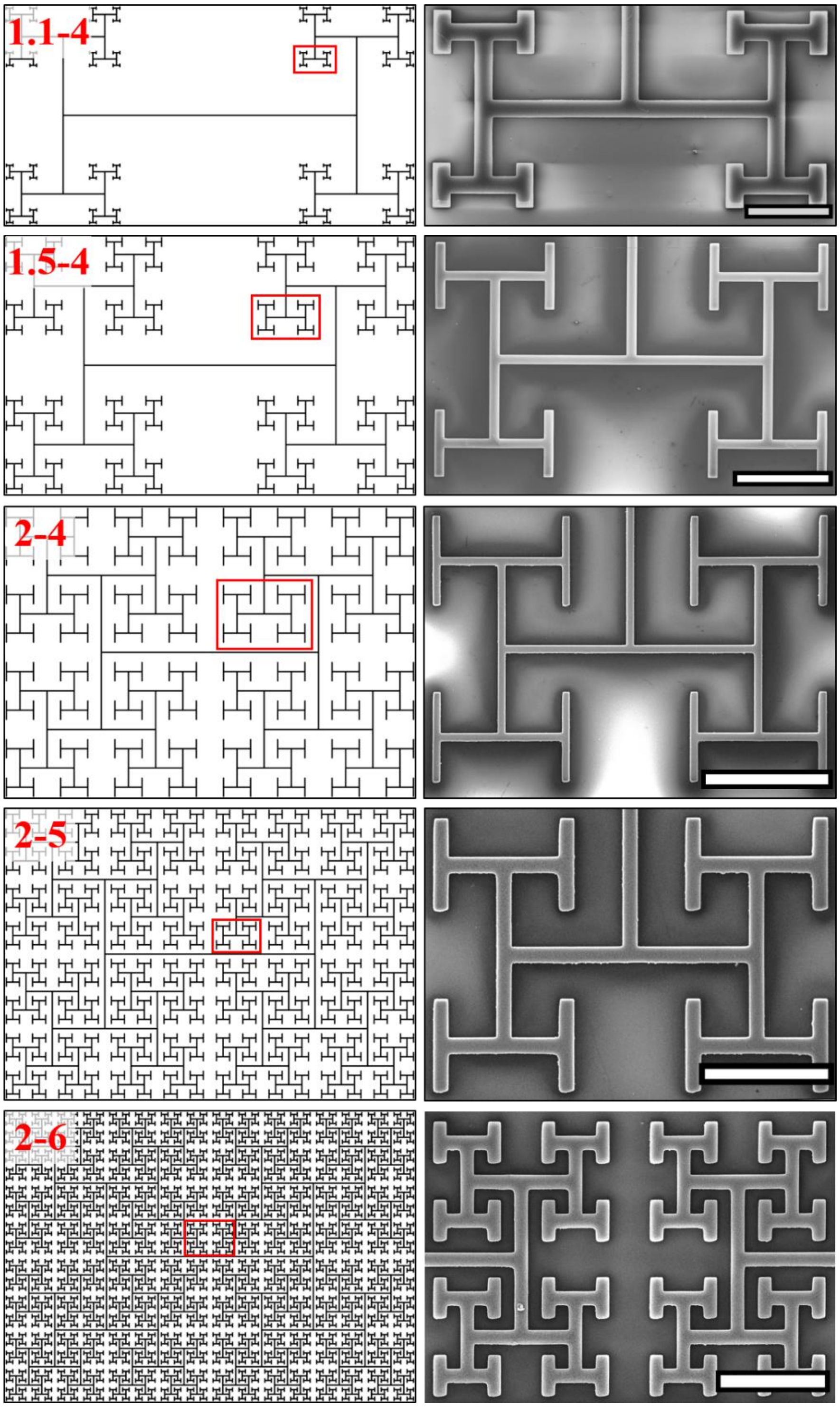

Figure 3-2. Schematic and scanning electron microscopy (SEM) images of electrodes from the Fractal group with different fractal dimensions and repeating levels. Left column from top to bottom: (*D* = 1.1 and *m* = 4, labelled as 1.1-4), (*D* = 1.5 and *m* = 4, labelled as 1.5-4), (*D* = 2 and *m* = 4, labelled as 2-4), (*D* = 2 and *m* = 5, labelled as 2-5), (*D* = 2 and *m* = 6, labelled as 2-6). Right column: equivalent SEM image of the area marked by the red square in each electrode on the left column. The scale bars are 100, 200, 400, 200 and 200 µm from top to bottom.

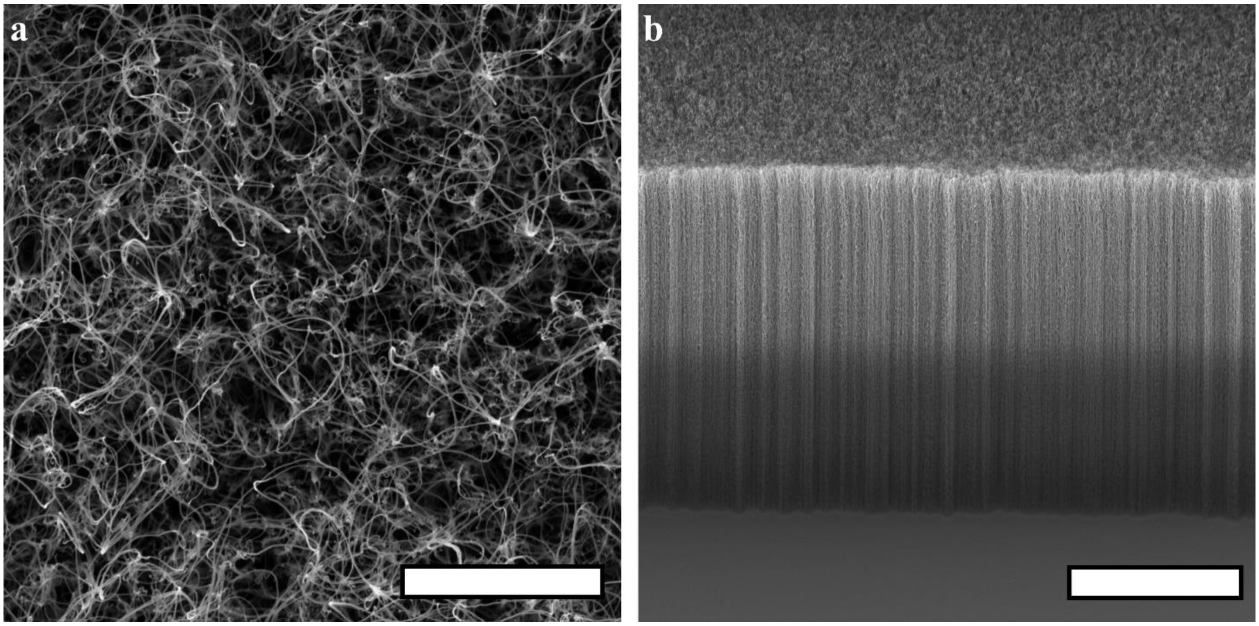

Figure 3-3. SEM images of patterned VACNT forests taken before the culturing experiments. (**a**) Top-down view of entangled VACNTs on the forest's top surface, (**b**) View of the sidewall of a VACNT row taken at a 40° angle. Scale bars are 2 and 10 µm, respectively.

Dissociated Retinal Cell Cultures

Wildtype C57BL/6J mice were kept at animal welfare services at University of Oregon (UO) with full time access to fresh water and food supplies. Handling and culture procedures involving the mice were performed according to protocols approved by the UO's Institutional Animal Care and Use Committee (IACUC) under protocol 16-04, in compliance with the ARRIVE and National Institutes of Health guidelines for the care and use of experimental animals. Dissociated retinal cell cultures were employed using protocols described elsewhere[69,136,159]. Briefly, postnatal day 4 (PN4) mice were euthanized by decapitation and their retinas quickly dissected and kept in Dulbecco's Modified Eagle Medium (DMEM – ThermoFisher Scientific, Waltham, MA) containing high-glucose, sodium pyruvate, L-glutamine, and phenol red. For each culture experiment, four retinas were transferred into an enzyme solution containing DMEM, papain (Worthington Biochemical Corporation, Lakewood, NJ) and L-cysteine (Sigma-Aldrich, St Louis, MO). The digested retinas were carefully rinsed with DMEM and transferred to new DMEM containing B27 (Sigma-Aldrich, St Louis, MO) and L-glutamine-penicillin-streptomycin (Sigma-Aldrich, St Louis, MO). The dissociated retina solution was then centrifuged, and the resulting cell pellet was re-suspended in the DMEM/B27/antibiotic solution. The cell suspension (500 μL) was subsequently seeded onto each well containing an electrode. The cells were cultured for 17 DIV at 37°C and 5% CO_2. The culture medium was first changed at 3 DIV and then every other day until the end of the culture time. No protocols such as precoating the surfaces with poly-D-lysine (PDL) or poly-L-lysine (PLL) were used to increase the neuronal and glial adhesion to the different surface types. The live cell density as measured by a hemocytometer was $(3.7 \pm 0.4) \times 10^6$ cells/mL.

Immunocytochemistry

The immunocytochemistry protocol is described in detail elsewhere[69,136,159]. Briefly, the cells were fixed with 4% paraformaldehyde (PFA), rinsed with a phosphate buffered solution (PBS) and pre-incubated in PBS-complete, containing PBS, Triton-X (Sigma-Aldrich, St Louis, MO), bovine serum albumin (BSA) (Sigma-Aldrich, St Louis, MO), goat normal serum and donkey normal serum (Jackson ImmunoResearch, West Grove, PA). The cells were subsequently incubated with PBS-complete containing the primary antibodies, mouse anti-β-tubulin III (neuronal marker for several neuron types in the mouse retina[160,161] – Sigma-Aldrich, St Louis, MO) and rabbit anti-glial fibrillary acidic protein (GFAP; glia marker – Agilent, Santa Clara, CA) over night at 4°C. The cells were then rinsed and incubated with PBS-complete containing the secondary antibodies Cy3 goat anti-mouse IgG and AlexaFluor 488 donkey anti-rabbit IgG (Jackson ImmunoResearch, West Grove, PA). The secondary antibody solution was then removed and the cells rinsed with PBS. The samples were transferred to microscope slides and mounted with Vectashield containing DAPI (fluorescent cell nuclear marker that binds to DNA – Vector Laboratories, Burlingame, CA).

Fluorescence Microscopy

A Leica DMi8 inverted fluorescence microscope was used to take 20× images in the Cy3 (excited at 550 nm, emission peak at 570 nm), AlexaFluor 488 (excited at 493 nm, emission peak at 519 nm) and DAPI (excited at 358 nm, emission peak at 461 nm) channels for all electrodes. The top VACNT and bottom SiO_2 surfaces were imaged separately with the focus being adjusted to these surfaces. The 2048 × 2048 $pixel^2$ (662.65 × 662.65 μm^2) field of views (FOVs) in each channel were then stitched together using an automated stitching algorithm with 10% overlap at the edges of neighboring FOVs to create full electrode images.

Post-culture SEM imaging

For post-culture SEM imaging, cells were fixed in 1.25% and 2.5% glutaraldehyde solutions in deionized (DI) water for 10 and 20 minutes, respectively. After rinsing 3 times in PBS for 10 minutes each, the wafers were submerged in increasing concentrations of ethanol (50%-100%) for 15 minutes each for dehydration. They were then submerged in a 2:1 solution of ethanol:HMDS for 20 minutes followed by a 20-minute rinse in 1:2 ethanol:HMDS and finally a 20-minute rinse in 99.9% HMDS. The cells were left in fresh 99.9% HMDS overnight to let it evaporate. The electrodes were then coated with a 20 nm thick layer of gold before SEM imaging.

Quantitative Measurement of the Neuron Process Length and Glial Coverage

Neuron process growth was chosen as the morphological phenotype measurement of neuronal cell health and function[162,163]. This was in part based on the long-term goal of employing electrodes for neuron stimulation and the high density of stimulation sites on the processes. The quantitative analysis involved a calculation of the density of processes (i.e. total length of the neurons' dendrites and axons within a given surface area). Based on their role of promoting neuron homeostasis and survival, the glial analysis focused on quantifying the surface area expressing the cytoskeletal marker GFAP[143]. This analysis involved a calculation of their surface coverage density (referred to hereafter as 'coverage', i.e. the surface area covered by glia normalized to the total surface area available).

To perform this quantitative analysis, binary masks were created for each electrode geometry and applied to all acceptable FOVs for each electrode so that the SiO_2 and VACNT surfaces could be analyzed separately. Unacceptable FOVs (e.g. those with any abnormalities such as VACNT deformations) were rare: typically 2 out of 50 FOVs. An automated image analysis algorithm (based on one previously reported by Wu *et al.*[164]) was integrated with the binary masks to detect and measure the process length per FOV on the SiO_2 and VACNT surfaces separately. In cases when processes physically overlapped (for example, when they 'bundled' together and followed a common route on the surface or when multiple processes followed the same electrode edge), the algorithm detected these as one process. This resulted in an undercount of processes, especially on the VACNT surface, but did not affect the general results of the experiments. For each electrode, the normalized process length on the SiO_2 (N_{Si}) and the VACNT (N_{CNT}) surfaces was then defined as the total process length on each surface across all FOVs (N_{LSi} or N_{LCNT}) divided by the total area of that surface in the electrode (A_{Si} or A_{CNT}):

$$N_{Si} = \frac{N_{LSi}}{A_{Si}} \qquad \text{(Eq. 3-1)}$$

$$N_{CNT} = \frac{N_{LCNT}}{A_{CNT}} \qquad \text{(Eq. 3-2)}$$

Adopting the above definitions for N_{Si} and N_{CNT}, these parameters have units of μm^{-1}.

For the glia, a semi-automated thresholding algorithm was integrated with the binary masks to detect and measure the glial area per FOV on the SiO_2 and VACNT surfaces separately. For each electrode, the normalized glial area on the SiO_2 and the VACNT surfaces were then defined as the total glial area on each surface across all FOVs (G_{ASi} or G_{ACNT}) divided by the total area of that surface:

$$G_{Si} = \frac{G_{ASi}}{A_{Si}} \quad \text{(Eq. 3-3)}$$

$$G_{CNT} = \frac{G_{ACNT}}{A_{CNT}} \quad \text{(Eq. 3-4)}$$

Adopting the above definitions for G_{Si} and G_{CNT}, these parameters are unitless. To minimize the error in detecting neuron process length and glial area around the edges of the electrodes on both surfaces, FOVs were inspected, and mask measurements were adjusted manually if necessary to allow for the correct detection of in-focus features. Figure 3-4 illustrates an application of the glial coverage and neuron process detection algorithms to the VACNT surface of a fractal electrode.

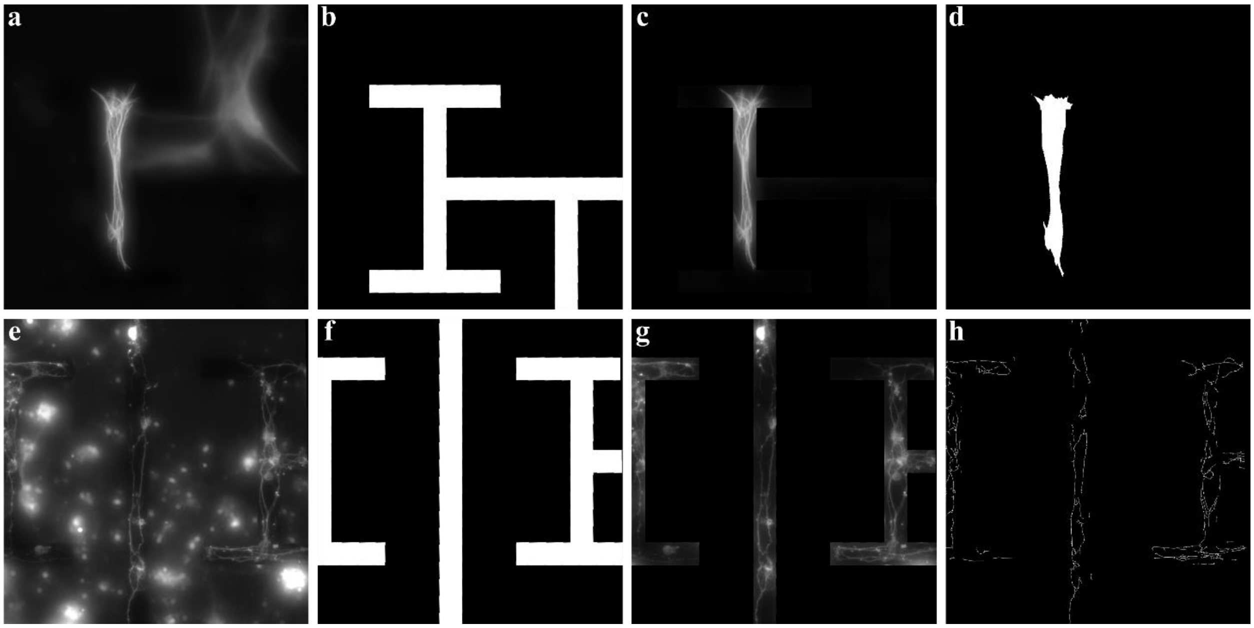

Figure 3-4. Representative images of the algorithm's process for detecting glial coverage and neuron processes. Fluorescence images of (**a**) glia and (**e**) neurons on the VACNT and SiO_2 surfaces of a fractal electrode where the focus is set on the VACNT surface. (**b**, **f**) The binary masks associated with the FOVs shown in (**a**) and (**e**) respectively. (**c**, **g**) Combination of the FOVs in (**a**, **b**) and (**e**, **f**) respectively for isolating the glia and neurons on the VACNT surface. (**d**, **h**) Applying the glia thresholding and neuron process detection algorithms to the FOVs shown in (**c**) and (**g**).

In order to quantitatively compare the total neuron process length and total glial coverage area of the VACNT and SiO_2 surfaces, three 'herding' parameters were introduced. Neuron herding, *N*, glia herding, *G*, and combined herding, *GN*, were defined as follows:

$$N = \frac{N_{CNT}}{N_{Si} + N_{CNT}} \quad \text{(Eq. 3-5)}$$

$$G = \frac{G_{Si}}{G_{Si} + G_{CNT}} \quad \text{(Eq. 3-6)}$$

$$GN = G \times N \quad \text{(Eq. 3-7)}$$

N and G values greater than 0.5 indicate successful guiding of neuron processes and glial cells to the desired VACNT or SiO_2 surface, respectively. Specifically, the $N > 0.5$ condition corresponds to more neuron processes existing on the VACNT surface than the SiO_2 surface. The $G > 0.5$ condition corresponds to more glial coverage on the SiO_2 surface than the VACNTs surface. GN was calculated to compare combined herding powers between various electrode groups.

Statistical Analysis

All statistical analyses presented within this chapter were done using functions available in MATLAB's Statistics Toolbox. The Shapiro-Wilk test was performed to determine the normality of the various neuronal and glial parameters. Because some of the distributions failed the normality criteria, the nonparametric Kruskal-Wallis test for significance (with a significance level of 0.05) was used to compare the medians of neuronal and glial parameters against various null hypotheses (for example G_{Si} and G_{CNT} were tested against the null hypothesis that surface material would not impact glial behavior). When multiple groups were being compared and significance was found using the Kruskal-Wallis test, the nonparametric post-hoc Dunn's test (with a significance level of 0.05) was used to determine which group pairings had a significant difference. Table 3-2 provides a summary of how many electrodes and how many independent cultures were used in these experiments for each electrode group. Some samples were excluded due to complications in fabrication or culturing procedures. Each independent culture included electrodes from multiple groups.

Table 3-2. Total number of each electrode geometry used as well as the number of independent cultures for each electrode design.

Culture Duration	**3 DIV**		**7 DIV**		**17 DIV**	
Subgroup	**Number of electrodes**	**Number of independent cultures**	**Number of electrodes**	**Number of independent cultures**	**Number of electrodes**	**Number of independent cultures**
Euclidean Rows						
S100C100	6	3	11	7	8	6
S75C100	3	2	4	4	6	4
S50C100	3	1	5	4	6	4
S25C100	3	1	5	4	4	2
S75C75	3	1	6	3	4	3
S50C50	3	1	6	3	5	3
S25C25	2	1	6	3	5	2
Fractal						
1.1-4	X	X	X	X	7	2
1.5-4	X	X	X	X	7	5
2-4	X	X	X	X	9	4
2-5	X	X	X	X	11	5
2-6	X	X	X	X	10	4
Grid						
X	X	X	X	X	7	3

Qualitative Observations of Herding in the Euclidean Rows and Fractal Groups

To begin, qualitative observations were made for the Euclidean Rows group using fluorescence and electron microscopy at 17 DIV to establish the basic herding properties of the retinal cells. Large numbers of glial cells were observed in the SiO_2 gaps, but they were confined by the electrodes and never traversed them. Individual glia rarely attached to the electrodes (Fig. 3-5b and f) and when doing so typically exhibited a more branched morphology (Fig. 3-5e). In contrast, neuron processes grew on both the gap and electrode surfaces, although they were considerably longer and formed more complex networks on the electrodes. For both the gaps and electrodes, neuron somas were seen to cluster together and the relatively simple networks in the gaps featured fewer but larger clusters (Fig. 3-5c and g). The neuron processes followed the top and the bottom edges of the electrodes upon reaching them and were able to climb up or down the sidewalls to connect cell clusters that existed on both surfaces (Fig. 3-5c, g, and h). The peak glia and neuron process locations along the direction perpendicular to the electrode rows (i.e. in the Y direction) were identified using the neuron process length and the glial coverage area algorithms by summing the neuron process length and the glial coverage area along the rows (i.e. in the X direction). The result demonstrates that glial coverage area peaked within the gaps and neuron process length was largest on the electrodes and peaked at their edges (Fig. 3-5a and d).

Figure 3-6 summarizes the retinal cell responses to electrodes from the Fractal group imaged at 17 DIV. One notable characteristic of their multi-scaled geometry is the frequent change in branch direction. Although glia rarely adhered to the electrodes, they elongated themselves along the branches and were not restricted by their 90° turns (Fig. 3-6a). Glial cells were observed in the gaps of all Fractal subgroups by 17 DIV, even for the most restricted gap connections (see the 2-6 Fractal subgroup image in Fig. 3-6b). Neurons readily grew processes on the electrodes, forming networks that followed their edges and made 90° turns at branch junctions (Fig. 3-6e, f, and k). It should be noted that fractals with more than 6 repeating levels were excluded from the experiment because including more levels would have closed the electrode geometry to form disconnected gaps.

To facilitate more detailed observations, three categories were defined that characterize the behavior of the cells within the SiO_2 gaps. Figure 3-6 shows columns of example images of the neurons and glia, along with schematic representations immediately below these images: the electrode region (Fig. 3-6a, e, i-1, and j-1), the ‘boundary’ region (Fig. 3-6b, f, i-2, and j-2), the ‘cluster’ region (Fig. 3-6c, g, i-3, and j-3), and the ‘desert’ region (Fig. 3-6d, h, i-4, and j-4). Furthest away from the electrodes were the desert regions, which featured a few individual neurons and small

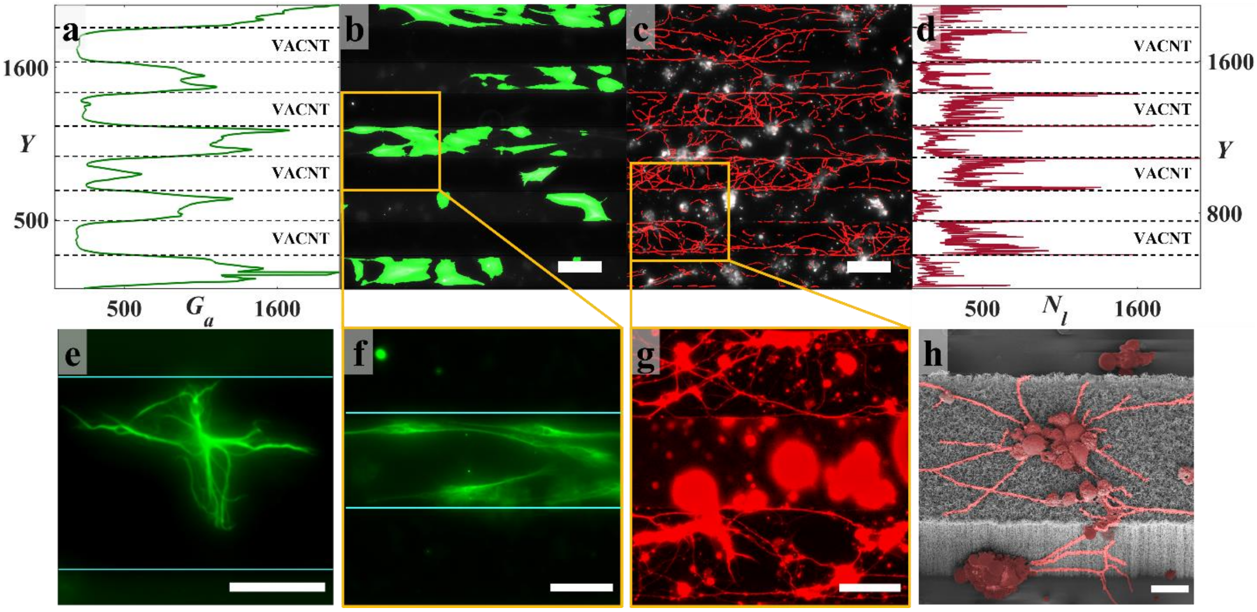

Figure 3-5. Neuronal and glial behaviors on electrodes from the Euclidean Rows group imaged at 17 DIV. (**a**) Sum of glial coverage areas shown in panel (**b**) (measured in pixels with a pixel width of 0.32 µm), revealing peaks within the SiO2 gaps. (**b**) Representative fluorescence image of GFAP labelled glial cells of a S75C75 electrode superimposed on the regions of glial coverage identified by the algorithm (green). (**c**) Representative fluorescence image of β-Tubulin III labeled neurons of the same region in (**b**) superimposed on the neuron processes identified by the algorithm (red). (**d**) Sum of process lengths (in pixels) shown in panel (**c**), revealing peaks coinciding with the electrode edges. (**e**) Representative fluorescence image of a GFAP labelled glial cell (green) on the VACNT top surface of a S75C75 electrode. (**f**) Zoom-in representative fluorescence image of GFAP labeled glial cells of the area marked in (**b**). (**g**) Zoom-in representative fluorescence image of β-Tubulin III labeled neurons (red) of the area marked in (**c**). (**h**) SEM image of a S50C50 Euclidean electrode taken at 40° tilt showing neuron clusters and connecting processes (false-colored) adhering to the top surface and sidewalls of the electrode (7 DIV). The dotted black lines in (**a**) and (**b**) and the cyan lines in (**e**) and (**f**) locate the edges of the VACNT rows. Scale bars are 100 µm in (**b**) and (**c**), 50 µm in (**e**), (**f**), and (**g**), and 10 µm in (h).

clusters with weak processes, along with a scattering of glial cells. Nearer to the electrodes, neurons aggregated into larger clusters physically connected to each other by bundles of processes and accompanied by significant numbers of glia. These are labelled as the cluster regions – in recognition of these typically larger clusters relative to those in the other regions. Many of these networks were connected to neurons on the electrodes via the boundary regions, which formed in some places along the electrode-gap interface. These boundary regions were composed of small to medium-sized

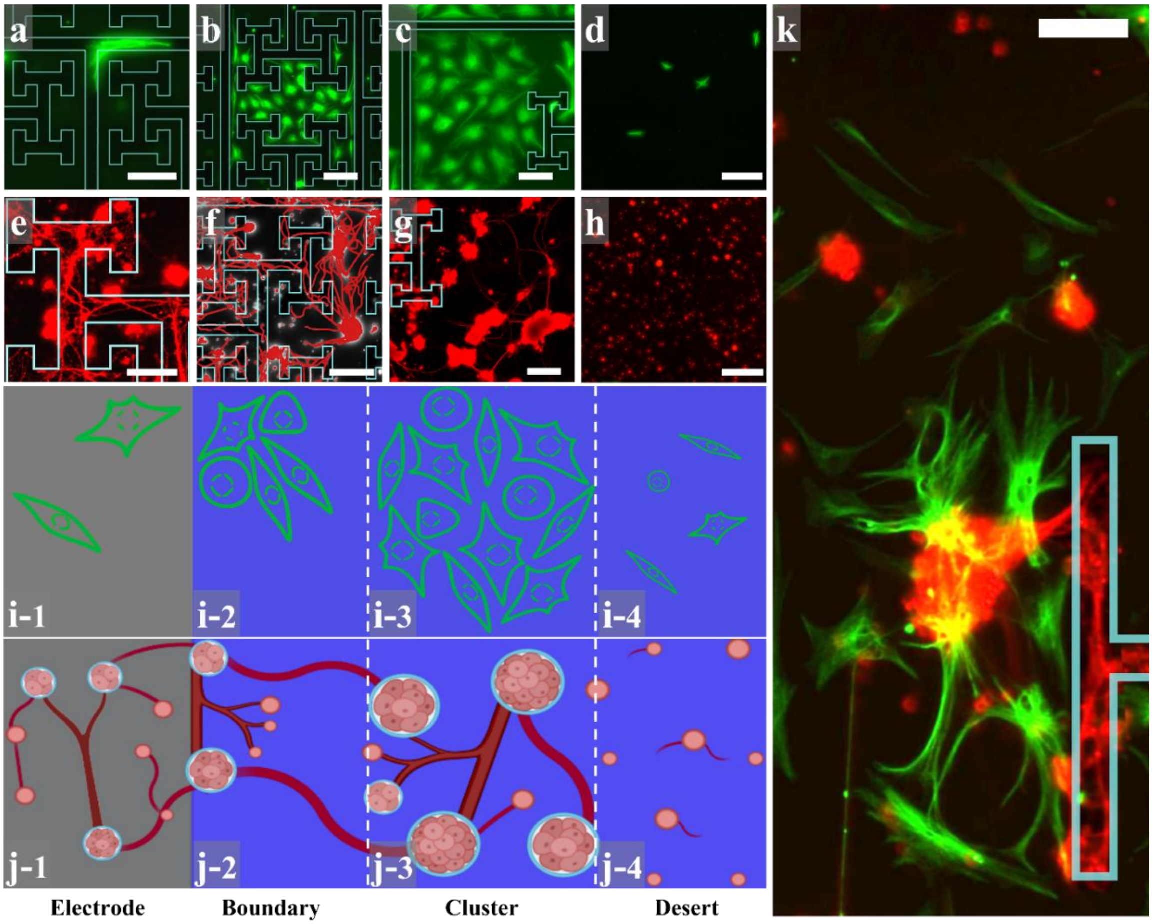

Figure 3-6. Examples of the assembly of neurons and glia on electrodes from the Fractal group. All fluorescence images within this figure show GFAP labelled glia (green) and β-tubulin III labelled neurons (red) imaged at 17 DIV. (**a**) The rare occurrence of glia following the 90° turn of a 2-6 electrode branch. (**b**) Glial coverage in the gap of a 2-6 electrode. (**c**) Glial coverage in the gap of a 1.1-4 electrode close to its branches. (**d**) Individual glia in a desert region away from the branches of a 1.1-4 electrode. (**e**) Neurons and their processes on a 2-6 electrode's branches. (**f**) Neuron clusters and processes in a 'boundary' region interacting with the neurons on the nearby branches of a 2-6 electrode. Neuron processes were semi-automatically traced using the Fiji simple neurite tracer and were false-colored. (**g**) Neuron clusters and processes forming a cluster neuronal network in the gaps of a 1.1-4 electrode. (**h**) individual neurons in a desert region of a 1.1-4 electrode far from the branches. (**i**) and (**j**) Schematic of the glial and neuronal network regions. (**i-1**) and (**j-1**) show the electrode with few glial cells and multiple processes connecting individual neurons and small to medium-sized clusters. (**i-2**) and (**j-2**) show the 'boundary' region featuring small to medium glial coverage regions and clusters connecting to each other and to neurons on the electrodes using multiple processes. (**i-3**) and (**j-3**) show the 'cluster' region featuring larger glial coverage and clusters with bundles of processes connecting them. (**i-4**) and (**j-4**) show the 'desert' region furthest from electrodes featuring very few glial cells, mostly individual neurons and very few processes. (**k**) Merged fluorescence image of glia and neurons on a 2-4 electrode showing all the different regions. Scale bars on (**a**), (**b**), (**c**), (**f**), and (**g**) are 100 µm, on (**d**) and (**h**) are 200 µm, and on (**e**) and (**k**) are 50 µm. The electrode edges are highlighted in cyan in (**a**), (**b**), (**c**), (**e**), (**f**), (**g**), and (**k**). Schematic panels were created in BioRender.

clusters and accompanied by occasional glial coverage. Figure 3-6k captures these various behaviors in one wide field of view (FOV).

The desert regions were most prevalent for the 1.1-4 Fractal subgroup. Their size diminished with increasing *D* and *m* until they vanished completely for the 2-5 and 2-6 Fractal subgroups. In contrast, the contributions of the boundary regions increased with *D* and *m*, with the 2-6 Fractal subgroup displaying the most processes connecting from the gaps to the electrodes (Fig. 3-6f). The cluster regions were prevalent for the $D = 1.5$-4 electrodes. Based on this *D* and *m* dependence, the sizes of the regions varied between the different electrodes. The importance of these regional behaviors along with their *D* and *m* dependence will be returned to later after quantifying the herding behavior of the various electrodes.

Having identified these three regions for the SiO_2 gaps within the electrodes from the Fractal group, it is prudent to revisit the cell behavior within the gaps of the Euclidean Rows group. These tended to be dominated by boundary regions with an absence of deserts. Although less prevalent in comparison to the Fractals group, some cluster regions were apparent within the Euclidean Rows group and their time evolution is shown in Fig. 3-7a, b, and c. These show three regions containing glial cells on both the electrode and gap surfaces at the 3, 7, and 17 DIV. Notably, through cell

Figure 3-7. Examples of fluorescence images of neurons and glia interacting with electrodes from the Euclidean Rows group and analysis of their behavior at all culture times. All fluorescence images within this figure show GFAP labelled glia (green) and β-tubulin III labelled neurons (red). (**a**, **b**, **c**) Glial cells on the VACNT and SiO_2 gaps of S75C75 electrodes at (**a**) 3 DIV, (**b**) 7 DIV, and (**c**) 17 DIV. (**d**, **e**, **f**) Merged fluorescence images of neuronal networks showing glia and neurons on different regions of the same electrodes shown in (**a**), (**b**), and (**c**). Panel (**g**) is a zoom-in on the region marked in (**f**) with the green channel removed in order to clearly highlight neuron processes bundling in the SiO_2 gap. Scale bars are 50 µm in (**a**) through (**g**). The cyan lines mark the edge between the VACNT electrode (top half) and SiO_2 gap (bottom half) in (**a**) through to (**f**). (**h**, **i**, **j**, **k**) Time evolution of G_{Si}, G_{CNT}, N_{Si}, and N_{CNT} for all Euclidean Rows electrodes averaged at each culture time. The glial cells follow a gradual increase in surface coverage across the culture time while the neuron processes show a peak at 7 DIV. The error bars correspond to the 95% confidence intervals. Stars in (**h**), (**i**), (**j**), and (**k**) indicate the degree of significance: * denotes $p \leq 0.05$, *** denotes $p \leq 0.001$, and **** denotes $p \leq 0.0001$.

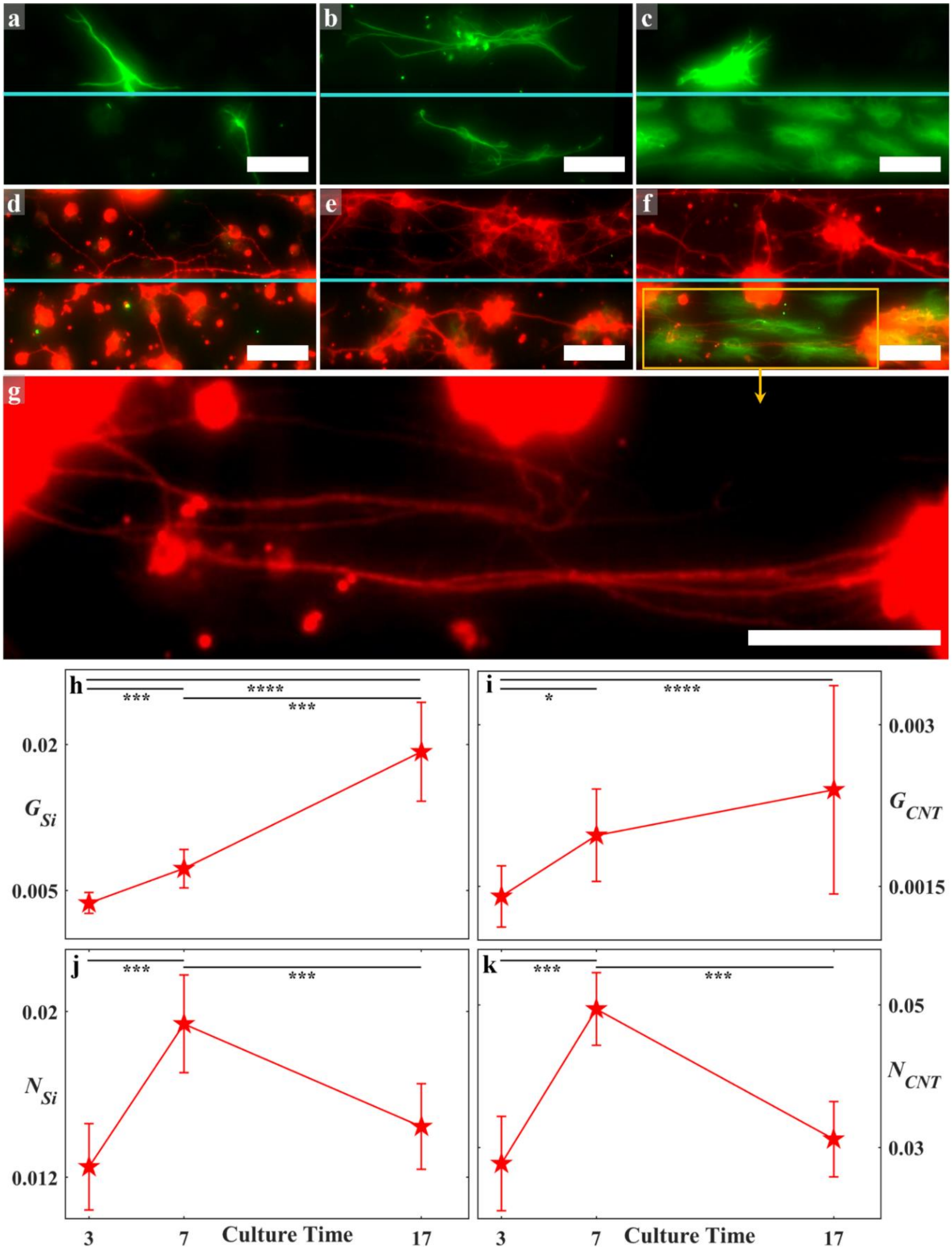
a
b
c
d
e
f
g
h
***
****
***
0.02
G_{Si}
0.005
i
*
****
0.003
G_{CNT}
0.0015
j
***
***
0.02
N_{Si}
0.012
k
***
***
0.05
N_{CNT}
0.03
3
7
Culture Time
17
3
7
Culture Time
17

division and growth, the glia have started to cover increasingly larger areas in the gaps by 17 DIV. Figure 3-7d, e, and f show different regions from the same electrodes as Fig. 3-7a, b, and c, now including the neuronal behavior. Whereas the neuron processes have grown from 3 to 7 DIV to connect the clusters, 17 DIV reveals fewer but larger clusters connected by bundles of processes, as shown in Fig. 3-7g. Visual inspection revealed that this signature of network formation was mildest on the electrode surfaces when compared to the gaps.

Quantification of Herding in the Euclidean Rows and Fractal Groups

The time evolution for the Euclidean Rows group is quantified in Fig. 3-7h, i, j, and k where, at each DIV, all the subgroups are combined. Consistent with the qualitative observations, G_{CNT} was an order of magnitude smaller than G_{Si} and both increased with time. In contrast, N_{CNT} and N_{Si} exhibited a peak at 7 DIV. Statistical comparisons between all DIV pairs revealed that G_{Si} was significantly lower at 3 DIV than at 7 and 17 DIV ($p \leq 0.001$ and $p \leq 0.0001$, respectively) and was significantly lower at 7 DIV than at 17 DIV ($p \leq 0.001$). G_{CNT} was also significantly lower at 3 DIV than at 7 and 17 DIV ($p \leq 0.05$ and $p \leq 0.0001$, respectively). N_{Si} and N_{CNT} were significantly lower at 3 and 17 DIV than at 7 DIV (both with $p \leq 0.001$).

Figure 3-8 summarizes the glial and neuronal behavior on the SiO_2 and VACNT surfaces of the Euclidean Rows and Fractal groups at 17 DIV with respect to their effective feature sizes and geometries. Figure 3-8a and c show the relationship of G_{Si} and N_{Si} with W_{Si} for the Euclidean Rows group at 17 DIV. For these plots, subgroups with identical W_{Si} but different W_{CNT} were combined (e.g., S25C25 was combined with S25C100 and so on) since statistical tests showed no significant differences between same W_{Si} subgroups, indicating that W_{CNT} did not significantly impact glial and neuronal growth in the gaps. In Fig. 3-8a, G_{Si} consistently increased with W_{Si} up to 75 µm and then decreased for W_{Si} = 100 µm (in agreement with qualitative observations of smaller glial coverage in the S100C100 SiO_2 gaps). However, a statistical test showed no significant differences in G_{Si} between any pairs with different W_{Si}. Figure 3-8c shows a gradual decrease in N_{Si} as W_{Si} increases with statistical tests revealing that N_{Si} at W_{Si} = 50 µm is significantly lower than N_{Si} at W_{Si} = 100 µm ($p \leq 0.05$). Figure 3-8b and d show the relationship of G_{CNT} and N_{CNT} with W_{CNT} for the Euclidean Rows group at 17 DIV. For these plots, the subgroups with identical W_{CNT} but different W_{Si} (i.e. all electrodes with W_{CNT} = 100 µm) were combined since statistical tests showed no significant differences between any pairs with the same W_{CNT}, indicating that W_{Si} did not significantly impact glial and neuronal growth on the VACNT surface. No clear increasing or decreasing trends were observed for G_{CNT} or N_{CNT} and no significant differences were detected between any pairs with different W_{CNT}.

Figure 3-8e-h summarizes the glial and neuronal behavior on both surfaces of the Fractal group as a function of D and m. G_{Si} peaked for the 1.5-4 subgroup, although statistical tests revealed a significant difference only between the 2-5 and 2-6 subgroups ($p \leq 0.05$). G_{CNT} was more than an order of magnitude smaller than G_{Si} and was almost constant across all Fractal subgroups, with the 1.1-4 subgroup having the lowest value. Statistical tests showed no significant differences in G_{CNT} between any pairing within the Fractal subgroups. N_{Si} and N_{CNT} gradually increased with D, but not with m. Statistical comparisons revealed no significant differences in N_{CNT} between any pairing within the Fractal subgroups. As for N_{Si}, the following Fractal subgroups were significantly different: 1.1-4 versus 2-5 ($p \leq 0.001$), 1.1-4 versus 2-6 ($p \leq 0.05$), and 1.5-4 versus 2-5 ($p \leq 0.05$).

In terms of herding, when grouping the electrodes from the 17 DIV Euclidean Rows group together, it was found that N_{CNT} was significantly higher than N_{Si} ($p \leq 0.0001$) and that G_{Si} was significantly higher than G_{CNT} ($p \leq 0.0001$) (Fig. 3-9a and b). Exactly the same result was found when grouping electrodes from the Fractal group together (Fig. 3-9c and d), demonstrating the herding capabilities of the VACNT-SiO_2 material system for both electrode geometries.

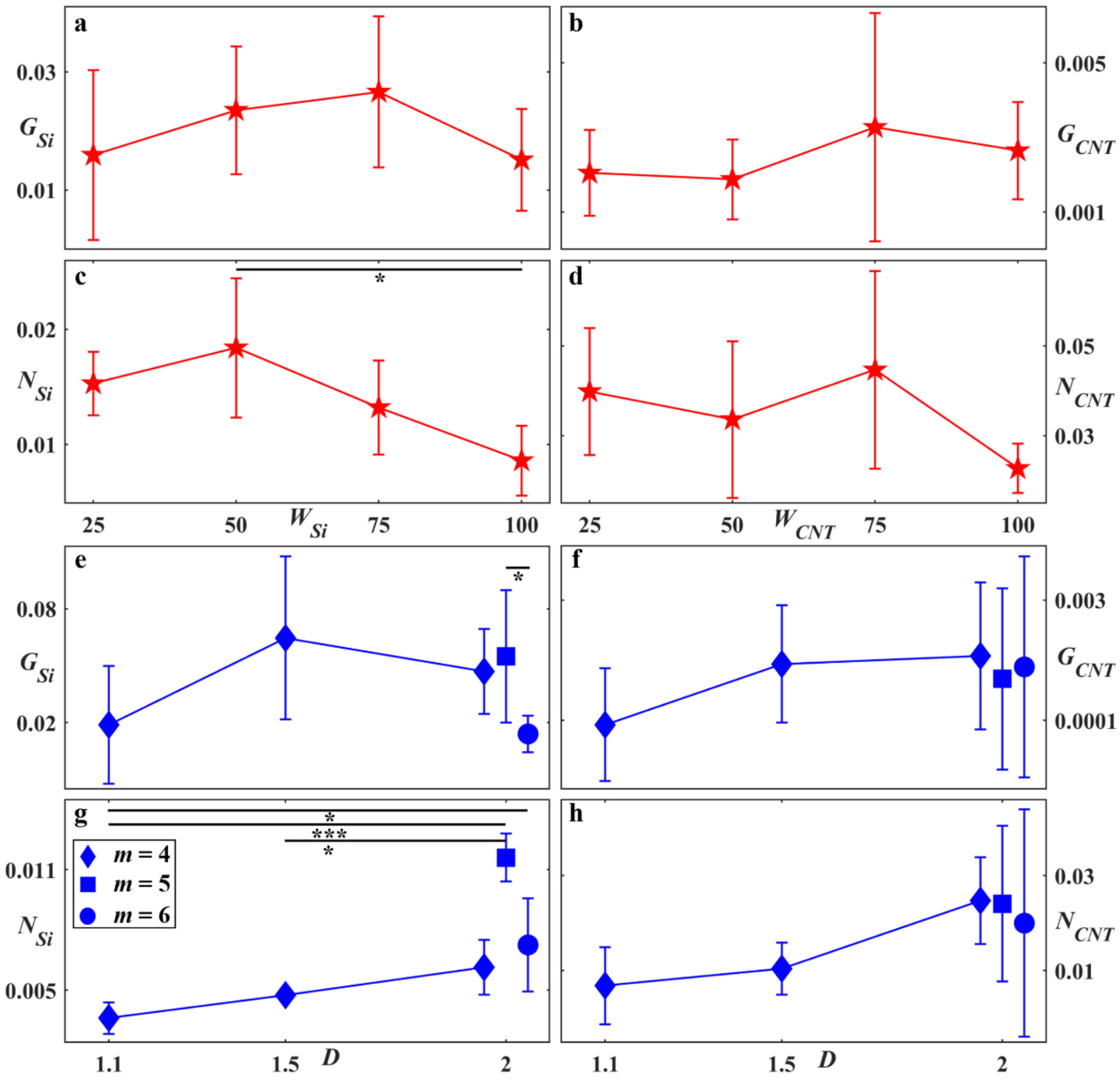

Figure 3-8. Glial and neuronal behavior for the Euclidean Rows and Fractal groups at 17 DIV. (**a**) G_{Si} median plotted against W_{Si}, (**b**) G_{CNT} median plotted against W_{CNT}, (**c**) N_{Si} median plotted against W_{Si}, (**d**) N_{CNT} median plotted against W_{CNT}. (**e**), (**f**), (**g**), and (**h**) show the G_{Si}, G_{CNT}, N_{Si}, and N_{CNT} medians, respectively, plotted against D. Because the 2-4, 2-5, and 2-6 Fractal subgroups share the same D value, they are all plotted at $D = 2$ with a slight shift from one another. In order of increasing m value, they are plotted from left to right as 2-4, 2-5, and then 2-6. The error bars correspond to the 95% confidence intervals. Stars in (**c**), (**e**), and (**g**) indicate the degree of significance: * denotes $p \leq 0.05$ and *** denotes $p \leq 0.001$.

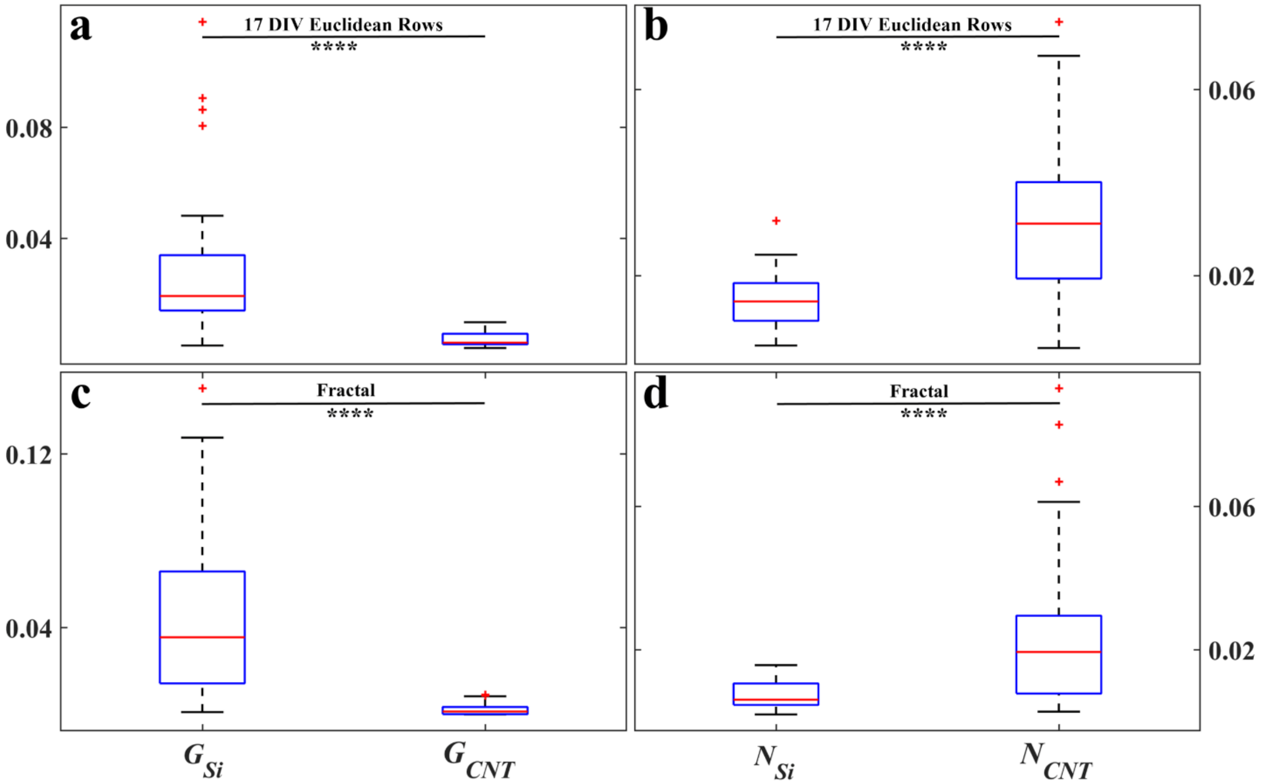

Figure 3-9. Comparison of glial and neuronal behavior on VACNT and SiO_2 surfaces for the Euclidean Rows and Fractal groups at 17 DIV. Statistical analysis showing boxplots comparing (**a**) G_{Si} and G_{CNT}, and (**b**) N_{Si} and N_{CNT} for the 17 DIV Euclidean Rows group. (**c**) and (**d**) are the same as (**a**) and (**b**) except that they show the results for the Fractal group. Stars in all panels indicate the degree of significance: **** denotes $p \leq 0.0001$. The red plusses indicate outliers within a group.

To further quantify the herding of neurons and glia, the parameters *N* and *G* were introduced. Adopting these measures, *N* and *G* values greater than 0.5 indicate successful guiding of neuron processes and glial cells to the desired VACNT and SiO_2 surfaces, respectively. The *N* and *G* values of the Euclidean Rows and Fractal groups are examined to provide an overall view of the herding power of each group. Analysis of the individual parameters N_{CNT}, N_{Si}, G_{CNT}, and G_{Si} and their dependences on the various electrode subgroups will be returned to later. Figure 3-10a shows a scatterplot of *N* versus *G* measured at 17 DIV for the Euclidean Rows and Fractal groups. The dashed black line represents a threshold, G_T, in glial herding at $G \sim 0.95$, beyond which no electrodes in the Euclidean Rows group were observed. Electrodes in the Fractal group, on the other hand, were not limited by this threshold and achieved significantly higher G values than the Euclidean Rows group ($p \leq 0.0001$). Based on G_T, the Fractal group was divided into two regimes in Fig. 3-10a: low ($G \leq G_T$) and high ($G > G_T$) regimes. Note the following overall observations for Fig. 3-10a: 1) almost all electrodes (90% in the Euclidean Rows group and 95% in the Fractal group) were successful at herding (i.e. both $G > 0.5$ and $N > 0.5$), again highlighting the favorable material qualities of the VACNTs for herding, 2) in the low regime, the Fractal group achieved significantly higher N values than the Euclidean Rows group ($p \leq 0.001$), 3) in the high regime, the Fractal group's enhanced neuron herding collapsed such that they shared the same approximate range of N values as the Euclidean Rows group.

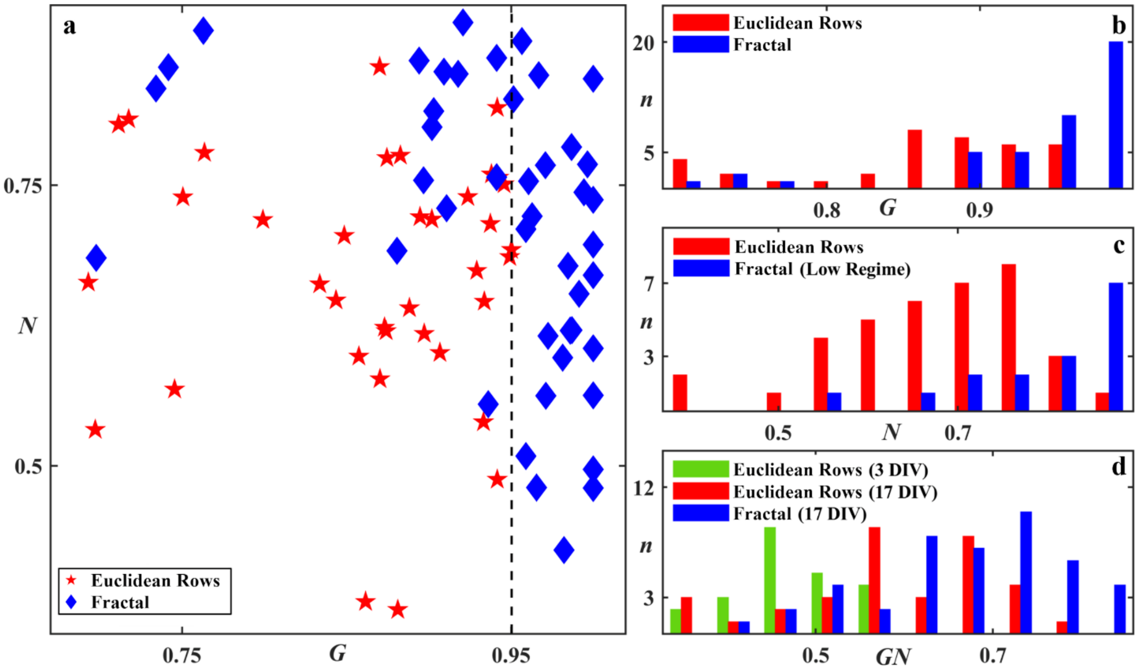

Figure 3-10. Quantification of the overall herding of neurons and glia for the Euclidean Rows and Fractal groups. (**a**) Scatterplot of N (neuron herding) versus G (glial herding) for the Euclidean Rows and Fractal groups at 17 DIV where each data point represents one electrode (G is plotted in the range of 0.5 to 1 for clarity, but it should be noted that there was one outlier in the Euclidean Rows group with $G < 0.5$ that, though not shown here, was included in the statistical analysis of the groups). The dashed line marks the threshold value in G that no Euclidean Rows electrode surpassed. (**b**) Histogram of the number of electrodes, n, with a given G for the Euclidean Rows and Fractal groups at 17 DIV. (**c**) Histogram of the number of electrodes, n, with a given N for the Euclidean Rows and low regime Fractal groups at 17 DIV. (**d**) Histogram of the number of electrodes, n, with a given GN for the Euclidean Rows group at 3 and 17 DIV as well as the Fractal group at 17 DIV.

The combined herding parameter *GN* was also introduced to quantify the power of the electrode groups to simultaneously herd both neurons and glia. At 17 DIV, the Euclidean Rows group exhibited significantly lower *GN* values compared to the Fractal group ($p \leq 0.01$). Figure 3-10d shows the histogram of the number of electrodes, n, with a given *GN* value for Euclidean Rows (3 and 17 DIV) and Fractal (17 DIV) groups. This indicates that not only did time evolution increase the combined herding power, but also that this power was amplified at 17 DIV for the Fractal group when compared with the Euclidean Rows group.

Discussion of Herding in the Euclidean Rows and Fractal Groups

The experiments detailed throughout this chapter relied on the well-established behavior that glia accumulate on smooth rather than textured surfaces[143,151,152]. Whereas many previous studies investigated pure glial cultures on substrates made of a single material featuring different textures, the work presented within this chapter focuses on retinal neuron-glia co-cultures on a multi-material system (smooth SiO_2 and textured VACNT) to provide confirmation that different cell types within a co-culture could be ‘herded’ onto different regions through a manipulation of surface texture[69]. To achieve this, micron-scale lateral patterning of the VACNTs was combined with their surface nano-roughness effects. This contrasts with previous studies that used unpatterned nano-rough surfaces[127,143,151], nano-ripples and micro-grooves[152], and nanowires[69]. While the work presented here found in general that the cell morphologies on the two surfaces were consistent with those observed in previous studies, the relatively large VACNT heights used in these experiments were shown to be an important factor in the system’s design - glia residing on the SiO_2 surfaces never extended processes over nearby VACNT surfaces which acted as barriers to the glia and therefore guided glial coverage across the SiO_2 surface.

The patterned VACNTs examined in this chapter follow previous studies that have examined the manipulation of neuronal networks using patterned substrates to guide cell attachment[66,122,165].

Based on previous studies examining the migration of neurons[166–169], the neurons within the VACNT-SiO_2 material system examined here are expected to utilize neuron-substrate forces to migrate across the smooth SiO_2 surfaces with average speeds of 10-20 µm/h. As such, neurons that initially landed proximal to the VACNT electrode branches had a high chance of their growing processes finding the electrode edges during the first few hours of culturing. The strong cell-VACNT adhesion forces experienced by these neurons would have competed with the neuron-neuron aggregation forces, presumably slowing down cluster formation and resulting in the emergence of the boundary regions (note that these cell-VACNT adhesion forces were not sufficiently strong to stop cluster formation completely – as indicated by the observation of mainly small to medium-size clusters on the electrode surfaces and N_{CNT} exhibiting a rise and fall in complexity with culture time – see Fig. 3-7k). Neurons that landed further away from the electrodes would have been less likely to encounter their edges and would therefore have experienced fewer anchor points, mainly in the form of other cells or rough impurities on the surface. In these regions, the neurons therefore had a higher tendency to aggregate and follow cluster network formation. The desert regions were likely caused by neurons anchored to the VACNT electrodes secreting chemical signals, regulating ion fluxes, neurotransmitters, and specialized signaling molecules[170] which encouraged stronger interaction between neurons on the VACNTs and on the nearby SiO_2 gaps.

These developments would have been accompanied and supported by an interplay with glial cells. Glia likely started proliferating through cell division and growth and, in this process, acted as a support system for the neurons, following chemical cues[170] that increased their surface coverage close to the neuron-rich regions[171,172]. This emergence of glial coverage was then likely to support not only neuronal survival and process development, but also migration along their fibers[173,174] towards the electrodes. These observations agree with other studies on smooth surfaces showing that in glial-neuronal co-cultures, glia direct neurons to glial-rich regions using chemical cues[175]. As a sign of their subtle growth interaction, frequent cases of neuron process development were observed on top of regions covered with glia (Fig. 3-6k and Fig. 3-11).

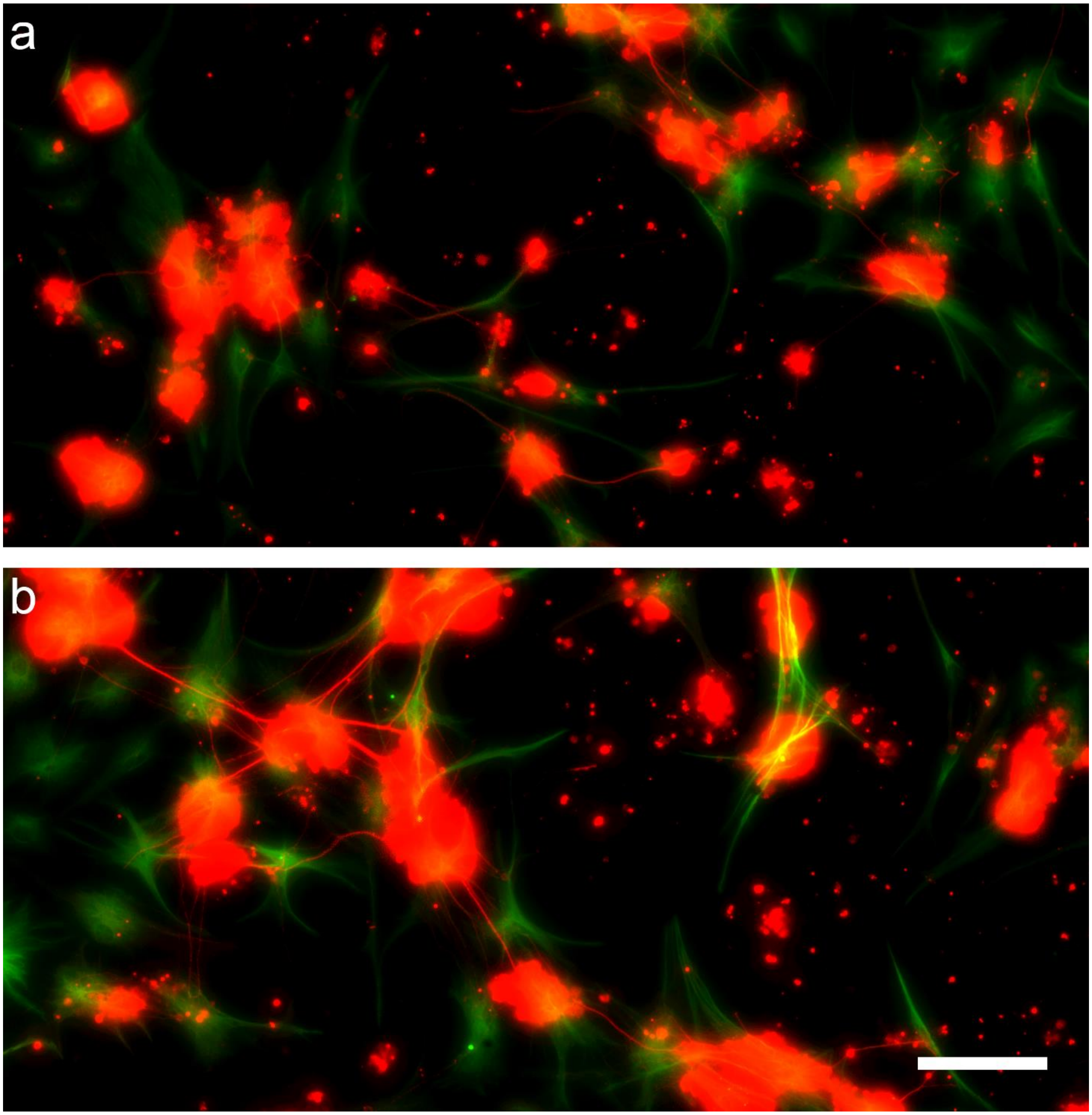

Figure 3-11. Fluorescence images of neuron clustering and process growth in close proximity to glia-covered regions. The images in (**a**) and (**b**) show two different regions of β-tubulin III labelled neurons (red) and GFAP labelled glia (green) growing on a SiO_2 surface. The location of the neuronal clusters and processes are heavily correlated with the regions covered by glia. The scale bar in the bottom right corresponds to 100 μm and applies to both (**a**) and (**b**).

To place the results of this work in the context of studies examining neuron-glia interactions, it is informative to now consider how the fractal properties of the electrodes influence these inter-dependent networks of neurons and glia. Although previous studies have modelled individual cell locomotion through environments with complicated geometries[168,176,177], the discussion above emphasizes the additional roles played by cell growth and assembly behavior (e.g., glial cell division and neuron process bundling and pruning) when considering cells connected in networks. The fractal electrode design integrates two sets of related, multi-scaled patterns – the branches and the gaps – that both impact cell organization favorably. The repeating patterns of the branches build long edges that interface with the gaps. The consequence for neurons and glia is that the fractal patterns with high D and m values offer increased accessibility of electrode edges to the gaps, so increasing favorable interactions between cells in both regions. More specifically, the large edge lengths are likely to accommodate the neurons' tendency to grow processes along the top and bottom edges of the electrode sidewalls, and for the sidewalls to act as anchor points for neuron clusters in the gaps to adhere to. These effects can be seen in the large density of processes connecting the neuronal networks on the VACNT electrodes to those in the SiO_2 gaps observed in Fig. 3-6f. Furthermore, the close proximity of the electrode branches to the surrounding gaps, which ensures closeness of the neuron-rich electrodes to the glial cells in the gaps, is crucial because neurons and glia thrive when in such close proximity[178].

Turning to the impact that the SiO_2 gap sizes have on cell behavior, it is important to understand how the D and m values of the fractal patterns affect the 'openness' and scaling of the gaps. Low D and m value fractals provide gaps that scale up in size quickly and the overall pattern is therefore much more open, whereas the gaps in high D and m value fractals are much tighter and scale up in size slowly. Consequently, low D and m value fractals offer much more physical freedom within the gaps, while high D and m value fractals result in a more restrictive environment.

Combining this effect with the impact that *D* and *m* have on the electrode edge length and proximity of electrode branches to the surrounding gaps, high *D* and *m* value fractals are expected to encourage boundary regions and reduce desert regions since there are no large gaps far away from branches. In contrast, low *D* and *m* value fractals are expected to minimize boundary regions and encourage deserts with their vast, empty gaps. Forming between the boundary and desert regions, growth of cluster regions is expected to be encouraged for mid *D* and *m* value fractals. Taken together, this model suggests that for the fractal patterns examined in this work, those with mid to high *D* and 4 to 5 repeating levels will promote the most favorable cell interactions. They are likely to enhance glial coverage inside their multi-scaled gaps without restricting the glia and prevent the formation of large deserts. These glia will also fuel the formation of the neuronal networks in the cluster regions. The large edge length of the fractal VACNT branches combined with their close proximity to the SiO_2 gaps would then enhance the growth of neuron processes in the boundary region and facilitate connection of the neuronal networks in the cluster region to those on the VACNT branches.

Revisiting the examination of glial coverage in the SiO_2 gaps of the Euclidean Rows group (Fig. 3-8a), G_{Si} did not show a statistically significant increase with gap width up to the largest investigated gap of width W_{Si} = 100 μm. This suggests that, although they likely benefitted from being proximal to the neuron-rich electrodes, their gap sizes were insufficient to offer the necessary freedom to encourage large glial coverage. Figure 3-12 shows fluorescence images emphasizing that the SiO_2 gaps in the Fractal group start near the same size scale as the Euclidean Rows group and then repeat at increasingly larger sizes. The advantage of connecting to larger gaps for the 1.5-4, 2-4, and 2-5 Fractal subgroups is demonstrated by plotting the median G_{Si} versus the minimum gap width, $W_{Si\text{-}min}$, (the $W_{Si\text{-}min}$ values for the 1.1-4, 1.5-4, 2-4, 2-5, and 2-6 Fractal subgroups are 56 μm, 101 μm, 134 μm, 61 μm, and 25 μm, respectively – see Fig. 3-13 for a schematic illustrating the measurement of $W_{Si\text{-}min}$). The median G_{Si} values for these 3 Fractal subgroups are notably higher than the Euclidean Rows subgroups with similar W_{Si} values (note that $W_{Si} = W_{Si\text{-}min}$ for the electrodes in the Euclidean Rows group). In particular, the G_{Si} values of the 2-5 and 1.5-4 Fractal subgroups are significantly higher than the Euclidean Rows subgroups with W_{Si} = 50 µm and 100 µm, respectively (both with $p \leq 0.05$). In contrast, the 2-6 Fractal subgroup held no advantage over the Euclidean Rows group because their $W_{Si\text{-}min}$ gaps were not connected to gaps sufficiently large to encourage proliferation. They consequently lost the interconnected, multi-scaled freedom of afforded to the 1.5-4, 2-4, and 2-5 Fractal subgroups, and instead approached the more filled character of the Euclidean Rows group (i.e., higher electrode areas, A_{CNT}, and lower gap areas, A_{Si} - Table 3-1). The 1.1-4 Fractal subgroup held no advantage because their $W_{Si\text{-}min}$ gaps connected to vast regions dominated by deserts. This behavior is supported by the qualitative inspections of the images shown in Fig. 3-12. In summary, the 1.1-4 Fractal subgroup was too ‘open’, and the 2-6 Fractal subgroup and Euclidean Rows group were too ‘restricted’. In this spectrum, the 1.5-4, 2-4, and 2-5 Fractal subgroups appear to have the optimal balance for glial coverage provided through integration of a fractal distribution of small and large interconnected SiO_2 gap areas proximal to interpenetrating fractal electrode branches.

To quantify the impact of this glial cell behavior on neuron process length in the gaps, N_{Si} was plotted as a function of G_{Si} in the scatterplot of Fig. 3-14a. The electrodes from the low and high regimes within the Fractal group are marked with different symbols to detect any possible variations in trends for N_{Si} or G_{Si} between the two regimes. Although the low regime was limited to lower G_{Si}, some of the high regime also appeared in this low range, indicating that low G_{CNT} values must also have played a role in achieving the high G herding powers associated with the high regime. The similarity of these two regimes in terms of their N_{Si} versus G_{Si} relationship indicates a common cell behavior in the gaps, which will now be explained in terms of an interplay of the boundary, cluster, and desert regions.

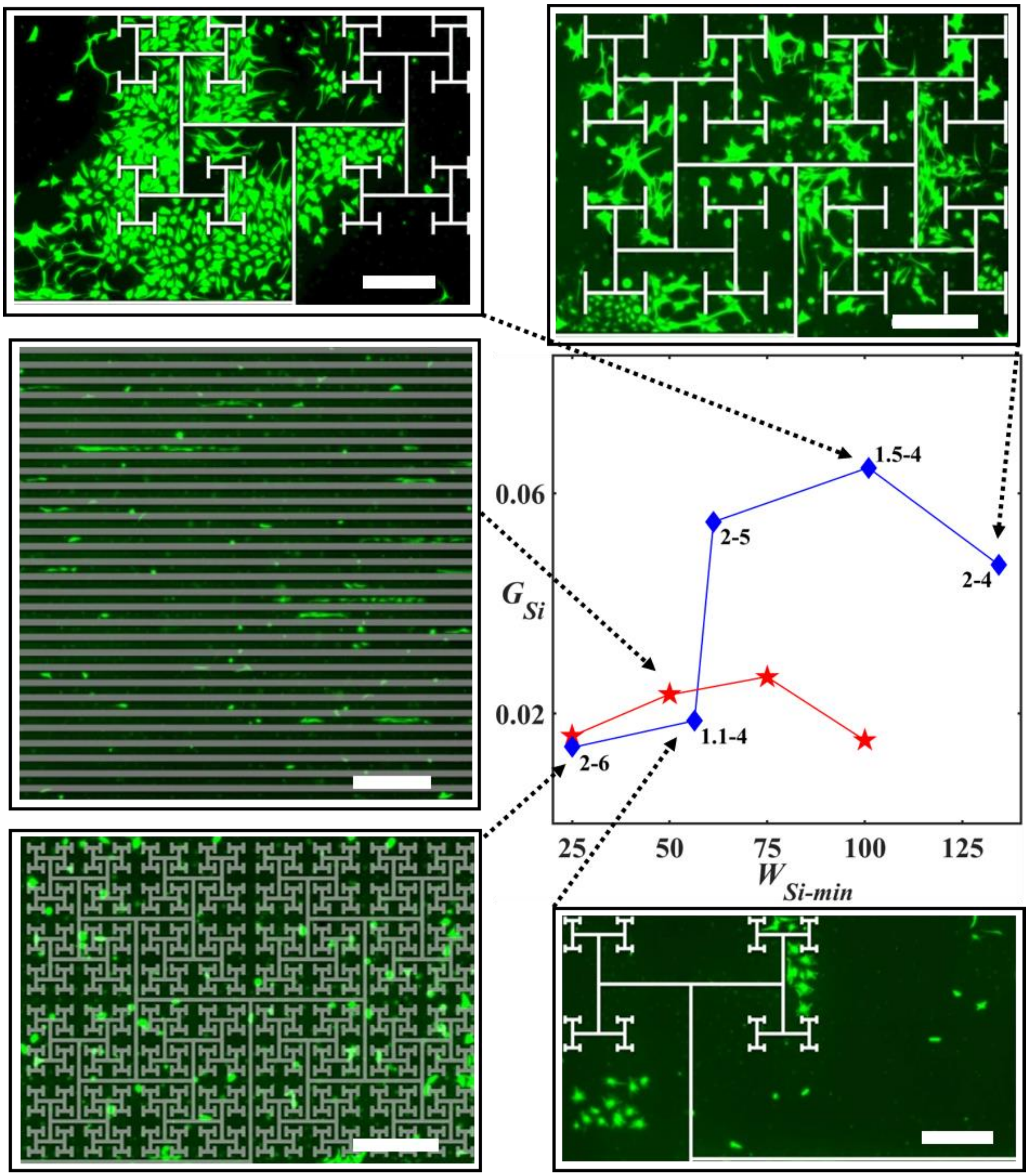

Figure 3-12. Study of the impact of SiO_2 gap size on glial behavior. Representative fluorescence images of GFAP labelled glial cells (green) at 17 DIV are shown for one quarter of the full images of electrodes from the 1.1-4 (bottom right), 1.5-4 (top left), 2-4 (top right), and 2-6 (bottom left) Fractal subgroups along with the S50C50 (middle left) Euclidean Rows subgroup. White or gray masks have been imposed on to the images to highlight the locations of the VACNT electrodes and the lower-right scale bars are 500 µm. A plot of the median G_{Si} against $W_{Si\text{-}min}$ at 17 DIV is also shown. The dashed arrows connect the images to their corresponding datapoints in the plot. The blue diamond symbols represent the Fractals group and the red pentagrams represent the Euclidean Rows group. Note that $W_{Si\text{-}min} = W_{Si}$ for the Euclidean Rows group and that there are 4 datapoints corresponding to the 4 distinct widths of SiO_2 gaps within this group.

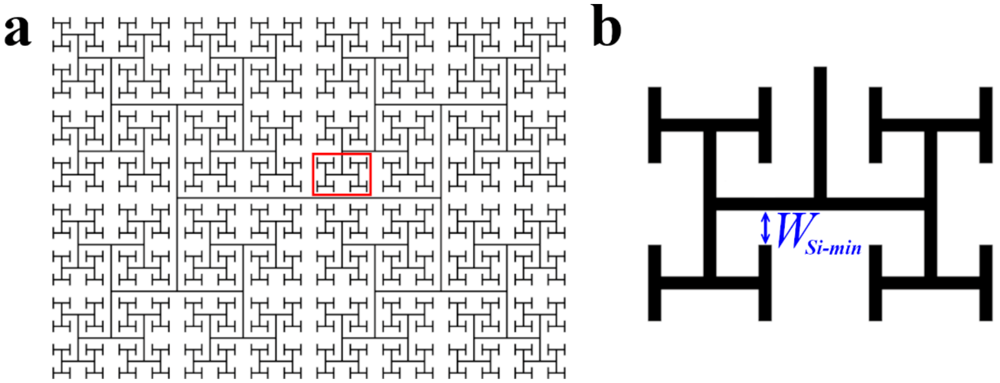

Figure 3-13. Schematic indicating the measurement of the minimum gap width for the 2-5 Fractal subgroup. (**a**) Schematic image of the 2-5 Fractal subgroup. (**b**) Marker indicating the measurement of the minimum gap width, $W_{Si\text{-}min}$, using a zoom-in on the region within the red box shown in (**a**). The same method for measuring $W_{Si\text{-}min}$ is applied to all Fractal subgroups.

To quantify the impact of this glial cell behavior on neuron process length in the gaps, N_{Si} was plotted as a function of G_{Si} in the scatterplot of Fig. 3-14a. The electrodes from the low and high regimes within the Fractal group are marked with different symbols to detect any possible variations in trends for N_{Si} or G_{Si} between the two regimes. Although the low regime was limited to lower G_{Si}, some of the high regime also appeared in this low range, indicating that low G_{CNT} values must also have played a role in achieving the high G herding powers associated with the high regime. The similarity of these two regimes in terms of their N_{Si} versus G_{Si} relationship indicates a common cell behavior in the gaps, which will now be explained in terms of an interplay of the boundary, cluster, and desert regions.

Beginning with the Euclidean Rows group which lies on the left side of Fig. 3-14a, as expected from their relatively low G_{Si} values revealed in Fig. 3-12, these electrodes showed a dominance of boundary regions due to a lack of large gaps to support deserts and a reduction of the cluster networks because of small glial coverage. However, cluster networks were evident for some electrodes within the Euclidean Rows group with W_{Si} down to 50 µm. This was indicated by the significant decrease in N_{Si} ($p \leq 0.05$) seen in Fig. 3-8c potentially due to increased pruning and

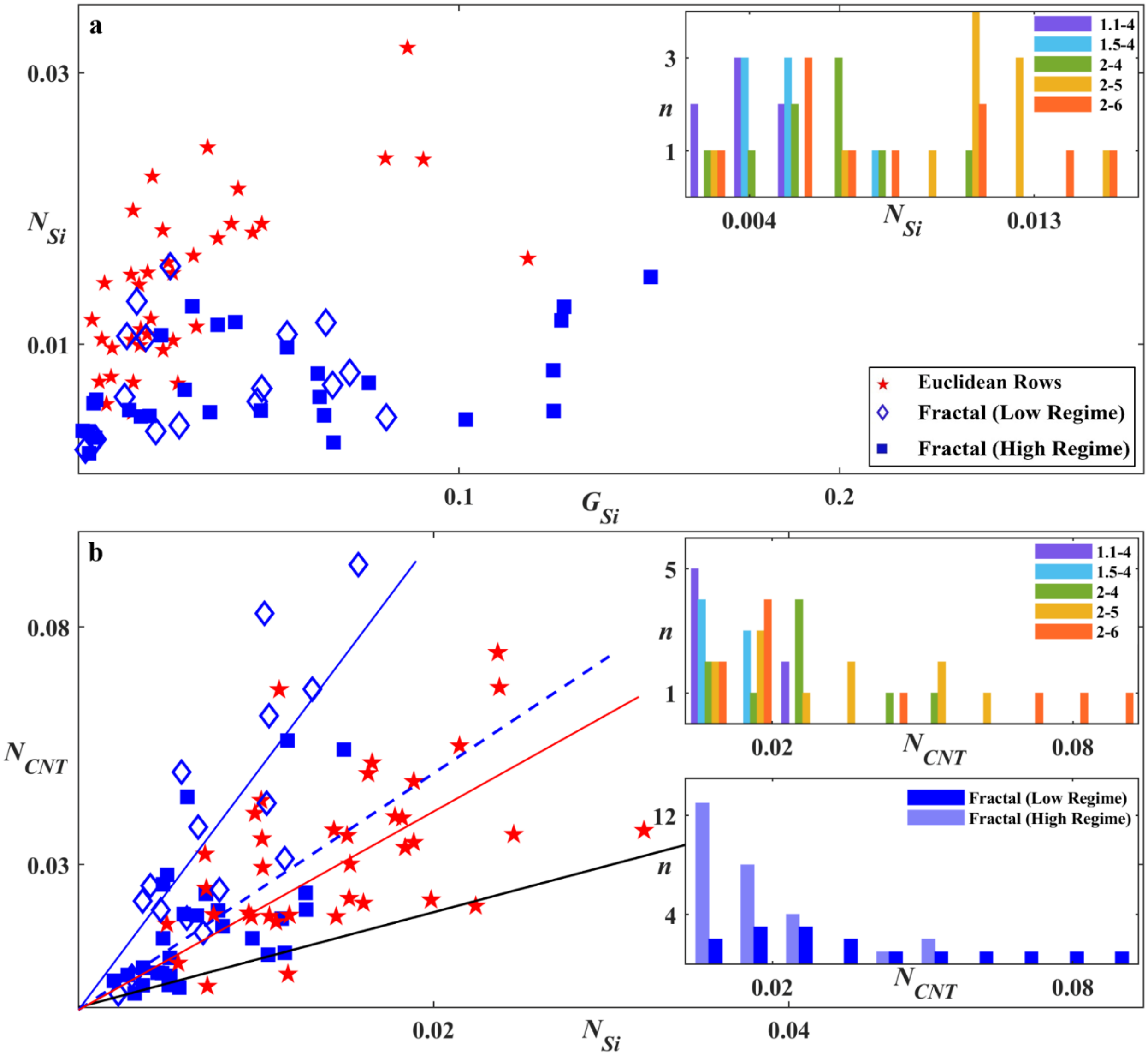

Figure 3-14. Study of the relationship between neuron and glial behavior on the SiO_2 surfaces and between neuronal behavior on the SiO_2 and VACNT surfaces for the Fractal and Euclidean Rows groups. (**a**) Scatterplot of N_{Si} versus G_{Si} for 17 DIV Euclidean Rows group (red pentagram) as well as the low (diamond) and high (filled square) regimes of the Fractal group. The inset of (**a**) provides a histogram of the number of electrodes, *n*, with a given N_{Si} for all Fractal subgroups. (**b**) Scatterplot of N_{CNT} versus N_{Si} for 17 DIV Euclidean Rows group as well as the low and high regimes of the Fractal group. The solid black line represents the $N_{CNT} = N_{Si}$ condition. The solid blue, dashed blue, and solid red lines are fits through zero for the Fractal group's low and high regimes, and the Euclidean Rows group, respectively. The top inset of (**b**) provides a histogram of the number of electrodes, *n*, with a given N_{CNT} for all Fractal subgroups. The bottom inset of (**b**) provides a histogram of the number of electrodes, *n*, with a given N_{CNT} for Fractal group's low and high regimes.

bundling as the edges became less influential as the gap widths increased from 50 μm to 100 μm. Nevertheless, the Euclidean Rows group was in general boundary-dominated with large N_{Si} values and the observed sharp increase in N_{Si} with G_{Si} (Fig. 3-14a) was likely due to the supporting role of glial cells on neuronal survival and function. The slight dampening of this rise seen at higher G_{Si} might again be due to the presence of pruning and bundling of the cluster network.

In comparison, the Fractal group featured far fewer neuron processes in the gaps as quantified by the lower N_{Si} values across the full range of G_{Si} (the few data points from the Fractal group residing in the scatter of the Euclidean group's data are the 2-6 Fractal subgroup, which were previously pointed out to have collapsed into the Euclidean condition in terms of their gap behavior). To determine the origin of this suppression in N_{Si}, the histogram of the number of electrodes, n, with a given N_{Si} for each of the Fractal subgroups is plotted in the Fig. 3-14a inset (the equivalent box plot is shown in Fig. 3-15). In general, it is seen that increases in D and m produced higher N_{Si} values. For example, most of the 1.1-4 subgroup is located on the histogram's left side because its vast deserts dominated over the boundary and cluster regions and supported few processes. The 1.5-4 subgroup is next because their large cluster networks efficiently bundled and pruned processes. The increasing role of the process-rich boundary regions explains the increase in N_{Si} when moving from the 2-4 to the 2-5 subgroup. This dependence of N_{Si} on D and m is re-iterated in Fig. 3-8g. (A speculative explanation for the 2-6 subgroup having lower N_{Si} values than the 2-5 subgroup is that a combination of the lower G_{Si} of the 2-6 subgroup and the relative increase in the proximity of their electrode branches to the surrounding SiO_2 gaps would increase the tendency of processes to grow on the VACNTs and their edges rather than the gaps.) Due to the subtle nature of the N_{Si} suppression process, along with the scattered data it generates, fitting any form to the N_{Si} versus G_{Si} trend for both the Euclidean Rows and Fractal groups has been avoided.

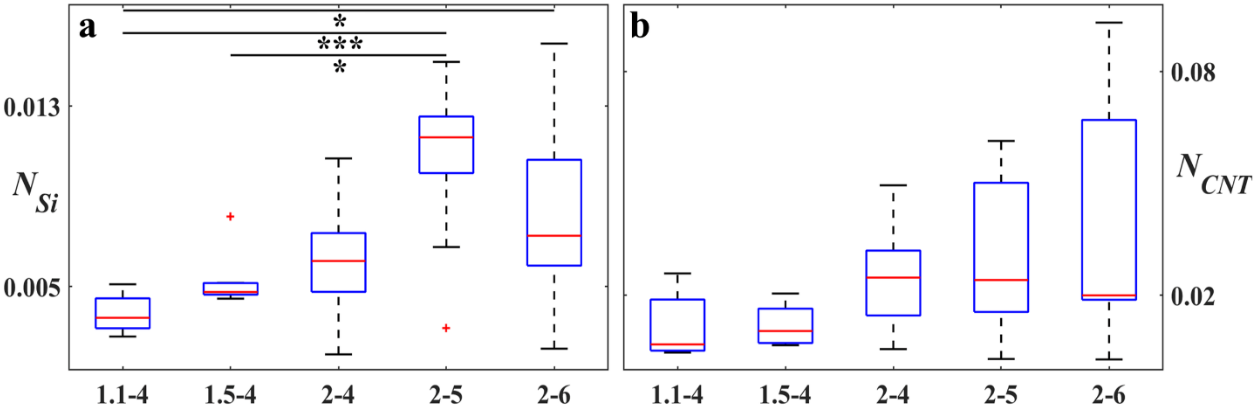

Figure 3-15. Study of neuronal behavior on the SiO_2 and VACNT surfaces for the Fractal group. Statistical analysis showing boxplots for N_{Si} (**a**) and N_{CNT} (**b**). Stars in (**a**) indicate the degree of significance: * denotes $p \leq 0.05$ and *** denotes $p \leq 0.001$. The red plusses in panel (**a**) indicate outliers. No significance was observed in N_{CNT}.

Equipped with this picture of how G_{Si} and N_{Si} describe cell behavior in the gaps, their interaction with the electrode branches will now be examined. The scatterplot of Fig. 3-14b illustrates how N_{Si} varies with N_{CNT} for the Euclidean Rows group as well as the low and high regimes of the Fractal group. The solid black line (given by $N_{Si} = N_{CNT}$) represents the threshold for successful herding. Interestingly, almost all electrodes reside above this threshold. Additionally, N_{CNT} increases with N_{Si} for each of the three groups, as indicated by their fit lines. Although these linear guides are useful for comparing the data to the $N_{Si} = N_{CNT}$ condition, they are not meant to imply a strictly linear behavior. A comparison of Fig. 3-14a inset with Fig. 3-14b top inset (and the equivalent box plots in Fig. 3-15) highlights this trend for the Fractal group: the increase in N_{CNT} values with the rise in D and m has a similar trend to that of the N_{Si} increase. Fractal subgroups with a large number of neuron processes in the gaps and a large electrode interface generated large N_{CNT} values. This is also revealed in Fig. 3-8g, h.

Although the fractal parameters influence N_{CNT}, they are not sufficiently powerful to produce a statistically significant difference between the low regime of the Fractal group and the Euclidean Rows group, a result that highlights the strong adhesive properties of the VACNT surface (this is also true of other geometric factors, as indicated by the lack of N_{CNT} dependence on electrode width within the Euclidean Rows group as shown in Fig. 3-8d). For similar N_{CNT} values within the Euclidean Rows and Fractal groups, the higher N_{Si} values of the Euclidean Rows group (Fig. 3-14a) led to the observed drop in the data gradient when comparing the Euclidean Rows (red slope in Fig. 3-14b) and Fractal (blue slope) groups. Crucially, although the Euclidean Rows and Fractal groups supported similar numbers of processes, N_{CNT} does not reflect their advantageous locations on the Fractal group electrodes. A large density of neurons were located at electrode branch edges (Fig. 3-5c and d) close to the glial coverage in the gaps which ensures neuronal health[179,180]. The longer edge lengths of the electrodes within the Fractal group therefore promoted this potential health advantage.

Finally, the collapse in the gradient (N_{CNT} versus N_{Si}) when moving from the low to high regime within the Fractal group was caused by a drop in N_{CNT} (lower inset of Fig. 3-14b). This may have been induced by a change in glial behavior between the two regimes. In particular, in addition to the high regime supporting G_{Si} values larger than those reached in the low regime, G_{CNT} dropped when moving to the high regime. The G_{CNT} values of the Euclidean Rows group were significantly higher than those of the Fractal group's high regime ($p \leq 0.0001$). Additionally, although no statistically significant difference in G_{CNT} was observed between any of the Euclidean subgroups, when grouping together all Euclidean subgroups with $W_{CNT} = 100$ µm, they have a significantly higher G_{CNT} value ($p \leq 0.05$) than the Fractal group (which has $W_{CNT} = 20$ µm). It is therefore likely that the larger widths of the Euclidean electrodes were less restrictive to glial growth and that this was responsible for their high G_{CNT} values. The majority of the electrodes within the Fractal group (61%) lie in the high regime because, along with their higher G_{Si} values, their narrow electrode widths generated small G_{CNT} values. However, there isn't a clear geometric dependence in terms of which Fractal subgroups have high or low G values due to 'natural' (i.e., not originating from differences in fabrication and/or culture batches, etc.) statistical variations in the G_{Si} and G_{CNT} values.

When moving from the low to high regime within the Fractal group, the increase in the G_{Si} median value was not statistically significant whereas the drop in G_{CNT} was ($p \leq 0.0001$). A possible scenario therefore is that the significant drop in N_{CNT} ($p \leq 0.01$) is being driven by G_{CNT} (Fig. 3-16). The electrode's material properties that caused neurons to thrive, and thereby allowing for them to extend many processes, needed to be supplemented by chemical cues provided by a small number of glial cells on the VACNT surface. The collapse observed in Fig. 3-10 and Fig. 3-14b would likely be triggered if this number fell below a critical value. Electrodes with longer edges that promoted stronger process interactions with the boundary regions might be expected to be more robust in terms of preventing this collapse. Accordingly, in general it is found that the Fractal subgroups that were less prone to collapse were those with higher *D* and *m* values.

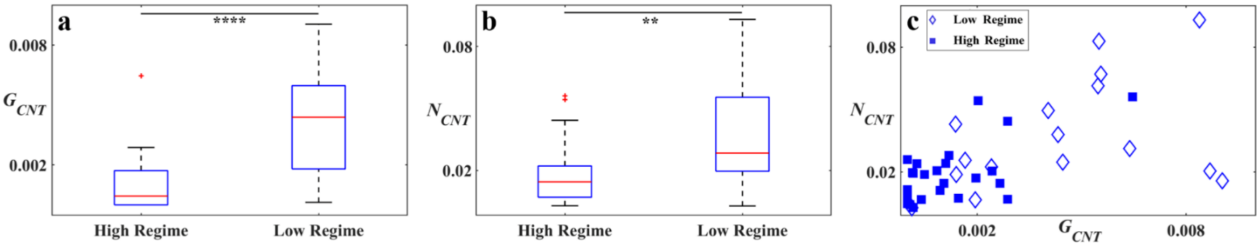

Figure 3-16. Comparison of neuronal and glial behavior on the VACNT surface for the low and high regimes within the Fractal group. Statistical analysis showing boxplots for G_{CNT} (**a**) and N_{CNT} (**b**). Scatterplot of N_{CNT} versus G_{CNT} (**c**) showing the different cell behaviors on the VACNT and SiO_2 surfaces for the low and high regimes. No significance was observed in N_{Si} and G_{Si} between the two regimes. Stars in (**a**) and (**b**) indicate the degree of significance: ** denotes $p \leq 0.01$ and **** denotes $p \leq 0.0001$. The red plusses in panels (**a**) and (**b**) indicate outliers.

Comparing the Impact of the Grid and 2-5 Fractal Electrode Geometries on Cell Behavior

Having assessed the behavior of the networks of neurons and glia that formed on the Euclidean Rows and Fractal electrode geometries and developed a model for understanding the characteristics of the networks, the model will now be applied in a comparison between the Grid and 2-5 Fractal electrode designs. This specific pair was chosen as comparators for a number of reasons. Both geometries provide a fully connected VACNT surface, while having distinctly different behavior with respect to the connectedness of their SiO_2 surface. The gaps in the 2-5 Fractal provide an ‘open’ system, while the isolated chambers of the Grid provide a ‘closed’ system (see Fig. 3-1b and c). These contrasting behaviors allow for an investigation of the impact of SiO_2 gap connectedness on the herding of neurons and glia. Additionally, the 2-5 Fractal was chosen out of all the other Fractal designs due to its high performance with respect to N_{Si} and N_{CNT}, while simultaneously allowing for a large G_{Si} (Fig. 3-8c, g, and h). Further, the size of the minimum gap width, $W_{Si\text{-}min}$, is 61 µm for the 2-5 Fractals, which is equal to the chamber width of the Grids. It should be emphasized that this is not meant to be an exhaustive comparison between the impact that ‘open’ and ‘closed’ electrode geometries have on neuron and glia network formation, but simply as a first test of the model of cell behavior proposed up to this point.

Beginning by focusing on some qualitative observations of cell behavior on the Grid and 2-5 Fractal geometries, Fig. 3-17 and Fig. 3-18 show representative fluorescence images of cell interactions with the electrodes. Glia were observed on both the SiO_2 and VACNT surfaces of both electrodes at 17 DIV. As expected from the previous results, the glia residing on the SiO_2 never extended processes over nearby VACNTs. In terms of morphology, the glia exhibited a spread-out shape typically featuring multiple long processes on the SiO_2 surfaces of both electrodes. In contrast, glia residing on the VACNT surfaces of both electrodes frequently adopted a more elongated morphology that was restricted by the shape of the underlying VACNT surface and although rare, even made 90° turns at the VACNT turning points.

Neurons adhered to and grew processes on both the SiO_2 and VACNT surfaces of the Grid and 2-5 Fractal electrodes. For both surfaces, neuron somas often clustered together and some of the processes connecting the clusters formed bundles (Fig. 3-17l and p). This behavior was observed more frequently on the SiO_2 surface than the VACNT surface. Neurons on the two surfaces were connected via clusters attached to the VACNT sidewalls and processes were frequently observed

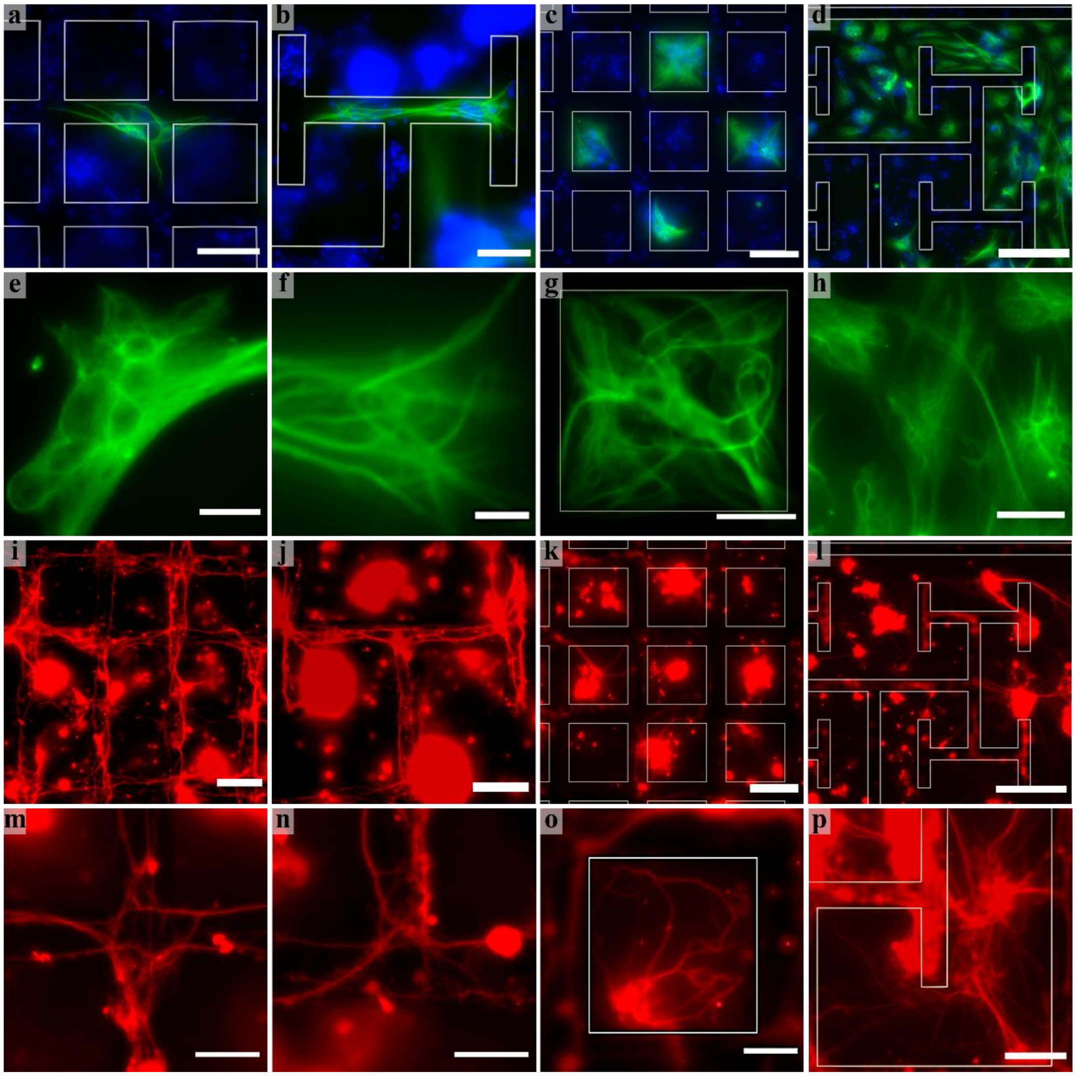

Figure 3-17. Representative examples of fluorescence images of retinal cells interacting with the Grid and 2-5 Fractal electrodes at 17 DIV. GFAP labelled glia (green) and DAPI labelled cell nuclei (blue) on the VACNT surfaces of the (**a**) Grid and (**b**) 2-5 Fractal electrodes. Glia accumulating on the SiO_2 surfaces of the (**c**) Grid and (**d**) 2-5 Fractal electrodes. The structure of glia on the VACNT surfaces of the (**e**) Grid and (**f**) 2-5 Fractal electrodes as well as the SiO_2 surfaces of the (**g**) Grid and (**h**) 2-5 Fractal electrodes. β-tubulin III labelled neurons (red) extending processes that follow the VACNT electrodes of the (**i**) Grid and (**j**) 2-5 Fractal electrodes. (**k**) Neuron clusters inside the chambers of a Grid electrode sending processes towards the VACNT sidewalls. (**l**) Large neuron clusters on the SiO_2 surface connecting to the neurons on the VACNT surface of a 2-5 Fractal electrode. Neuron processes following the VACNT electrodes of the (**m**) Grid and (**n**) 2-5 Fractal electrodes. (**o**) Neuron cluster attached to the VACNT sidewall of a chamber within a Grid electrode sending processes onto both the SiO_2 and VACNT surfaces. (**p**) Neuron clusters and connecting processes on the SiO_2 and VACNT surfaces of a 2-5 Fractal electrode. The images in (**c**) and (**k**) show the same FOV, as do (**d**) and (**l**). Electrode edges are highlighted with white lines except for panels (**i**), (**j**), (**m**), and (**n**) which concentrate on the behavior of processes along the edges because the lines would have obscured these processes. Scale bars are: 10 µm in (**e**) and (**f**); 20 µm in (**g**), (**h**), (**m**), (**n**), and (**o**); 40 µm in (**p**); 50 µm in (**a**), (**b**), (**c**), (**i**), (**j**), and (**k**); and 100 µm in (**d**) and (**l**).

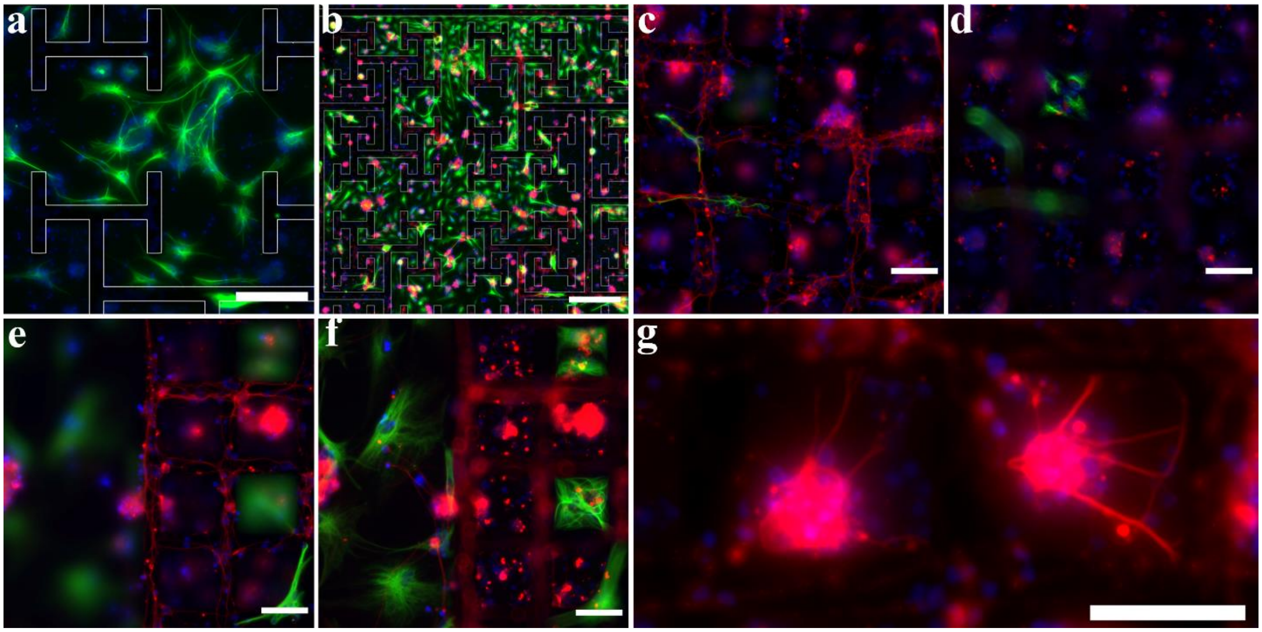

Figure 3-18. Additional examples of fluorescence images of retinal cells interacting with the Grid and 2-5 Fractal electrodes at 17 DIV. (**a**) GFAP labelled glia (green) and DAPI labeled cell nuclei (blue) inside the gaps of a 2-5 Fractal electrode. (**b**) β-tubulin III labelled neurons (red) as well as glia and cell nuclei within the gaps of a 2-5 Fractal electrode. The whole gap area is interconnected, giving the glia the potential to cover large surfaces. Neurons, glia, and cell nuclei accumulating on the (**c**) VACNT and (**d**) SiO_2 surfaces of a Grid electrode. Neurons, glia, and cell nuclei outside and within the patterned area of a Grid electrode with the focus being on the (**e**) VACNT and (**f**) SiO_2 surfaces. (**g**) Cell clusters sending neuron processes towards VACNT sidewalls in two side-by-side chambers of a Grid electrode. The images in (**c**) and (**d**) show the same FOV at two different focal planes, as do (**e**) and (**f**). Scale bars are 100 μm in (**a**), 200 μm in (**b**), and 50 μm in (**c**), (**d**), (**e**), (**f**), and (**g**).

following the top and bottom edges of the sidewalls (Fig. 3-17i and j). The large clusters on the SiO_2 surfaces were much more common for the 2-5 Fractal than the Grid electrodes, particularly in regions accompanied by large glial coverage. Large clusters were occasionally evident in some chambers of the Grid electrodes, and this most often occurred when glia were present. For example, in Fig. 3-17c and k the cluster in the central chamber (which has no glia) appears to be smaller than those in the surrounding four chambers (which are occupied by glia).

Moving on to quantitative measures, the effect of the SiO_2-VACNT material system on the glial and neuronal distributions on the two surfaces was studied through a statistical comparison of G_{Si} versus G_{CNT} and N_{Si} versus N_{CNT} for the Grid and 2-5 Fractal electrodes separately. There was no significant difference between G_{Si} and G_{CNT} for the grids (Fig. 3-19a), whereas G_{Si} was significantly higher for the 2-5 Fractals ($p \leq 0.001$, Fig. 3-19c). N_{Si} was significantly lower than N_{CNT} for both the Grids and 2-5 Fractals ($p \leq 0.01$, Fig. 3-19b, d).

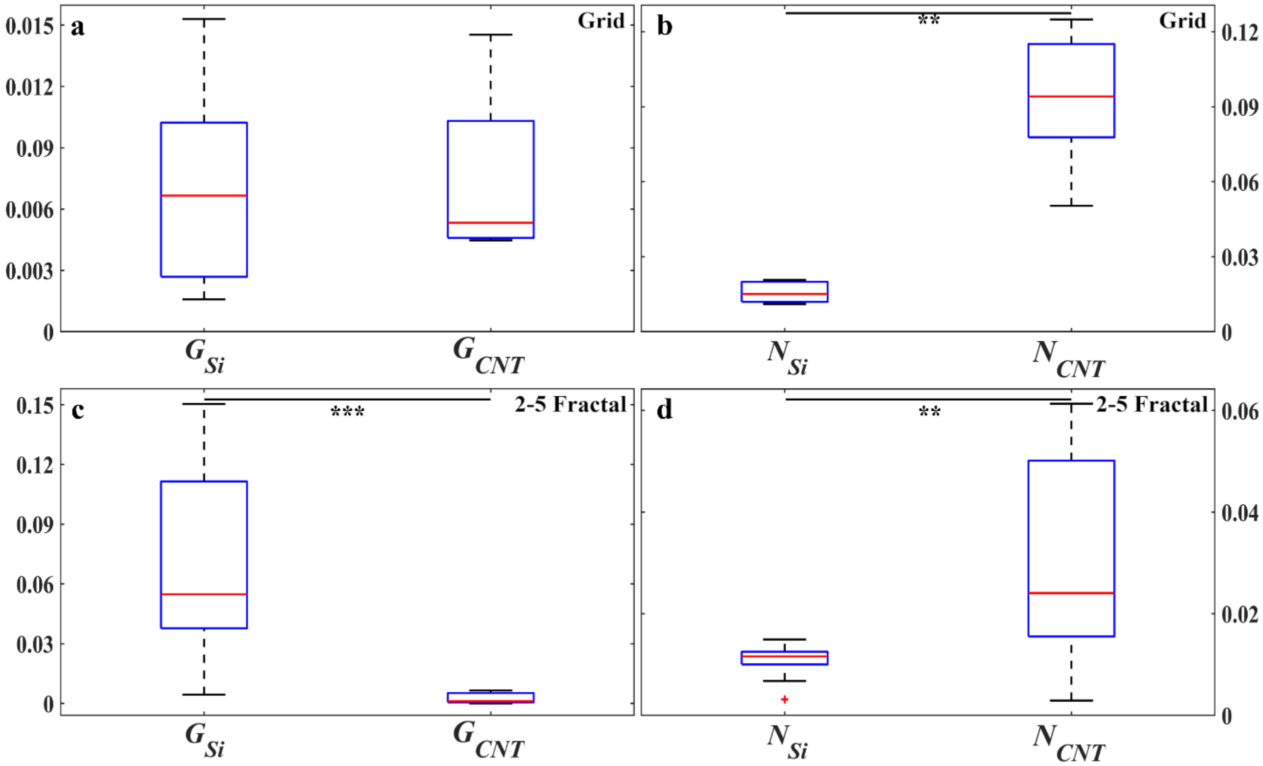

Figure 3-19. Comparison of glial and neuronal behavior on the SiO_2 and VACNT surfaces for the Grid and 2-5 Fractal electrodes at 17 DIV. Statistical analysis showing boxplots of G_{Si} (left) compared with G_{CNT} (right) for the (**a**) Grids and (**c**) 2-5 Fractals, as well as N_{Si} (left) compared with N_{CNT} (right) for the (**b**) Grids and (**d**) 2-5 Fractals. The y axes of (**a**) and (**c**) display the range of G_{Si} and G_{CNT} values and the y axes of (**b**) and (**d**) display the range of N_{Si} and N_{CNT} values. Stars in panels (**b**), (**c**), and (**d**) indicate the degrees of significance: *** and ** denote $p \leq 0.001$ and $p \leq 0.01$, respectively. The red plus in panel (**d**) is an outlier.

Having assessed the effect of the SiO_2 and VACNT regions on the glial and neuronal distributions for each electrode design separately, the success of the two electrodes in achieving the desired cell distributions (i.e. concentrating neurons and glia in the VACNT and SiO_2 regions, respectively) can now be compared. Figure 3-20a and b show scatterplots of G_{Si} versus G_{CNT} and N_{CNT} versus N_{Si} for the Grid and 2-5 Fractal electrodes. The black lines represent the conditions $G_{Si} = G_{CNT}$ and $N_{CNT} = N_{Si}$. All 2-5 Fractals successfully achieved the condition $G_{Si} > G_{CNT}$, while only 2 out of 7 Grids did so. On the other hand, all the Grids were successful in achieving the condition $N_{CNT} > N_{Si}$, whereas 9 out of 11 of the 2-5 Fractals were successful in doing so. The solid red and blue lines are fits through zero for the Grids and 2-5 Fractals and are included as guides to the eye. Although these linear guides are useful for comparing the data to the $G_{Si} = G_{CNT}$ and $N_{CNT} = N_{Si}$ conditions (represented by the slopes of the black lines), they are not meant to imply a strictly linear behavior.

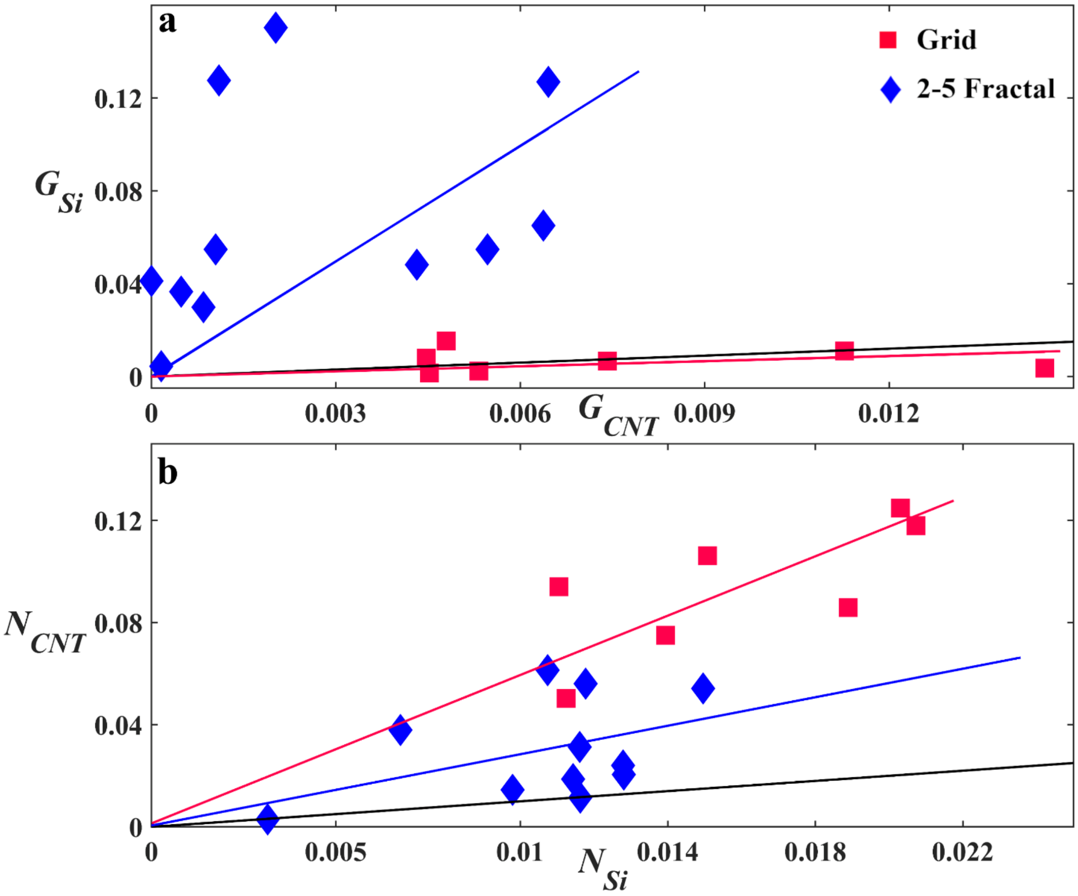

Figure 3-20. Study of the relationship of G_{Si} with G_{CNT} and N_{CNT} with N_{Si} for the Grid and 2-5 Fractal electrodes. (**a**) Scatterplot of G_{Si} versus G_{CNT} for the Grids (red) and 2-5 Fractals (blue). (**b**) Scatterplot of N_{CNT} versus N_{Si} for the Grids (red) and 2-5 Fractals (blue). The solid black lines represent the $G_{Si} = G_{CNT}$ and $N_{CNT} = N_{Si}$ conditions in (**a**) and (**b**), respectively. The solid red and blue lines are fits through zero for the Grids and 2-5 Fractals, respectively.

Finally, the Grid and 2-5 Fractal electrodes were compared directly for each of the four parameters (G_{Si}, G_{CNT}, N_{Si}, and N_{CNT}). In terms of glial behavior, results of statistical comparisons confirmed that the 2-5 Fractals had significantly higher G_{Si} than the Grids ($p \leq 0.01$, Fig. 3-21a), while the Grids had significantly higher G_{CNT} than the 2-5 Fractals ($p \leq 0.05$, Fig. 3-21b). Considering neuronal behavior, the Grids had significantly higher N_{Si} and N_{CNT} compared to the 2-5 Fractals ($p \leq 0.05$ and 0.01, respectively, Fig. 3-21c and d). The outlier in Fig. 3-19d and Fig. 3-21c has the lowest N_{Si} likely due to it having the lowest G_{Si} value among all 2-5 Fractals (this low G_{Si} was due to variations across different electrodes within a culture).

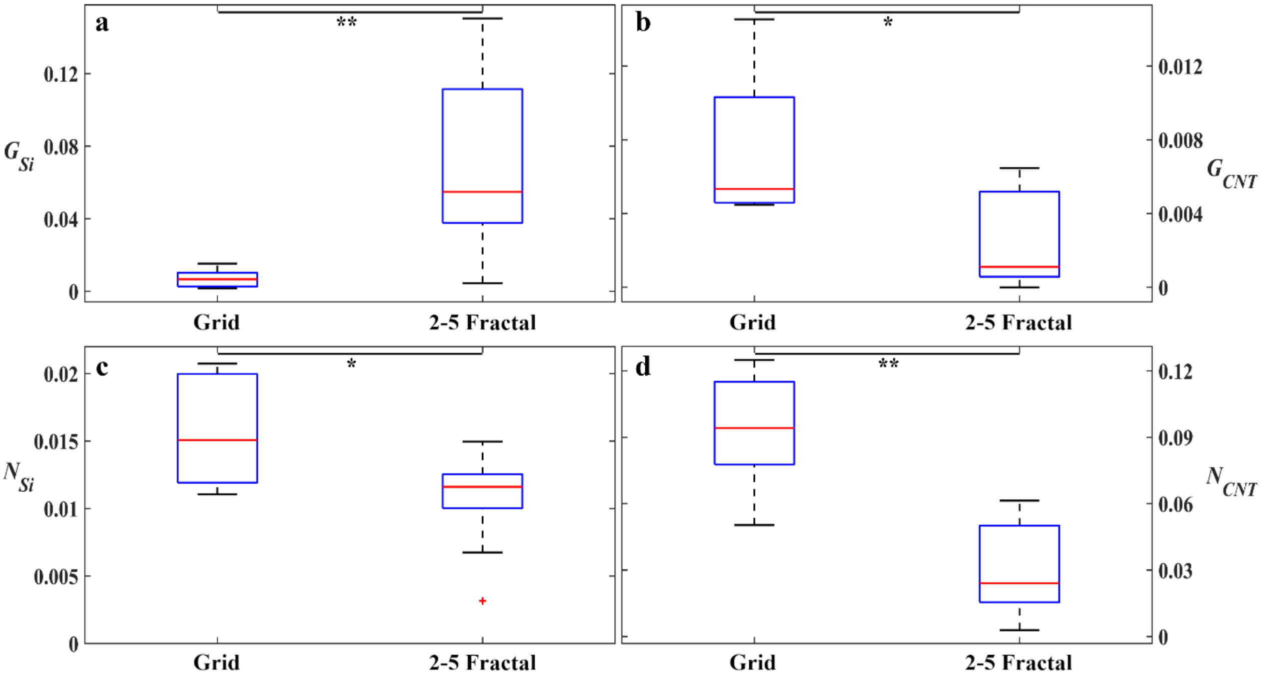

Figure 3-21. Comparison between the Grid and 2-5 Fractal electrodes at 17 DIV in terms of the glial and neuronal behavior on the SiO_2 and VACNT surfaces. Statistical analysis showing boxplots of (**a**) G_{Si}, (**b**) G_{CNT}, (**c**) N_{Si}, and (**d**) NCNT between the Grid and 2-5 Fractal electrodes. Stars in all panels indicate the degrees of significance: ** and * denote $p \leq 0.01$ and $p \leq 0.05$, respectively. The red plus in panel (**c**) is an outlier.

Discussion of Cell Behavior on Grid and 2-5 Fractal Electrode Geometries

As expected from the results seen earlier in this chapter, the smallest gap size, $W_{Si\text{-}min}$, in the 2-5 Fractal design was large enough to avoid restricting glial coverage from extending between the SiO_2 gaps, as suggested by the extended morphology of the glia located in/around the $W_{Si\text{-}min}$ gaps (Fig. 3-17d and Fig. 3-18a). Due to the smallest SiO_2 regions within the 2-5 Fractal electrode being connected to increasingly larger areas, the glia were provided with the freedom to expand their coverage across these large regions (Fig. 3-18b). Although the width of the Grid electrodes' chambers matched $W_{Si\text{-}min}$ for the 2-5 Fractal electrodes, the disconnected character of the Grid electrodes prevented glia that resided in one chamber from accessing other regions of the electrode (Fig. 3-17c). This left regions within the Grid electrodes devoid of glia and resulted in the Grids having significantly lower G_{Si} values than the 2-5 Fractal electrodes (Fig. 3-21a). Since it is well-known that glia act as the neurons' life support system[179,181] and their presence significantly improves synaptic connections between neurons[182], this may have significant negative effects on the survival and function of neurons in the long term.

Considering neuronal behavior on the SiO_2 surfaces, neurons rely on surface adhesion for their development and survival. Due to their closer proximity to the VACNT sidewalls, neurons in the chambers of the Grid electrodes had a higher chance of adhering to and growing their processes along the electrode edges than those in the larger gaps of the 2-5 Fractal electrode. This attraction of processes to the sidewalls rather than to the SiO_2 surface could have been further encouraged by chemical signals (neurotrophic factors)[170,183–185] from neurons and glia on the VACNT surface, potentially lowering N_{Si} for the Grids compared to the 2-5 Fractals. Additionally, the closer proximity to the VACNT sidewall also caused the behavior of the cells within the Grids' chambers to be dominated by the effects characteristic of the boundary regions discussed earlier in this chapter. In contrast, the behavior of the neurons in the gaps of the 2-5 Fractals would have been characterized by both boundary and cluster regions. The addition of the cluster regions to the gaps of 2-5 Fractals results in a higher tendency for aggregation of neurons into larger clusters and for bundling of their processes when compared to the Grids. This clustering behavior even left many locations in the gaps of the 2-5 Fractals completely empty of processes. It is therefore possible that the inclusion of cluster regions in the 2-5 Fractals could explain their significantly lower N_{Si} values compared to the Grids (Fig. 3-21c).

Consistent with previous results[129,136] and with the experiment comparing the Euclidean Rows and Fractal groups presented earlier in this chapter, the VACNT surface supported neuron process growth that was larger compared to the SiO_2 surface for both the Grid and 2-5 Fractal electrodes (Fig. 3-19b and d). CNT nano-roughness mimics some properties of the extracellular matrix (ECM), provides guided neuron process growth, and improves neuron adhesion[120,147]. In addition, they provide favorable mechanical flexibility that can improve neuron process growth and branching[186], so establishing a suitable environment for neuronal adhesion, survival, and growth without the need of any further chemical surface modification[136]. As was seen from the previous results comparing the Euclidean Rows and Fractal groups, these favorable CNT properties then resulted in the significantly larger N_{CNT} than N_{Si} values for both the Grid (Fig. 3-19b) and 2-5 Fractal electrodes (Fig. 3-19d). Due to their sensitivity to topographical cues[69,71,187,188], the processes exhibited a tendency to follow the top and bottom edges of VACNT sidewalls for both electrodes (Fig. 3-17i and j). The large, connected edge length of both electrode designs provided the opportunity for clusters to form and anchor to the VACNT sidewalls. The larger N_{CNT} values for the Grids when compared to the 2-5 Fractals (Fig. 3-21d) is likely explained by an increase in the prevalence of boundary regions which are characterized by clusters near or anchored to the Grid's VACNT sidewalls facilitating greater connections between the processes in the chambers and those on the VACNT surface (Fig. 3-17o and Fig. 3-18e-g).

Moving on to a discussion of the behavior of the glial cells, it is interesting to consider the result that G_{CNT} is higher for the Grids than the 2-5 Fractals. This is puzzling because the two electrodes have similar A_{CNT} values and the VACNT surface hinder cell division and growth. Based on these considerations, it is expected that G_{CNT} would be similar for the two electrodes. Although speculative, the Grids' neuron-rich VACNT surfaces might have shifted the fate of some of the existing retinal progenitor cells in the environment[189,190] towards becoming glia. It is known that, *in* *vivo*, neuronal stem/progenitor cells have the capability to differentiate into different neuronal cell types[191] depending on the physical, biochemical, and topographical cues present in their environment[192] and perhaps this effect extended to the *in vitro* environment[193,194] examined in this chapter. Accordingly, the larger N_{CNT} values for the Grids over the 2-5 Fractals (Fig. 3-21d) might have induced their larger G_{CNT} values (Fig. 3-21b). This relationship between neurons and glia on the Grids' VACNT surfaces is further suggested by Fig. 3-22, which provides a scatterplot of G_{CNT} versus N_{CNT}. The same overall trend of G_{CNT} increasing with N_{CNT} was also observed for the Euclidean Rows and Fractal groups. This relationship might also continue even after all the progenitor cells in culture have differentiated. As mentioned earlier when discussing a possible cause of the separation of the Fractal group into two regimes, having even a small number of glia on the surface of the VACNTs is likely associated with an increase in N_{CNT} because the glia provide chemical cues that promote process extension for the neurons residing on the VACNTs.

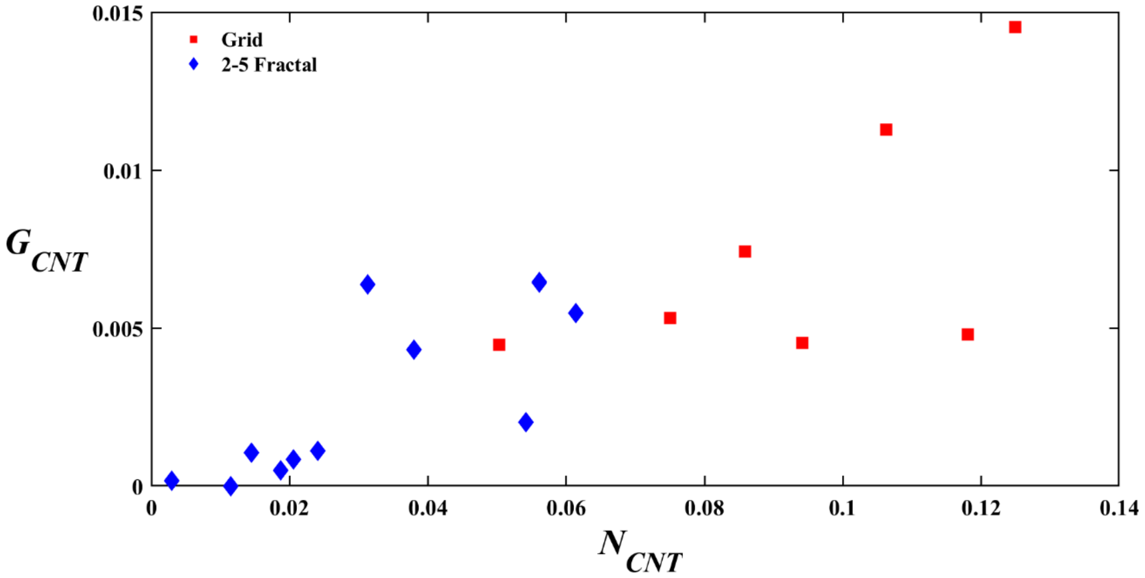

Figure 3-22. Study of the relationship of G_{CNT} with N_{CNT} for the Grid and 2-5 Fractal electrodes. Scatterplot of G_{CNT} versus N_{CNT} for the Grids (red) and 2-5 Fractals (blue).

Returning to Fig. 3-21a and b, the smaller values of G_{Si} and larger values of G_{CNT} for the Grids compared to 2-5 Fractals combine to generate the lack of significant difference between the two parameters in Fig. 3-19a. In contrast, the larger values of G_{Si} and smaller values of G_{CNT} in Fig. 3-21a and b lead to the significant difference for the 2-5 Fractals seen in Fig. 3-19c. Although N_{CNT} is significantly larger than N_{Si} for both the Grids and the 2-5 Fractals, the difference is larger for the Grids (Fig. 3-19b and d). These characteristics can also be seen in Fig. 3-20. The 2-5 Fractal data lie higher above the black line than the Grid data in Fig. 3-20a and the converse is true for Fig. 3-20b. The observed increase in N_{CNT} with N_{Si} in Fig. 3-20b is consistent with the previously proposed model describing the behavior of boundary regions.

In terms of the underlying aim of herding glia onto the SiO_2 surface and neurons onto the VACNT surface, the 2-5 Fractal electrodes performed better at the former and the Grid electrodes at the latter. However, the relative lack of nearby glia for the neurons on the Grids' VACNT surfaces is expected to have detrimental impacts on their survival and electrical activity in the long term. Although the Grid electrodes examined here had chambers on the scale of the individual glial cell bodies, it is informative to consider the impact of increasing the chamber size. If larger Grids were to be fabricated, some beneficial effects for glial surface coverage might be achieved. However, although larger chambers might offer an increased physical freedom for glial coverage due to their less-restricted geometry, there would be an accompanying reduction in proximity to the VACNTs. This would have multiple negative impacts. 1) Neurons and glia benefit from chemical cues[170,183] from each other and both cell types thrive when in close proximity. Implementing a larger chamber size will decrease this proximity between glia in the middle of the chambers and neurons on the VACNT surface. 2) The glia in the middle of the chambers will attract more neurons away from the VACNT sidewalls. This would increase the distance between neurons in the middle of the chamber and those anchored at the sidewalls (which mediate connections across the two surfaces), potentially reducing N_{CNT}. 3) For very large chamber sizes, cluster regions will likely become more prevalent and increase the probability of having gap areas devoid of cells, wasting space in the electrode design.

4) The reduced spatial density of VACNTs will provide less textured surface to support and stimulate the neurons.

Having established superior glial coverage in the gaps for the 2-5 Fractals, it is pertinent to discuss the amount of glia needed to keep neurons healthy and functional on the VACNT electrodes. Figure 3-23, which provides a plot of N_{CNT} versus G_{Si}, examines the correlation between the glia inside the SiO_2 gaps and neurons on the VACNT electrodes. Considering the 2-5 Fractals, N_{CNT} increases with G_{Si} with the shown linear fit described by an R^2 of 0.63. This fit is not meant to imply a strictly linear behavior, but instead to highlight the following key observations. Firstly, the data trend suggests that an absence of glia (i.e. $G_{Si} = 0$) impedes growth of neuron processes substantially. However, the data does not reveal a distinct lower limit (i.e. a G_{Si} value below which N_{CNT} falls to zero). This is backed up by qualitative observations showing that there are some VACNT regions that support processes even in the absence of nearby glia. Secondly, when variations in G_{Si} within the culture result in more glia, this increased presence promotes neuronal growth. Whereas it is possible that further increases in G_{Si} might eventually cause N_{CNT} to saturate or even show a depletion[195,196], the 17 DIV 2-5 Fractal system examined here operates within a regime in which there is no upper limit – the more glia the better. By comparing variations within the 2-5 Fractal electrode, neuron process growth can be taken as an indicator of health because all other geometric factors are constant. It should be stressed that this assumption cannot be extended to comparisons across the two electrode geometries. In particular, the higher N_{CNT} values achieved by the Grids compared to the 2-5 Fractals arises from the geometric factors discussed earlier (i.e. the sidewalls facilitating greater connections across the SiO_2 and VACNT regions) along with the Grid's larger G_{CNT} values. For completeness, a linear fit for the Grids is included, but note that the Grid's significantly lower G_{Si} values exclude meaningful observations regarding the relationship between N_{CNT} and G_{Si}.

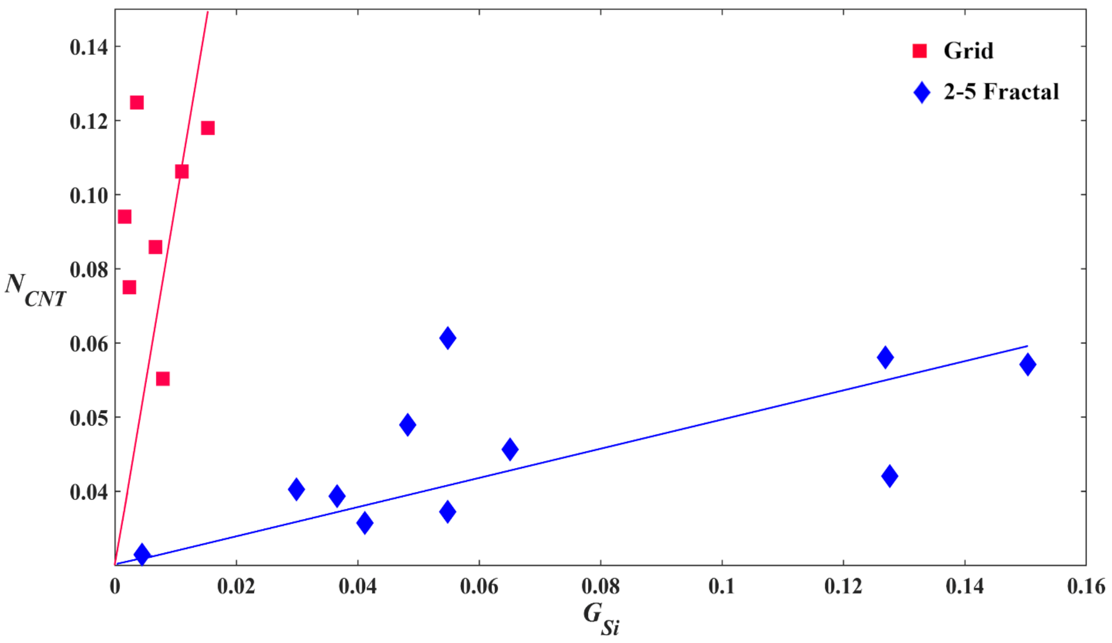

Figure 3-23. Study of the relationship of N_{CNT} with G_{Si} for the Grid and 2-5 Fractal electrodes. Scatterplot of N_{CNT} versus G_{Si} for the Grids (red) and 2-5 Fractals (blue). The solid red and blue lines are fits through zero for the Grids and 2-5 Fractals, respectively.

The above discussion focuses on the relative amounts of glia that are favorable for the VACNT-SiO_2 material system examined here rather than declaring absolute values for broader systems. Previous studies highlight that populations of cell types and consequently ratios of neurons to glia can vary widely between the strains of the same mammalian species[197] and across subregions of the same structure as a function of neuronal density[198]. With the current understanding of the neuron to glia ratio, it is challenging to determine a lower or upper limit for the number of glia needed in the gaps to guarantee the health and survival of the neurons on the VACNT electrodes. Previous studies claimed that a minimal glial occupation is necessary for protecting neurons from death but did not quantify the degree of occupation necessary[196]. It should also be acknowledged that the glial coverage and cell arrangements reported in the *in vitro* system examined in this chapter are vastly different to the glial coverage and cell distributions in a gliotic nervous tissue affected by neurodegenerative conditions[181,199] or insertion of an implant[199,200].

Finally, it is important to compare the current investigation of cell behavior on the Grid electrode geometry to previous studies in similar geometries. Various grid formations have been featured in glial investigations. A pioneering study in 1978 demonstrated that glial cells in 11 DIV cultures could be confined to square islands of palladium surrounded by a non-adhesive dried agarose film arranged in a grid pattern[201] in spite of negligible height differences between the palladium islands and surrounding agarose film. The VACNT electrodes examined in this chapter have much taller walls compared to the 1978 study. This emphasizes the enhanced restricting role of the electrode walls compared to the restrictive role of adherent and non-adherent surfaces. With regard to the size of a grid's chambers, studies have shown an increase in glial coverage as a function of increased surface area within a grid array using chamber sizes ranging from 75 to 200 µm[202]. For grid patterns defined by trenches[203], the largest trench spacing of 500 µm provided the highest glial coverage. These findings emphasize glial preference for geometries that provide greater physical freedom. For example, these trenches can be thought of as being equivalent to the SiO_2 gaps between the electrodes examined throughout this chapter and, accordingly, the glia accumulated within them. These findings were therefore consistent with the discussion provided here of physical freedom promoting glial coverage. Other studies investigated the interaction of neurons with grid patterns of negligible heights[140,204]. These showed that neurons followed the patterns and only deviated from them in longer cultures. The relatively large height of the VACNT electrodes examined in this chapter can potentially provide more robust confinement of neurons and their processes to the electrode surface for longer times. In another study, hippocampal neurons and glia were shown to colocalize on grid patterns with negligible heights in 26 DIV cultures[194]. The goal of this study was fundamentally different to the experiments presented in this chapter in which two cell types are guided into different regions of the electrode while keeping them in close proximity to each other. Whereas most of the previous studies discussed here focused on pure glial or neuron cultures, the current experiment has investigated a co-culture of neurons and glia to observe their behavior in more similar conditions to *in vivo* tissue. Additionally, although these previous studies examined cell behavior on a grid geometry, they also employed chemical approaches to guide cells to the desired areas within the grid. These chemical treatments may not be stable enough for long term *in vivo* applications and are fundamentally different to the electrode designs examined in this chapter in which their gaps offer the potential for cells to expand their coverage through growth and cell division.

CHAPTER IV

MODELLING NEURON BEHAVIOR AT THE SMALL SCALE

The work presented within this chapter has been adapted from previously published co-authored work by J. H. Smith, C. Rowland, B. Harland, S. Moslehi, R.D. Montgomery, K. Schobert, W. J. Watterson, J. Dalrymple-Alford, and R. P. Taylor in *How neurons exploit fractal geometry to optimize their network connectivity*, Scientific Reports **11**, 2332 (2021), by C. Rowland, B. Harland, J. H. Smith, S. Moslehi, J. Dalrymple-Alford, and R. P. Taylor in *Investigating Fractal Analysis as a Diagnostic Tool That Probes the Connectivity of Hippocampal Neurons*, Frontiers in Physiology **13**, 932598 (2022), and by C. Rowland, J. H. Smith, S. Moslehi, B. Harland, J. Dalrymple-Alford, and R. P. Taylor in *Neuron Arbor Geometry is Sensitive to the Limited-Range Fractal Properties of their Dendrites* Frontiers in Network Physiology **3**, 1072815 (2023).

This chapter begins by providing a summary of the experimental methods used to investigate the morphological properties of hippocampal pyramidal neurons from the CA1 region of the rat hippocampus. A technique for reconstructing and distorting three-dimensional models of the dendritic arbors of neurons is described as well as several metrics of morphological complexity that are used when analyzing the models. Methods for measuring various geometric parameters directly related to the functionality of the neurons are also explained. Following this, an analysis of the fractal properties of the neurons arbors and their constituent branches is provided using four different methods (two for the arbors and two for the branches). While there are various fractal analyses that can be applied to neurons, here the fractal dimension of a neuron’s branch is measured using a coastline analysis as well as a tortuosity scaling analysis, and the fractal dimension of a neuron’s arbor is measured using a box-counting analysis as well as a cumulative mass analysis (Table 4-1 provides a list of these fractal dimensions). Then, relationships between the fractal dimension of the neurons' arbors and their various functional parameters are charted. Using these relationships, an optimization model is employed that describes the functional benefits of the neurons' specific fractal geometry. It is found that the optimization model informs how the natural, fractal properties of the neurons are associated with an ability to balance its need to connect to other neurons while also building and operating an arbor and that deviations from the neurons natural state bring it away from an optimized condition.

Table 4-1. Summary of all measured fractal dimensions.

D_{BC}	coastline fractal dimension of a neuron's branch
D_{BT}	tortuosity fractal dimension of a neuron's branch
D_A	box-counting (or covering) fractal dimension of a neuron's arbor
D_M	mass fractal dimension of a neuron's arbor

Rodent Husbandry

Eighty PVGc male hooded rats were used (8–10 months old and weighing between 366 and 456 grams at surgery). The rats were maintained in reversed 12-h light schedule (8 a.m. to 8 p.m.) in their colony room so that all behavioral testing was conducted during the dark phase when activity levels are higher. Body weights were restricted to 85 to 90% of free-feeding weight during testing, with free food access for surgery, recovery, and during subsequent 40-day continuous enrichment period. All protocols detailed in this chapter conformed to the NIH Guide for the Care and Use of Laboratory Animals and were approved by the Animal Ethics Committee, University of Canterbury.

Image Acquisition, Model Reconstruction, and Model Distortion

The rats were given an overdose of sodium pentobarbital, their brains were removed fresh without perfusion, rinsed with Milli-Q water, and a 4mm block containing the hippocampus was cut in the coronal plane using a brain matrix (Ted Pella, Kitchener, Canada). These tissue blocks were processed with a metallic Golgi-Cox stain, which stains 1% to 5% of neurons so that their cell bodies and dendritic arbors can be visualized. 200 µm thick coronal brain sections spanning the bilateral dorsal hippocampus were taken using a microtome. A standard microscope was used to locate isolated neurons in the dorsal CA1 subfield (Fig. 4-1A). A Leica laser scanning confocal microscope was used to collect high-resolution image stacks (Fig. 4-1B) for these arbors. An example of one of the images within a stack is shown in Fig. 4-1C. The image stacks were captured using a 20x glycerol objective lens with a 0.7 numerical aperture, providing an x and y resolution of 0.4 µm. The step size (z distance between image stacks) was 2 µm.

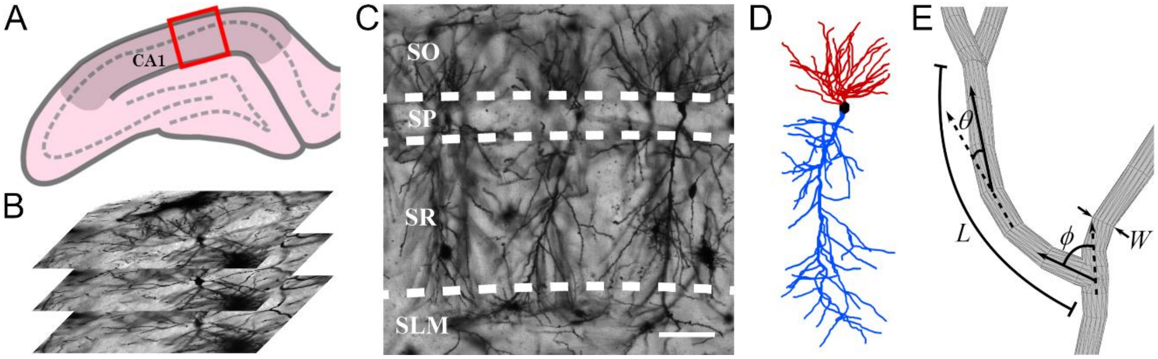

Figure 4-1. Demonstration of the neuron arbor reconstruction process. (**A**) Schematic diagram of a coronal slice through the rat hippocampus at Bregma -4.52mm showing the collection region (red box) within hippocampal CA1 (darkened area); the somata layer is denoted by the dashed line. (**B**) A stack of confocal micrographs of Golgi-Cox stained cells. Three 774 µm by 774 µm cross-sections separated by 2 µm in the z-direction are shown. (**C**) An example confocal micrograph (x-y layer) showing multiple neighboring dendritic arbors, each spanning the oriens (SO), pyramidale (SP), radiatum (SR), and lacunosum-moleculare (SLM) strata of the CA1 region. The dashed lines represent the strata boundaries, and the scale bar corresponds to 100 µm. (**D**) A three-dimensional model of a neuron's dendritic arbor, reconstructed from a z-stack of confocal micrographs, featuring the apical (blue) and basal (red) arbors and the soma (black). (**E**) Schematic providing an example measurement of a weave angle, θ, forking angle, ϕ, forking length, L, and width, W, for a neuron's dendrites.

Arbors were manually traced through the image stacks using Neurolucida (MBF Bioscience, Williston, VT, USA)[205] to create three-dimensional models (Fig. 4-1D). The models were then exported to the Wavefront .obj format and their soma removed, leaving only the arbor's dendrites. In this format, the arbor reconstructions were defined by sets of connected, cylindrical segments. The median length and width, W, of the segments were 2.4 µm and 1.4 µm, respectively. Each cylinder was constructed using two sets of rings of 16 points (vertices) and 32 connecting triangles (faces). At a dendrite's terminal point, the final segment had 14 faces that formed an end cap. Bifurcating dendrites started new segments at the same location as the last set of 16 vertices from the parent dendrite. The forking length, L, between two bifurcations along a dendritic branch had a median value of 42 µm. Note that L also includes lengths between a branch's forking point and its terminal point, as well as between a forking point and the point connected to the neuron's soma. For the apical arbors, one primary dendrite extended from the apex of the soma and all other apical dendrites were either directly or indirectly connected to this primary dendrite. For the basal arbors, multiple primary dendrites extended from the soma.

In order to perform the box-counting and profile analyses (explained below), the Wavefront files were used to create voxelized versions of the neuron arbors. The voxelization was performed at a resolution of 4 voxels/µm for box-counting and 1 voxel/µm for the profile calculation. In both cases, the arbor models were voxelized "exactly," meaning that if any part of the polygonal Wavefront model fell inside a voxel, the three-dimensional coordinate of that voxel was included in the voxelized representation of the arbor.

Distorted versions of the neuron arbors were created using rotation quaternions[206] by multiplying the weave angles, θ, and forking angles, ϕ, of the arbor's dendritic branches by a common factor α, called the angle multiplier. The weave angles were defined as the angles between connecting segments along a branch and had a median value of 12°. The forking angles were defined as the first weave angle following a bifurcation point on a branch and had a median value of 37°. Figure 4-1E shows example measurements of θ and ϕ. When distorting θ, those angles furthest from the soma were rotated first and, working inwards, each subsequent angle was then rotated one at a time until all of the angles had acquired their new values. When an angle was rotated, the entire connected section of the branch between that angle and the terminal endcaps was also rotated. This rotation occurred in the plane of the two vectors that define that angle. The range of α values used (0.5 to 2 in steps of 0.25) was chosen to ensure that separate branches rarely intersected, so ensuring a physically reasonable condition.

The effect that α had on the distributions of θ and ϕ can be seen in Fig. 4-2. Because our investigation focused on the weaving and forking deviations of connected segments relative to the dashed lines shown in Fig. 4-1E, their measured angles did not distinguish between whether the segments fell to the left or right of these lines. Accordingly, for the rare examples when the value of θ or ϕ was greater than 180° (corresponding to segments crossing over the dashed line) after distortion, it was adjusted to ensure that it remained within the range of 0° to 180°. For example, when $\alpha = 2$ was applied to a natural (i.e. undistorted) ϕ value of 100°, the resulting distorted ϕ was measured as 160° rather than 200°. This measurement scheme caused the slight non-linearity seen at large α values for the red and blue curves of Fig. 4-2d. The percentages of θ values crossing the dashed line after distortion were 0.009% and 0.07% for $\alpha = 1.5$ and 2, respectively. The corresponding percentages for the ϕ values were 0.7% and 2.7%. Note that if the weave and forking angles were not distinguished between and had instead been treated as one set of angles, the combined distribution would follow a similar behavior to that shown in Fig. 4-2a and b due to the relatively small number of forking angles.

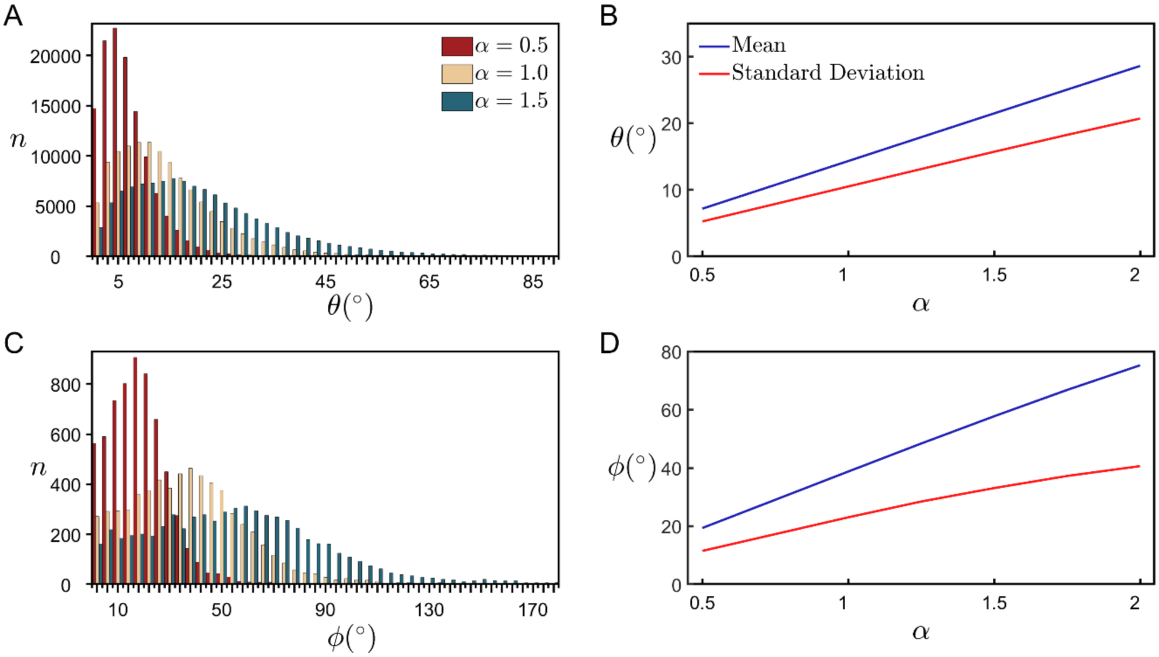

Figure 4-2. Study of the impact of the angle multiplier on the weave and forking angles. Histograms of the number, *n*, of occurrences of (**A**) θ and (**C**) ϕ values across all basal arbors. The impact of modifying these angles is shown for three α values. (**B**, **D**) Changes to the mean and standard deviation of the distribution of these angles as a function of α.

Calculating the Coastline Fractal Dimension of a Neuron's Branch

Within this chapter, a dendritic branch is defined as any path that starts from the soma and ends at the tip of a dendrite (Fig. 4-3B). Note that within this definition, different branches commonly have shared sections (Fig. 4-3C). To calculate a branch's coastline fractal dimension, D_{BC}, a three-dimensional extension of the traditional method pioneered by Richardson[207] and then Mandelbrot[25] in their discovery of the fractal character of meandering coastlines has been used. The 'coastline method' examines a branch at different resolutions through its employment of a ruler of length, L_R. Shown in Fig. 4-4A, the branch is segmented into a series of rulers. The branch's fractal scale invariance can then be revealed through the following power-law relationship between L_R and the number of rulers needed to span the branch's entire length, N_R:

$$N_R \propto {L_R}^{-D_{BC}} \qquad \text{(Eq. 4-1)}$$

D_{BC} can be extracted from a log-log plot of N_R versus L_R. In this analysis, L_R was normalized to the largest possible ruler length connecting the soma to the branch endpoint, L_E.

This fractal scaling was limited at fine scales by the finite sizes of the branches, which set a fine scale 'cut-off'. Rulers smaller than 4 µm (which approaches 2.5 µm, the median value of the branch segment length) were not considered because smaller rulers would start to detect the linear character of the cylindrical segments rather than the fractal character of the meandering branches. At the course scale, rulers spanning up to 40 µm were allowed, which provides an order of magnitude scaling on the log-log plots used to extract D_{BC}. This 'one-order' rule was applied to all branch sizes to standardize the fitting procedure that generated their D_{BC} values and was chosen in order to maximize the number of branches used in the comparison of the two examined methods for measuring branch fractal dimension (the second being tortuosity fractal dimension). Selecting this one-order range excluded only 35 of the 3354 total undistorted branches, compared to, for example, 1930 branches if 1.5 orders was used as the scaling range.

Figure 4-4A provides a graphical representation of how the segmented versions of a branch were generated. Initially, a spherical shell of radius L_R was centered on the branch end connected to the soma. The start point of the first segment was set at this location and the end point was set where the branch intersects the spherical shell. If the spherical shell intersected the branch at multiple locations, then the location which had the shortest path

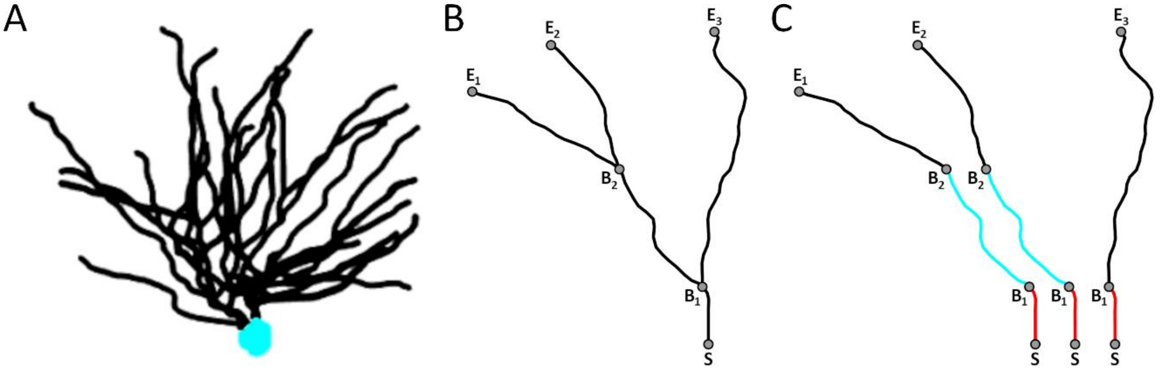

Figure 4-3. Schematic illustrating the paths taken by dendritic branches. (**A**) An example reconstruction of a neuron's basal arbor with the neuron's soma colored in cyan and its dendrites in black. (**B**) An example of the paths taken by a neuron's dendrites. S denotes the point where the dendrites initially extend out of the soma. B_1 and B_2 denote the points at which the dendrites bifurcate. E_1, E_2, and E_3 denote the endpoints of the dendrites. (**C**) The three dendritic branches seen in (**B**) separated from one another. The red and cyan colors are used to indicate sections that are shared between branches.

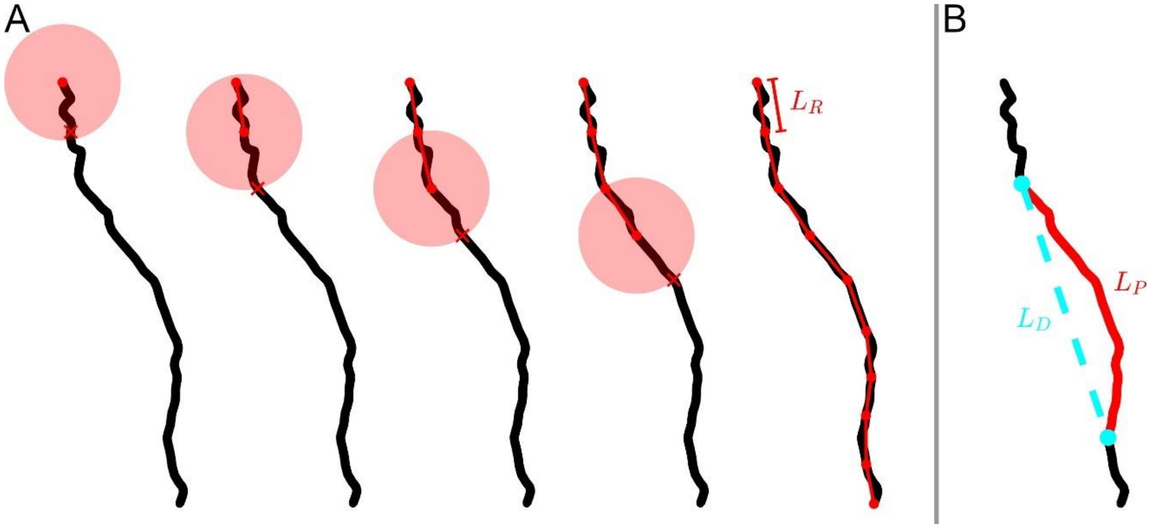

Figure 4-4. Examples of the measurements needed to implement the coastline and tortuosity fractal analyses. (**A**) Schematic demonstrating the placement of rulers along the branch of a neuron. The black curve shows an example neuron branch, the connected red dots show the segmented version of a branch at a given ruler length, L_R, the transparent red circles represent the spherical shells used to determine where to place each segment, and each red X indicates where the branch intersects the spherical shell, each of which has a radius equal to L_R. After the branch has been fully segmented (**A**-right), the number of rulers used to span the branch, N, can then be counted for multiple ruler lengths. (**B**) The same branch shown in (**A**) with a chosen branch section of path length, L_P, highlighted in red and the Euclidean distance, L_D, separating the ends of this section shown by the dashed cyan line. The tortuosity, T, of paths can then be measured across paths of varying length.

length along the branch from the intersection to the center of the spherical shell was chosen. The next segment was defined using the same process, but the spherical shell was instead centered at the end point of the previous segment. However, once the first segment was placed, parts of the branch that had already been segmented but which intersected the shell were not considered when placing a new segment. This ensured that in general each new segment was placed closer to the branch terminal point than the previous segment. This process was repeated until the spherical shell no longer intersected the branch. If part of the branch remained unaccounted for, then a truncated segment was inserted to connect the endpoint of the previous segment to the branch's terminal point. For cases when a truncated segment existed at the terminal point, the truncated segment was counted as a fraction of a segment. For example, for a ruler length of 10 µm, if the segmented version of the branch was comprised of 12 full segments and a truncated segment of length 2 µm then N_R was counted as 12.2.

The above analysis was performed on both the undistorted and distorted neuron branches. For the undistorted neurons, a method for calculating the normalized coastline fractal dimension, D_{BCN}, of all the branches within a given neuron was employed. Normalizing L_R to the Euclidean distance separating the ends of a branch, L_E, allowed for a direct comparison of N across branches with different lengths. D_{BCN} was calculated by plotting all of the branches on a single log-log graph of N versus L_R/L_E and extracting the magnitude of the slope of the combined data. In order to avoid having some branches dominate the fine and coarse scales of the fit, only the range of L_R/L_E over which all of the neuron's branches contributed was used in the fitting procedure. It should be stressed that this normalization procedure was used only to demonstrate the similar fractal character of different-sized branches.

Derivation of Tortuosity Fractal Dimension

The fractal dimension of a selected section of a neuron's branch, D_B, can be quantified using the power-law dependence of the number of rulers, N_R, spanning the branch section and the ruler length, L_R, being used, where L_R can be normalized to the largest ruler length spanning the chosen section, L_D.

$$N_R \propto \left(\frac{L_R}{L_D}\right)^{-D_B} \qquad \text{(Eq. 4-2)}$$

In the coastline method described in the previous section, D_B is labelled as D_{BC}, the full branch length is considered (i.e. $L_D = L_E$) instead of a section of a branch, and N_R is measured as L_R is reduced.

For the tortuosity method, D_B is labelled as D_{BT} and ruler count variations are converted to length variations by substituting $N_R = L_T/L_R$ into Eq. 4-2, where L_T is the total length of all the rulers, yielding

$$L_T \propto {L_R}^{-(D_{BT}-1)}{L_D}^{D_{BT}}. \qquad \text{(Eq. 4-3)}$$

Whereas the coastline method sets the second term of Eq. 4-3 constant and investigates the dependence on L_R, the tortuosity method sets the first term constant by considering a ruler length set at the finest possible resolution, causing L_T to approach the total length of the chosen branch section, L_P, and investigates the changes in L_P as L_D is reduced. Substituting L_T for L_P and keeping L_R constant in Eq. 4-3 then generates the following relationship:

$$L_P \propto {L_D}^{D_{BT}}. \qquad \text{(Eq. 4-4)}$$

The definition of tortuosity used here is the ratio of a path's curvilinear length, L_P, to the Euclidean distance between the two endpoints of that path, L_D (which is equivalent to the largest ruler length spanning the branch section), where a path is defined as any section of a neuron's branch connecting two points on that branch.

$$T = \frac{L_P}{L_D} \qquad \text{(Eq. 4-5)}$$

Substituting Eq. 4-4 into Eq. 4-5 then gives

$$T \propto L_P^{\frac{D_{BT}-1}{D_{BT}}}. \qquad \text{(Eq. 4-6)}$$

Labelling the exponent of Eq. 4-6 as S and solving for D_{BT} yields

$$D_{BT} = \frac{1}{1-S}. \qquad \text{(Eq. 4-7)}$$

Calculating the Tortuosity and Tortuosity Fractal Dimension of a Neuron's Branch

Before calculating the tortuosity fractal dimension, D_{BT}, of a branch, it must first be sectioned into all of the possible paths along that branch. An example path and its associated L_P and L_D lengths are shown in Fig. 4-4B. L_P was calculated by summing the lengths of all of the cylindrical segments spanning the chosen section of the branch. L_P can in principle be used to measure the length of any branch section - from the smallest sections approaching the segment length through to the largest possible section approaching the length of an entire branch. In each case, L_P captures the fractal tortuosity (i.e. meandering) of a branch. In contrast, L_D represents the length of the straight, Euclidean line connecting the two ends of a chosen section along the branch. T was measured across all possible paths along a branch and plotted against L_P on a log-log plot. The D_{BT} value of that branch can then be extracted using the slope of this log-log plot and substituting it into Eq. 4-7.

Due to the large noise inherent in plots of T versus L_P, it was first divided into bins over the desired scaling range (4 µm to 40 µm was chosen in order to match the range examined in the coastline fractal analysis) before fitting the data to extract D_{BT}. The average

T value was then calculated for each bin and the binned data was fitted on a log-log plot, yielding D_{BT} for the chosen branch. A single D_{BT} value was also calculated for all of the branches across all neurons. This procedure was the same as that for calculating D_{BT} for an individual branch except that the data from all the paths within all of the branches across all neurons was combined onto a single plot of T versus L_P. Note that duplicate paths exist due to different branches having overlapping sections (Fig. 4-3C) and therefore any duplicated data has been removed before performing the fit.

Calculating the Arbor Radius of a Neuron

The arbor radius, R_A, of a neuron can be defined as its radius of gyration and can be measured as the root mean square distance between any two points on the arbor[94]. However, for reconstructions of arbors in which the lengths of the dendritic segments (i.e. the cylinders) comprising the arbor are not uniform, R_A can also be calculated as

$$R_A{}^2 = \frac{1}{L_A{}^2} \sum_{i=1}^{K} \sum_{j=1}^{K} \delta l_i \delta l_j \left(r_i - r_j\right)^2 \qquad \text{(Eq. 4-8)}$$

where L_A is the total length of all the dendrites within the arbor, δl_i is the length of dendritic segment i, r_i is the position vector of dendritic segment i, and K is the total number of dendritic segments[208].

Modified Sholl Analysis

Traditionally, Sholl analyses of neurons are performed by counting the number of intersections of the neuron's arbor with concentric rings (in two dimensions) or spheres (in three dimensions) of increasing radii centered at the neuron's soma. In parts of this chapter, a modified version of a traditional three-dimensional Sholl analysis is employed that calculates the number of intersections, N_I, of a neuron's arbor with concentric spheres of increasing radii, r, averaged across spheres centered at 25 randomly selected locations on a neuron's arbor within a distance of $R_A/\sqrt{2}$ of the center of mass of the arbor[208]. This sampling of many local origins rather than just one origin centered on the soma accommodates potential variations arising from some parts of the neurons possessing different structural qualities than others. Restricting the selection of local origins to be within $R_A/\sqrt{2}$ of the center of mass of the arbor reduces the number of spheres that have large portions extending beyond the arbor's periphery. This approach also allows alignment with the cumulative mass fractal analysis (detailed below) which similarly samples many locations[94].

Calculating the Covering Fractal Dimension of a Neuron's Arbor

A three-dimensional, modified, 'sliding' box-counting analysis[89] was used to calculate the box-counting fractal dimension of the neurons' arbors, D_A, sometimes referred to as the 'covering' fractal dimension. The voxelized dendritic arbor was embedded into a three-dimensional array of boxes and the number of boxes, N_{box}, occupied by the arbor was counted across a range of box sizes, L_{box}. The minimum box count was selected after sliding the embedded array of boxes in every coordinate direction simultaneously in 0.25 µm steps. Figure 4-5 shows examples of the boxes occupied by a neuron across various box sizes. If a neuron's arbor displays fractal scale invariance, then the following power-law relationship holds between N_{box} and L_{box}:

$$N_{box} \propto {L_{box}}^{-D_A} \qquad \text{(Eq. 4-9)}$$

Given that an arbor has a limited physical size and that the reconstructions examined here are created with a limited resolution, this fractal scaling will only hold over a finite range. At the fine size scale, L_{box} was limited to be greater than 2 µm as the median length and width of the dendritic segments comprising the reconstructed models are 2.6 µm and 1.4 µm, respectively. This helps avoid resolution effects arising from the segment shapes. At the coarse scale, L_{box} was limited to be less than one fifth of the largest extent of the arbor in the x, y, or z-directions to ensure sufficient counting statistics. Within these limits, a straight line was fitted for all sets of points that range over at least an order of magnitude on the log-log plot of N_{box} versus L_{box} and the fit with maximal R^2 was chosen to measure D_A.

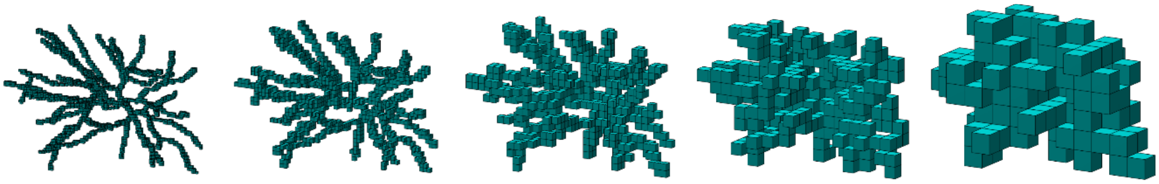

Figure 4-5. Visualization of the space occupied by a neuron's arbor across multiple size scales. From left to right, each image shows the boxes occupied by a neuron's basal arbor with increasing box size as determined by the box-counting analysis.

Calculating the Mass Fractal Dimension of a Neuron's Arbor

To perform a cumulative mass fractal analysis (also referred to as the mass-radius method) of a neuron's arbor, L_{in}, the total length of all dendrites within concentric spheres of increasing radii, r, was calculated and averaged across randomly selected sphere centers using the same process as the modified Sholl analysis. The range of r examined is also the same as that used in the modified Sholl analysis. For a neuron with fractal branches, the mass fractal dimension, D_M, of its arbor can be measured from this cumulative mass analysis using the following relationship[94,209]:

$$L_{in} \sim r^{D_M} \qquad \text{(Eq. 4-10)}$$

D_M is referred to as the mass fractal dimension because it measures the change in cumulated mass of the object as a function of the size of the region considered (relating length to mass assumes that the branch width does not vary substantially, which is a reasonable approximation for the cylindrical segments comprising the neuron reconstructions used in this chapter). Thus, the slope of a log-log plot of L_{in} versus r provides a quantitative value of D_M. However, once the radius of a sphere reaches a large enough value that the entire arbor is contained within the sphere, L_{in} will become equal to L_T. As such, this power-law scaling only holds over a finite range of r. The scaling range of the fit used to calculate D_M was chosen to be consistent with the scaling range examined when calculating D_A using the box-counting method.

Calculating the Surface Area, Bounding Area, Bounding Volume, and Profile Area of a Neuron's Arbor

In order to quantify the potential for a neuron's dendrites to connect to other neurons as well as the costs associated with building and operating those dendrites, the following metrics were utilized: surface area (A_s), bounding area (A_b), bounding volume (V_b), and profile area (P). To measure A_s, the surface area of a neuron's arbor was calculated by summing the area of all the triangular faces defining the cylindrical segments of the arbor's dendrites. However, due to some faces being partially positioned inside the branches of an arbor, a technique was employed that measures A_s more precisely by increasing the resolution of the triangular faces and then removing those faces with all three corners inside a branch. To measure A_b and V_b, the bounding area and volume of the arbor, respectively, were calculated using the convex hull method[210]. An example of the convex hull of a neuron's arbor is provided in Fig. 4-6.

Calculating P required a more involved process than A_s, A_b, and V_b that made use of the voxelized version of a neuron's arbor. As the arbor reconstructions used here did not include an arbor's dendritic spines, the potential contribution of the dendritic spines to an arbor's profile were accounted for in the calculation of P by uniformly expanding the voxelized arbor by 2 μm in every direction. The orange region around the black dendrites seen in Fig. 4-7 represents the space around the dendrites in which a spine could grow in order to form a synapse with an axon passing through the arbor. While including a solid orange region assumes a high spine density, lower densities could be accommodated by reducing the profile by a density pre-factor. Given that the comparisons in this chapter are made across the same neuron type with the same spine density, the value of the pre-factor will not impact the results.

The voxelized and expanded arbor was then orthographically projected onto the x-y plane. After projection, the points were rounded and any duplicate points occupying the same location were removed. Because the location of the points has been rounded, each point represents a 1 μm^2 area and the total area occupied by this projection can be measured by counting the number of remaining points constituting the projection. The area of this projection divided by the bounding area of the neuron is then proportional to the probability of connection with an axon travelling parallel to the z-direction and passing through the dendritic arbor. However, because the axons that pass through the arbors of our CA1 neurons can arrive from any direction[76,211], the average profile of each neuron's arbor was calculated as though it were viewed from any point on the surface of a sphere containing the neuron's arbor with its origin at the neuron's center of mass. To accomplish this, a set of polar and azimuthal angles were defined that corresponded to uniformly distributed viewpoints on the sphere. Rotating the voxelized and expanded arbor by these angles and then projecting the result onto the x-y plane yields what the arbor would look like if seen from the given viewpoint. *P* was then calculated by averaging the area of the projections corresponding with each of our uniformly distributed viewpoints. Because it is impossible to distribute a general

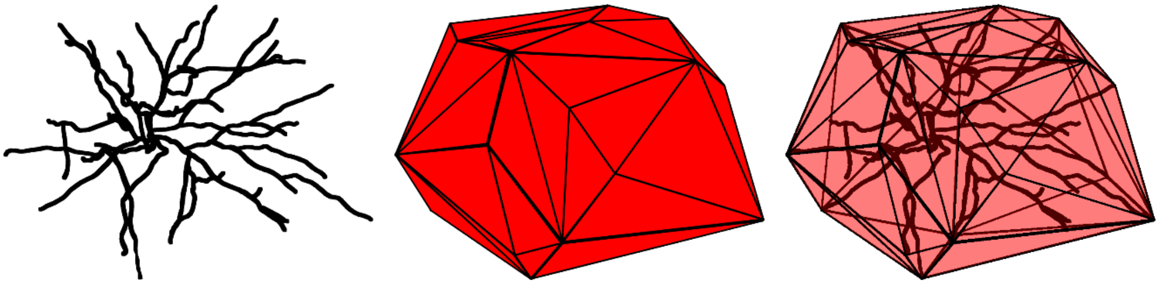

Figure 4-6. Visualization of the convex hull of a neuron's arbor. A neuron's basal arbor (left) and its convex hull (middle) are shown. Overlapping them (right) and making the faces of the convex hull transparent demonstrates how the convex hull encapsulates the arbor.

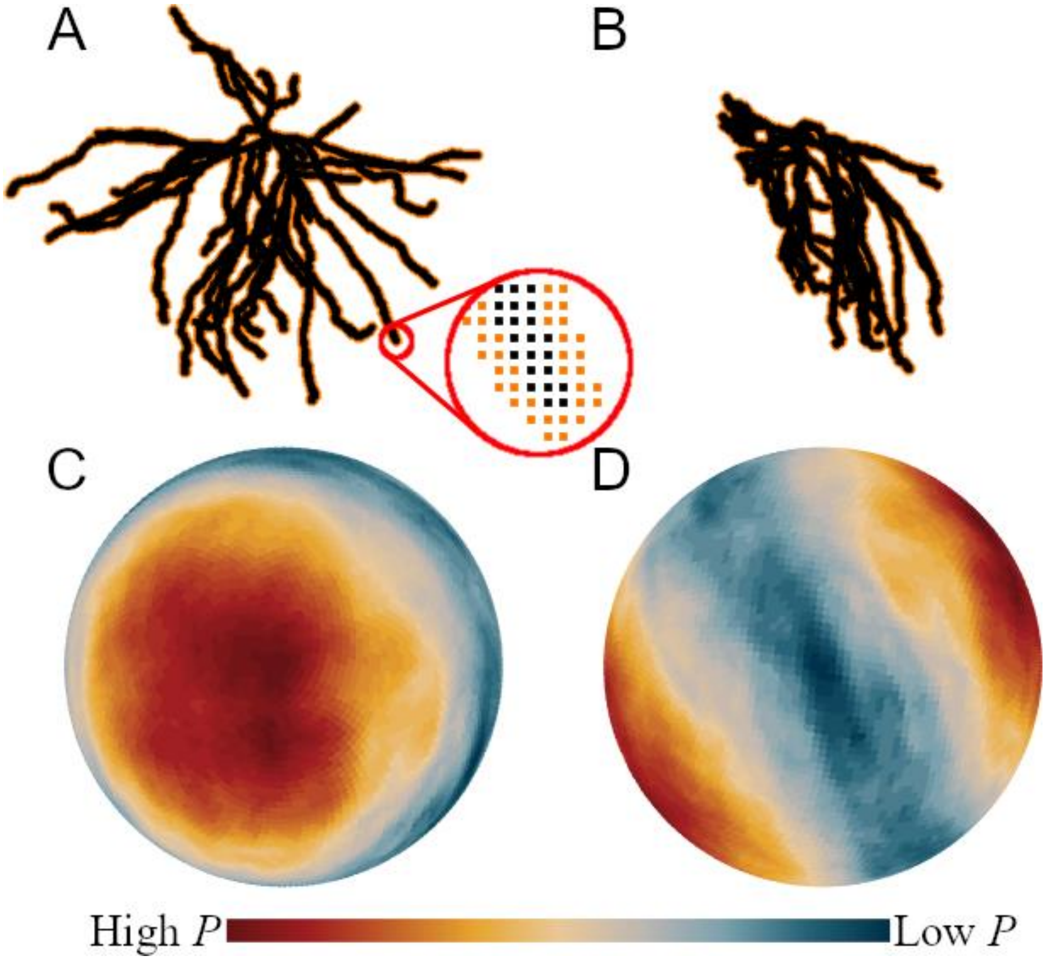

Figure 4-7. Measurement and mapping of the profile area of a neuron's arbor. (**A**) A neuron's basal arbor viewed from the direction for which *P* peaks. The zoom-in shows a black dendrite surrounded by an orange region representing the zone in which spines may extend. (**B**) The same arbor viewed from a different direction. (**C**) and (**D**) show the equivalent profile spheres. The middle point on the sphere's surface shown in (**C**) and (**D**) corresponds to the profile of the arbor as seen from the viewpoints shown in (**A**) and (**B**), respectively.

number of perfectly equidistant points on the surface of a sphere[212], the set of points was defined using the Fibonacci lattice, a commonly used and computationally efficient method for uniformly distributing the points[213].

The colored spheres in Fig. 4-7 (comprised of 10001 points) give a visual representation of the variation in profile with respect to the viewpoint. The P values used in this chapter, however, were calculated using only 201 viewpoints, which is sufficient for convergence - P for 201 viewpoints deviates by less than 1% from the value achieved when approaching infinite viewpoints.

H-Tree Generation

The neurons examined in this chapter have had several of their properties compared to H-Trees to identify the similarities and differences to a traditional mathematical fractal pattern in which its fractal dimension, D, can be set by scaling the lengths, L, of the H-Tree's branches (it should be emphasized that any similarities do not imply a shared growth mechanism[214]). Figure 4-8 shows examples of the H-Tree models used in the comparisons. Whereas these H-Trees extended into three-dimensional space (middle and bottom row), two-dimensional H-Trees have also been included (top row) for visual comparison. The D values of these H-Trees were determined using the length scaling relationship:

$$L_i = \frac{L_1}{2^{\frac{i-1}{D}}} \qquad \text{(Eq. 4-11)}$$

where L_i is the branch length of the ith iteration. The length of the first iteration, L_1, of any given H-Tree was chosen such that the total length of all its branches was constant across all D values. The number of iterations in the H-Trees was set to 12 to be close to the largest number of branch levels observed for the basal arbors (which was 11) and the width of the

H-Tree's branches was chosen to be 1 μm, which is similar to the 1.4 μm median width of the branches for the basal arbors. Whereas the theoretical *D* value of the straight H-Tree models is set by the scaling of its branch lengths, incorporating a statistical weave into the paths taken by the branches (bottom row of Fig. 4-8) causes the 'true' *D* value of the H-Tree to deviate from the theoretical *D* value associated with the scaling of its branches. For consistency when comparing the H-Trees and neurons, the 'true' *D* value of the H-Trees will be labelled as D_A and measured using the same box-counting method applied to the neurons.

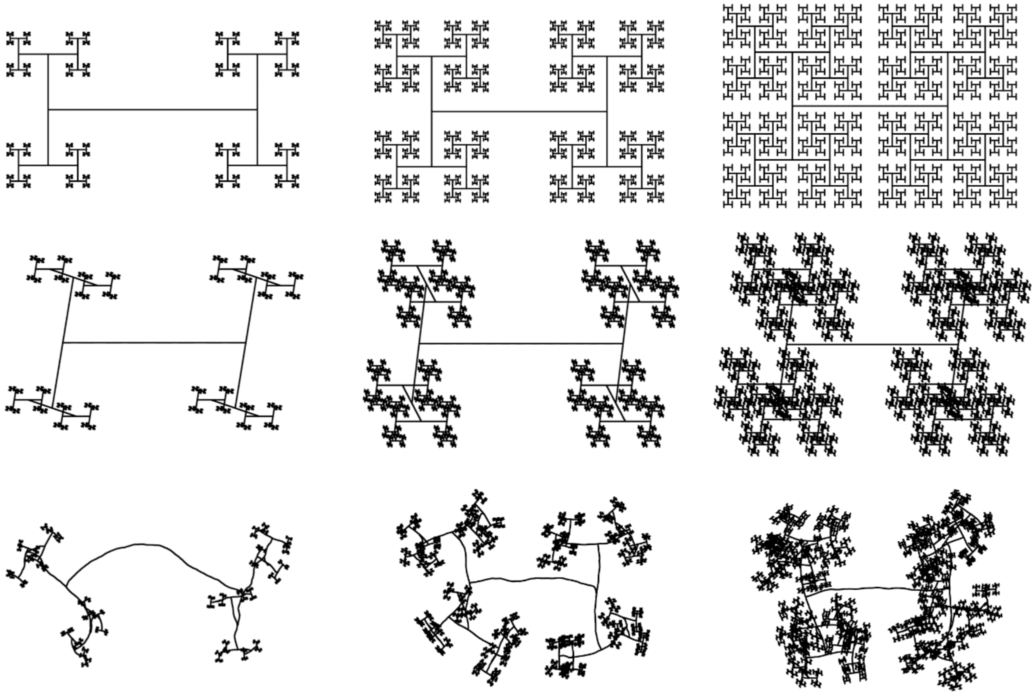

Figure 4-8. Example H-Tree models in two and three dimensions. A visual comparison of H-Tree models extending into two-dimensional (top row) and three-dimensional (middle row) spaces for *D* = 1.1 (left), *D* = 1.5 (middle), and *D* = 1.9 (right). While the branches of the 'exact' H-Trees in the top two rows are straight, the bottom row of 'statistical' H-Trees were generated by introducing a distribution of weave angles into the branches of the H-Trees in the middle row.

Study of the Geometric Origin of a Neuron's Fractal Properties

The first step taken towards addressing the question of which geometric features of a neuron's arbor contribute to its fractal properties is of course to create high-resolution models that faithfully represent its arbor. Figure 4-1A-D provides a visual representation of the process used to create three-dimensional models of the neurons examined in this chapter, those being pyramidal neurons from the CA1 region of the rat hippocampus. Figure 4-1A shows a schematic diagram of a coronal slice through the rat hippocampus and indicates the specific part of the CA1 region from which the neurons were imaged. Figure 4-1B shows an example of a stack of images that were taken using confocal microscopy and Fig. 4-1C uses one example image from a stack to indicate the various strata of the CA1 region in which these neurons' arbors reside. Axonal and dendritic arbors extend from neuron somas located in the stratum pyramidale (SP), with the dendritic arbor featuring component apical and basal arbors. The dendritic branches of the apical and basal arbors extend into the neighboring stratum radiatum (SR) and stratum oriens (SO), respectively, and adopt a complex branched morphology that is used to efficiently connect to and collect signals from the axons of other neurons[76]. Figure 4-1D shows an example three-dimensional reconstruction of a neuron's dendritic arbor created using a stack of confocal microscopy images. The axons that form synapses with these dendritic arbors originate either from within the CA1 region and connect to them from every direction (e.g. O-LM cells, basket cells, bistratified cells and axo-axonic cells)[211], or they originate from other regions such as the neighboring CA2 which extends axons parallel to the strata (e.g. Schaffer collaterals). Unless specified otherwise, the analyses presented throughout this chapter focus specifically on the neurons' basal arbors.

In principle, a neuron's dendrites could follow a perfectly straight line with dimension $D = 1$ or meander along a very winding trajectory that completely fills space with a dimension of $D = 3$. If the arbor features fractal dendrites instead of these integer dimensions characterizing Euclidean shapes, then each of these dendrites will be quantified by an intermediate D value lying between 1 and 3. The same, of course, is true when analyzing the entire dendritic arbor. Fractals with larger contributions of fine patterns will have higher D values than fractals with lower contributions of fine patterns. An initial examination of the size of the neurons' arbors showed that their mean arbor radius, R_A, was approximately 100 µm and that the mean volume occupied by their dendrites, V_m, was approximately 5000 µm^3. Converting R_A to a spherical volume and comparing this to V_m showed that the neurons' arbor occupied less than 1% of the space local to its dendrites, indicating that the arbors, and by extension their constituent dendrites, are very likely to have D values well below 3.

Because many mathematical fractals are generated by scaling the length of some feature, a clear place to start when examining the fractal properties of a neuron's arbor is to compare the scaling of its forking length, L, to that of H-Trees. Figure 4-9 shows the scaling relationship between the number of branches, N, with a given L/L_{max} measured for a $D = 1.4$ H-Tree (Fig. 4-9A, C, and E) and a typical neuron arbor (Fig. 4-9B, D, and F). Here, L has been normalized by L_{max}, which is defined as the maximum L value within any given arbor. The branch section levels are defined such that $i = 1$ corresponds to branch sections emerging from the soma, $i = 2$ to branch sections emerging from the first forks, etc., with neurons featuring a median of 7 levels (other common level assignments such as the Strahler scheme[215] generate similar findings to those below). The H-Tree exhibits a well-defined reduction in L/L_{max} as i increases (Fig. 4-9C) which translates into a power-law decrease in N as L/L_{max} increases (Fig. 4-9E). This power-law behavior is expected since it generates the scale invariance of fractal geometry: the magnitude of the data line's gradient in Fig. 4-9E equals the H-Tree's D value of 1.4. In contrast, this behavior is notably absent for the neuron

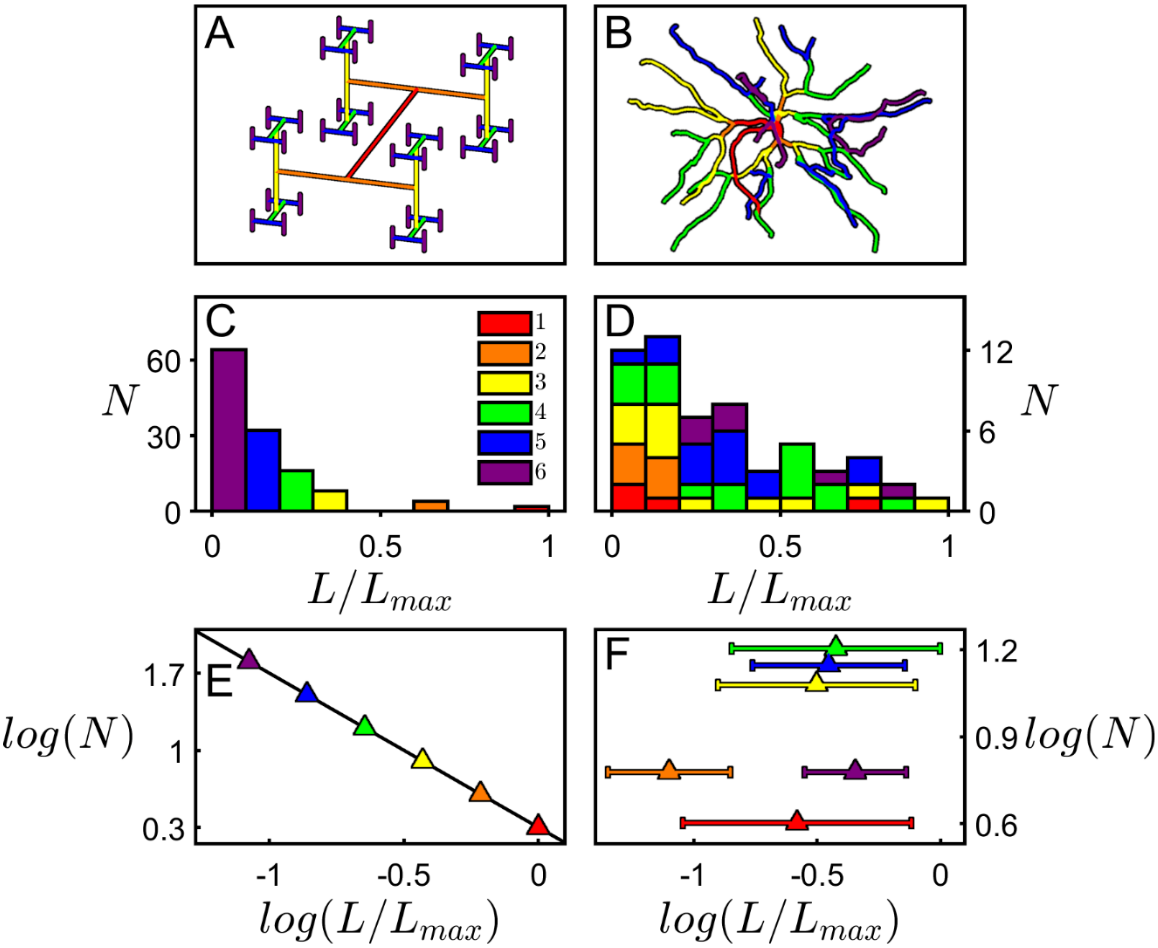

Figure 4-9. Comparison between the scaling properties of an H-Tree and a neuron arbor. (**A**) A D = 1.4 H-Tree and (**B**) an example neuron's arbor. The branch level, i, is colored as follows: red (1st branch level), orange (2nd), yellow (3rd), green (4th), blue (5th) and purple (6th). (**C**) Histogram corresponding to the H-Tree shown in (**A**) of the number of branches, N, with a given value of the normalized forking length, L/L_{max}. Here, the forking length, L, has been normalized to the maximum forking length, L_{max}. (**D**) The same as (**C**) but for the neuron shown in (**B**). Panels (**E**) and (**F**) show the analysis of (**C**) and (**D**) plotted in log-log space.

in Fig. 4-9D, L/L_{max} does not exhibit a systemic reduction in N with respect to i and consequently the Fig. 4-9F data does not follow a well-defined slope. Figure 4-10 shows the L/L_{max} distributions of six more example neurons, and demonstrates that while every neuron has a unique distribution, none of them exhibit a systemic reduction in N with respect to i. This result demonstrates that the L distribution alone is insufficient to generate the fractal character of the branches and indicates that in addition to branch lengths, the angles that determine the forking behavior along with the way branches weave between the forks must also play a role.

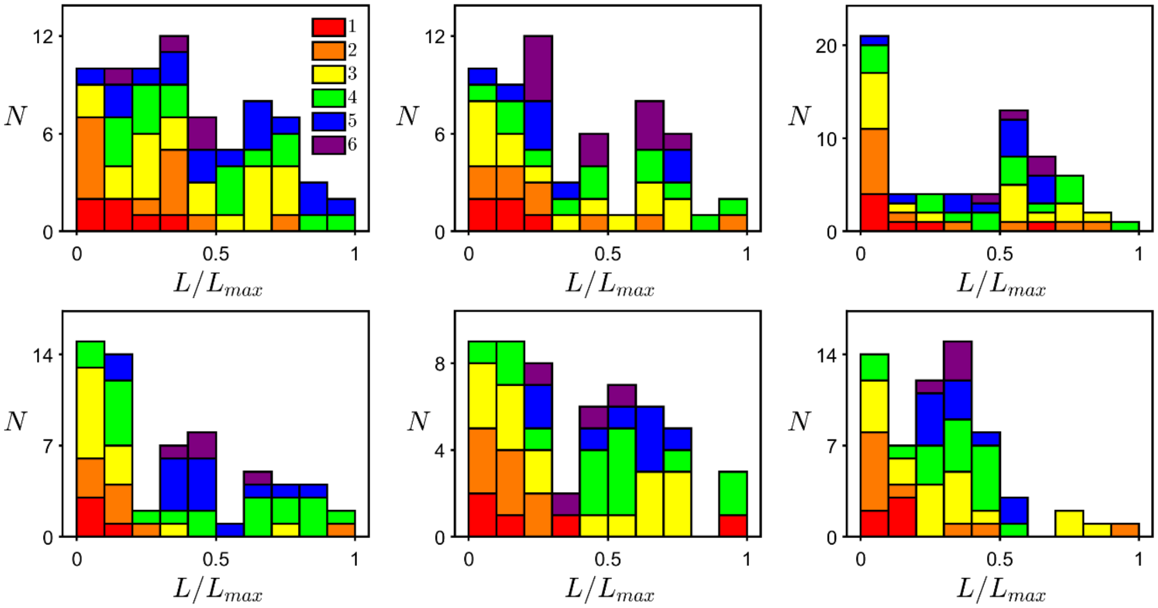

Figure 4-10. Extra examples of forking length scaling behavior of neuron arbors. Each panel shows the normalized forking length histogram of a different neuron's arbor for comparison with Fig. 4-9D. The legend shown in the top-left panel applies to all other panels.

Analysis of the Fractal Dimension of a Neuron's Branches

Within this section, two methods are presented for measuring the fractal dimension of a neuron's branches that accommodate the length scaling of a branch as well as its weaving and forking behavior. Initially, the results from a traditional method employed in the first demonstration of nature's fractality[207] are presented. This is followed by a novel method that examines a branch's tortuosity[208,216], T, across multiple scales. The measured branch fractal dimension, D_B, is then compared between the two methods.

The first method, termed the 'coastline' fractal analysis, is a three-dimensional extension of a traditional method pioneered by Richardson[207] and then Mandelbrot[25] in their discovery of the fractal character of meandering coastlines. The log-log scaling plot for this analysis is shown in Fig. 4-11A. Normalizing the ruler length, L_R, to the Euclidean distance separating the two ends of a branch, L_E, allows scaling plots for branches with different lengths to be plotted on a common x-axis. Figure 4-11B demonstrates that all of the branches within a given arbor condense onto a single line, indicating that they are quantified by a common fractal dimension, D_{BCN}. To extract D_{BCN}, the black data corresponding to the scaling range of L_R/L_E shared by all branches within the arbor (i.e. the region over which all of the individual plots overlap) is fitted. The red dots in Fig. 4-11B indicate the data that are excluded from the fit. The inset employs a histogram to compare the mean D_{BC} across all branches within the arbor, $\langle D_{BC} \rangle$, (1.031 as indicated by the cyan line) with D_{BCN} (1.032 as indicated by the red line). The scaling range of the fit in Fig. 4-11A is restricted to 1 order of magnitude to provide a standardized fitting procedure for extracting D_{BC}. Figure 4-12 shows the fit used in Fig. 4-11A when it is extended to larger scales so that it spans 1.5 orders. The inset provides a histogram showing a comparison of D_{BC} values for fits over 1 and 1.5 orders of all branches across all neurons long enough to have a scaling range up to 1.5 orders. It should be noted that the uncertainty associated with the measurement of D_{BC} cannot be calculated from the results of the simple linear regressions employed here. This is due to the lack of independence of the data being plotted, which results from the existence of correlations between the measured N_R values for given L_R values in a similar range. To better characterize the quality of these linear fits in future work, methods like maximum likelihood estimation[217] should be used to calculate the uncertainty of D_{BC}.

Figure 4-13 further demonstrates D_{BC}'s lack of dependence on branch length by plotting the values of all the individual branches across all of the neurons examined. A branch's 'path length', L_B, is given by the total length of all the cylindrical segments spanning

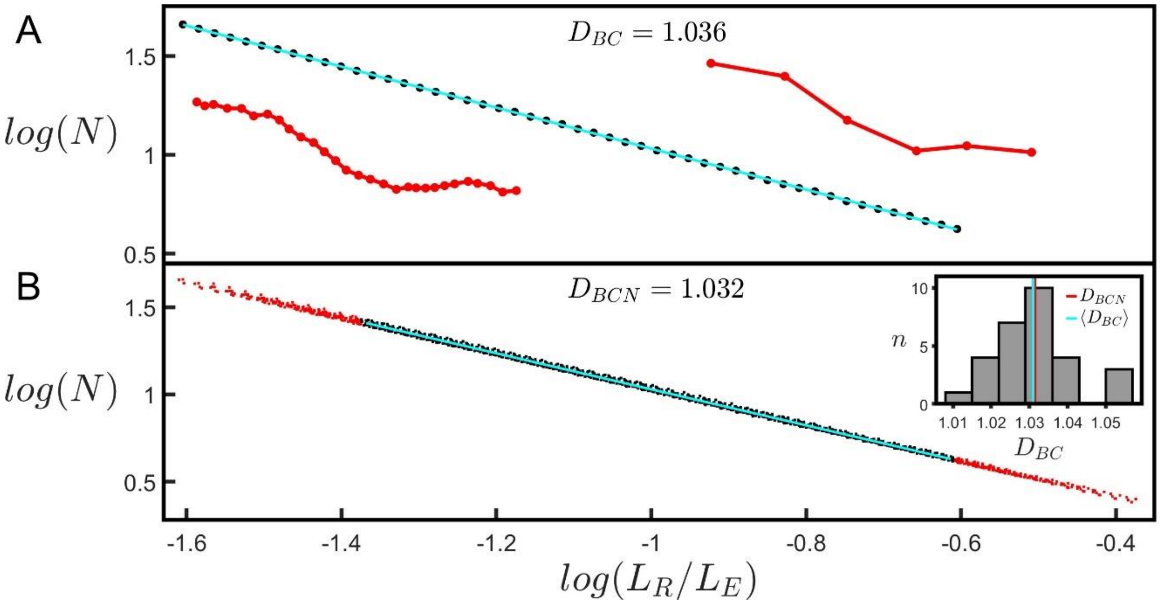

Figure 4-11. Coastline scaling analysis of a neuron's branch. (**A**) The coastline scaling plot of the number of rulers spanning the branch, *N*, versus the normalized ruler length, L_R/L_E, measured for a single branch within a natural neuron's arbor. The red insets show examples of segmented versions of the branch corresponding to ruler lengths of 6.4 µm (left) and 34.7 µm (right). The slope of the line yields a coastline fractal dimension, D_{BC}, of 1.036. (**B**) The equivalent coastline scaling plot including all the branches within the selected neuron's arbor. The black data correspond to the scaling range of L_R/L_E shared by all branches within the arbor, whereas the red data correspond to the range in which some branches do not contribute and are accordingly removed when fitting the data. The slope of the line yields a normalized coastline fractal dimension, D_{BCN}, of 1.032. The inset at the right shows a histogram of the number of branches, *n*, of a given D_{BC} within the neuron's arbor. The vertical red and cyan lines correspond to D_{BCN} and the mean coastline fractal dimension across all the branches within the neuron's arbor, $\langle D_{BC} \rangle$, respectively.

the branch from soma to tip (in terms of ruler measurement, L_B approximates to the total length of all rulers spanning the branch when the ruler is set to equal the smallest resolution possible). Although D_{BC} can vary considerably between individual branches, their collective behavior reveals an independence of D_{BC} with respect to L_B. The branch weave and forking angles, labelled as θ and ϕ, respectively, have also been mathematically manipulated by multiplying every θ and ϕ value by a common factor α (Fig. 4-1E shows a schematic indicating example measurements of θ and ϕ). This changes the D_{BC} values as follows.

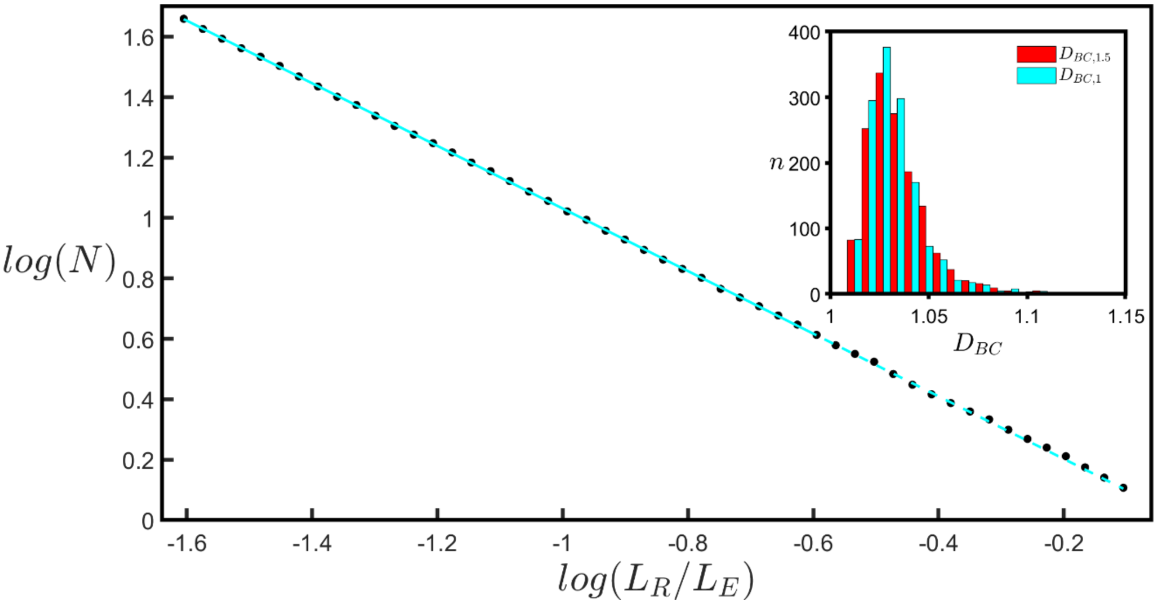

Figure 4-12. Examination of the coastline fractal analysis scaling range. The coastline scaling plot of the number of rulers spanning the branch, N, versus the normalized ruler length, L_R/L_E, measured for the same neuron branch shown in Figure 4-11A. The solid cyan line represents the fit used to extract D_{BC} over the 1 order of magnitude scaling range seen in Figure 4-11A, while the dashed cyan line represents the extension of this fit up to 1.5 orders of magnitude. The upper-right inset shows a histogram comparing the D_{BC} values extracted from fits over 1 (cyan) and 1.5 (red) orders of magnitude for all branches across all neurons long enough to have a scaling range up to 1.5 orders.

Values of α higher than 1 increase the angles above their natural values and cause the neuron branches to curl up, causing D_{BC} to rise because the amount of fine structure in the branch's shape increases. Similarly, reducing α causes the branches to gradually straighten out, decreasing the amount of fine structure, and causing D_{BC} to drop. The insets at the top of Fig. 4-13 provide a visual demonstration of this curling process.

Whereas the coastline method considers the entire length of the branch and examines how the branch properties change with measurement resolution, the second method used to investigate a branch's fractal behavior considers the finest resolution and examines how the branch properties vary when investigating increasingly small sections of the branch. This second approach aligns with one of the traditional measures of tortuosity, T, that quantifies

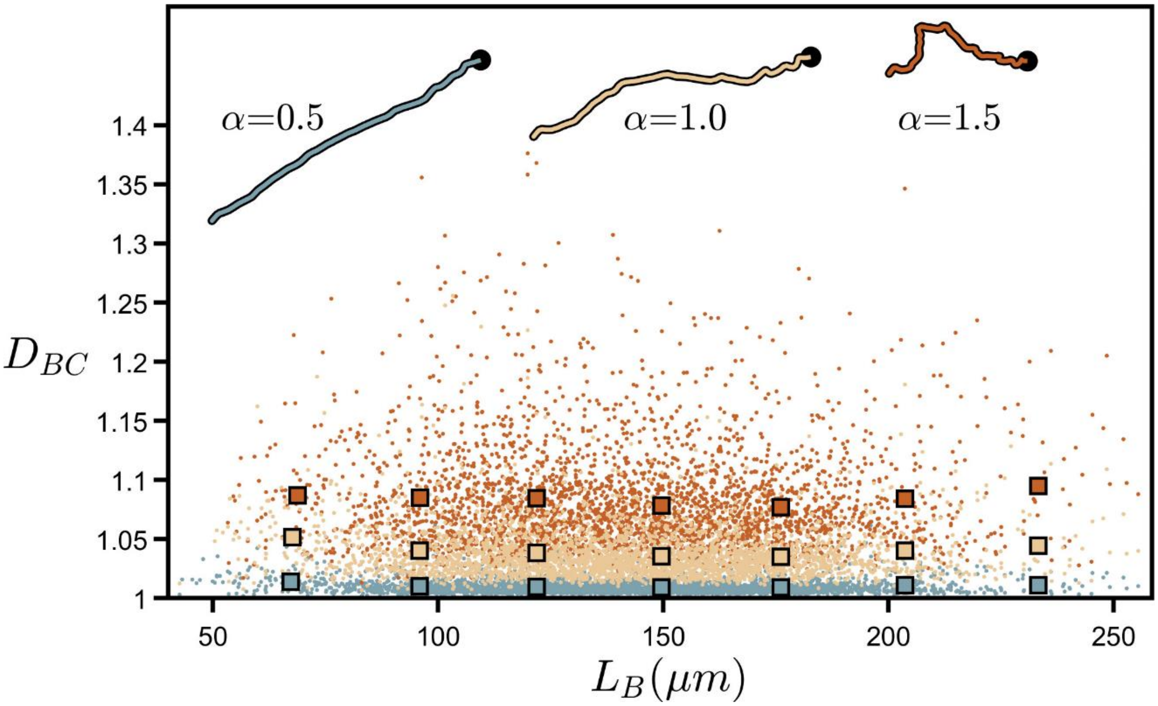

Figure 4-13. Examining the independence of coastline fractal dimension on branch length. Coastline fractal dimension, D_{BC}, plotted against branch length, L_B, (measured in µm) for all of the branches across all neurons. The larger, outlined squares indicate binned averages of the underlying data in the range of 50 to 250 µm. The upper insets show the path of a single neuron branch for three values of α where the location of the neuron's soma is indicated by the black dot. The colors of the data shown in this plot correspond to the α values shown in the insets.

the extent to which the meandering branch deviates from a straight trajectory. Several different tortuosity metrics have been used in previous studies of a variety of biological structures[208,216,218–221]. Due to its mathematical connection to fractal measurement, the definition of tortuosity that is used in the subsequent analyses is based the ratio of a path's curvilinear length, L_P, to the Euclidean distance between the two endpoints of that path, L_D (which is equivalent to the largest ruler length spanning the branch section).

By measuring the L_P and L_D values (see Fig. 4-4B for a schematic illustrating an example measurement of L_P and L_D) of many differently sized paths along the branches of all the neurons and averaging the resulting T values across all of these branches, the relationship between T and L_P can be charted. Figure 4-14 shows this relationship plotted over the same scaling range (4 to 40 µm) used to measure D_{BC} (Fig. 4-11A). Note that the exact values of the x-axes are different only because of the normalization scheme used in the coastline fractal analysis. Given the mathematical relationship between T and the coastline method, T is expected to follow the power-law relationship with L_P revealed in Fig. 4-14, with the slope, S, of the log-log plot related to branch fractal dimension using Eq. 4-7. Accordingly, increasing α results in the data following a steeper trend. The inset of Fig. 4-14 confirms intuition that the T value averaged across the data line will increase with α.

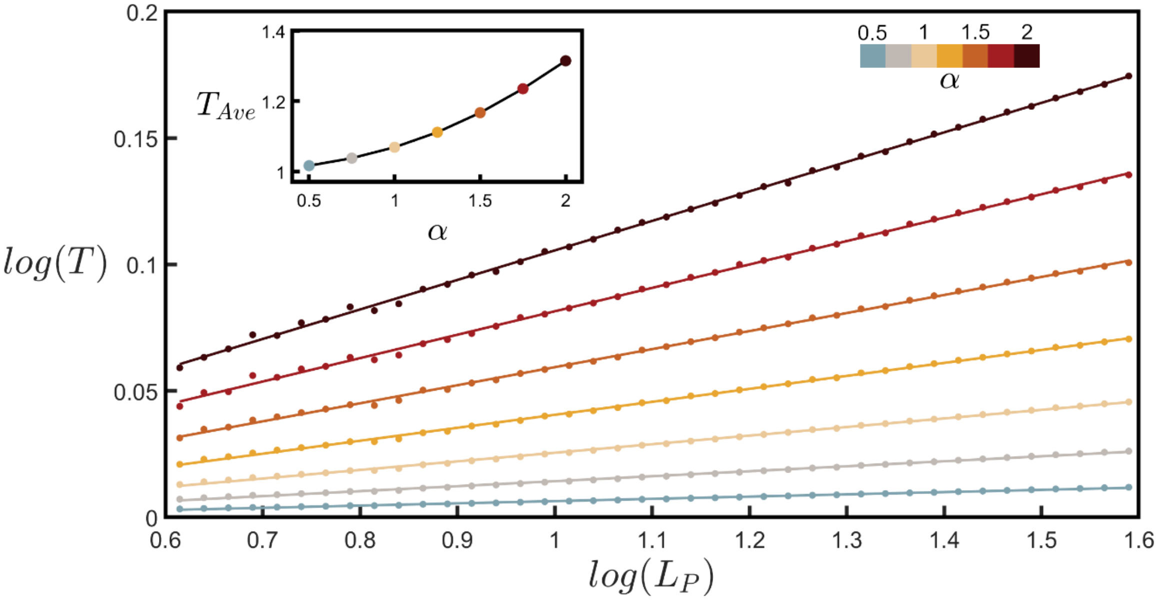

Figure 4-14. Tortuosity fractal analysis of all neuron branches. Scaling plot of tortuosity, T, against path length, L_P, (measured in µm) for seven values of α as indicated by the upper-right color bar. The data shown represent binned averages of T across all possible paths within all of the branches across all neurons. The upper-left inset shows how the average value of tortuosity across the L_P range examined in the main plot, T_{Ave}, increases with α.

Figure 4-15 plots D_{BC} against D_{BT} measured for all of the individual branches across all neurons and allows for a direct comparison of the two techniques used for determining branch dimension. The black line indicates the expected relationship, $D_{BC} = D_{BT}$. To compare the data to this line, for each α value the D_{BC} value averaged across all branches across all neurons is also plotted. Recognizing that the tortuosity scaling plots for the individual branches are inherently more noisy than the equivalent coastline scaling plots (compare Fig. 4-11A and Fig. 4-16 which show the scaling behaviors for the same branch), the D_{BT} values obtained from the procedure shown in Fig. 4-14 which benefits from fitting the combined data of all neurons are also plotted. Given the scatter observed in the individual branch data points, the close match of the two techniques to the line is impressive. In addition to demonstrating the power of confirming branch dimension using two techniques, Fig. 4-15 also emphasizes that neuron fractal behavior varies considerably from branch to branch, but nevertheless systematic behavior emerges when looking across the collective behavior of many neurons.

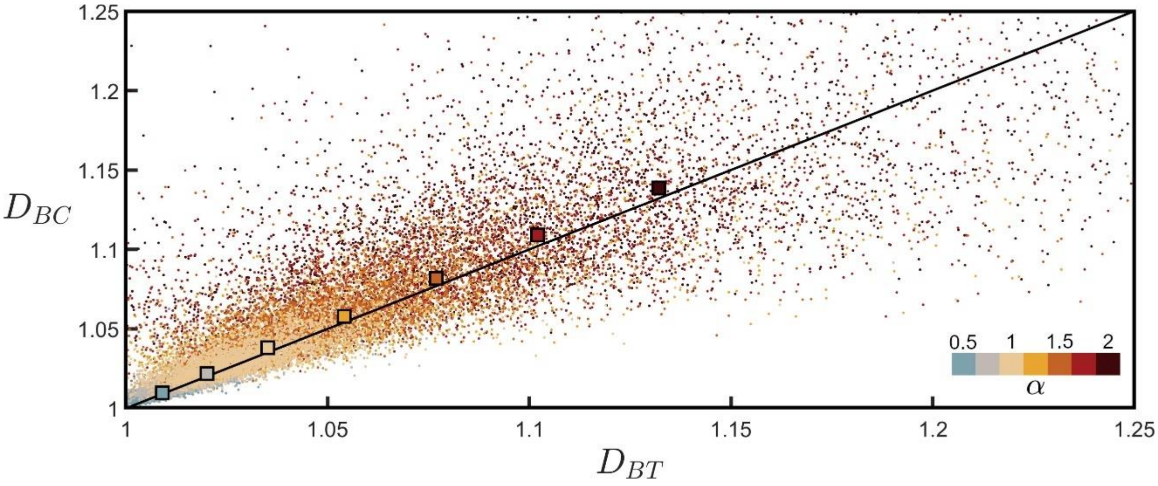

Figure 4-15. Comparison of the coastline and tortuosity fractal dimensions. Coastline fractal dimension, D_{BC}, plotted against tortuosity fractal dimension, D_{BT}, for all of the branches across all neurons for seven values of α. The lower-right color bar indicates the α value of the corresponding data. The larger, outlined squares show the mean of the underlying D_{BC} data points plotted against the D_{BT} value extracted from Figure 4-14 for each α value. The black line indicates $D_{BC} = D_{BT}$.

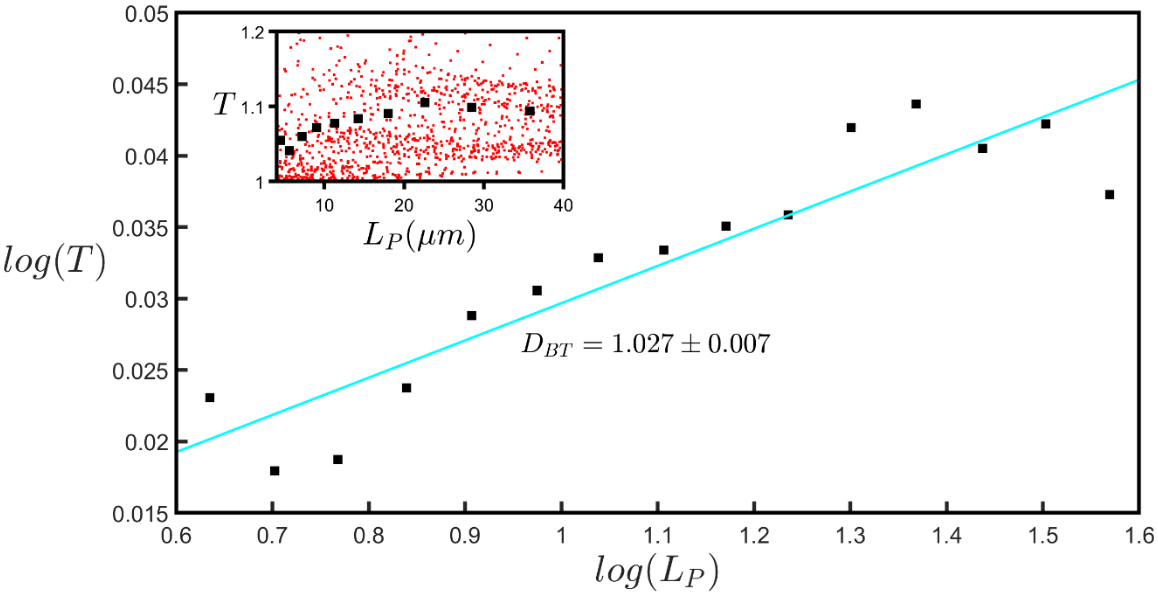

Figure 4-16. Tortuosity fractal analysis of a single neuron's branch. Double-logarithmic plot of tortuosity, T, (unitless) versus path length, L_P, (measured in μm) for the same branch shown in Fig. 4-11A. Each black square represents the average T value of all possible paths within the branch for the given L_P value. The cyan line shows the fit used to calculate the branches tortuosity fractal dimension, D_{BT}. The inset demonstrates the averaging procedure by plotting T versus L_P, where each red dot represents a single path along the branch and the black squares represent their binned averages (which correspond to those shown in the main plot).

Analysis of the Fractal Dimension of a Neuron's Arbor

With the fractal behavior of the neurons' branches now established using the coastline and tortuosity scaling analyses, two more techniques will be applied to investigate the fractal behavior of the neurons' arbors. First, the cumulative mass fractal analysis will be employed, a technique that can be related to Sholl analysis, a traditional measure of the complexity of a neuron's arbor[222]. The box-counting fractal analysis will then be employed, and its results compared with the cumulative mass fractal analysis. Though each technique probes the scaling behavior of a neuron's arbor in a unique way, they both quantify the fractal dimension of the arbor by examining the relative contributions of coarse and fine scale structure to the arbor's morphology.

Beginning with the cumulative mass analysis (also referred to as the mass-radius method), this technique charts the total length of dendrites, L_{in}, within a sphere of radius r as the radius of the sphere increases. Similarly, the modified Sholl analysis measures the number of intersections, N_I, of an arbor's branches with spherical shells of increasing radii. Figure 4-17 shows the results of these analyses when applied to a set of neuron arbors. As r increases, both N_I and L_{in} rapidly increase, with N_I displaying a maximum of 21 at $r = 73$ µm, followed by a decrease as r nears the mean arbor radius, R_A, of 98 µm. While the increase in N_I and L_{in} reflect the fractal character of the repeating patterns established by the arbors' branches[208,209], the decrease in N_I is a consequence of the measurement technique – it reflects the increased chance of the larger outer spherical shells reaching beyond the space occupied by the dendrites. The observed saturation in L_{in} for large r (which approaches the mean of the sum of all of an arbor's forking lengths) indicates that the fractal scaling behavior must exist over a limited range, as expected for any finitely sized physical object. Figure 4-18A, which plots L_{in} versus r on a double-logarithmic scale, provides an example measurement of the mass fractal dimension, D_M, of a given neuron's arbor.

Whereas the cumulative mass analysis provides a link to traditional neuroscience research through its relationship to Sholl analysis, the box-counting analysis is a commonly adopted technique within fractal studies. Similar to the coastline fractal analysis, which counts the number of rulers as ruler size is reduced, the box-counting analysis replaces the rulers with boxes to accommodate the fact that the arbors feature multiple branches. Figure 4-18B shows the results of the box-counting analysis when applied to the same arbor seen in Fig. 4-18A, plotting the number of boxes occupied by an arbor, N_{box}, versus the box size, L_{box}. The range of L_{box} used to measure the arbor fractal dimension, D_A, in the box-counting

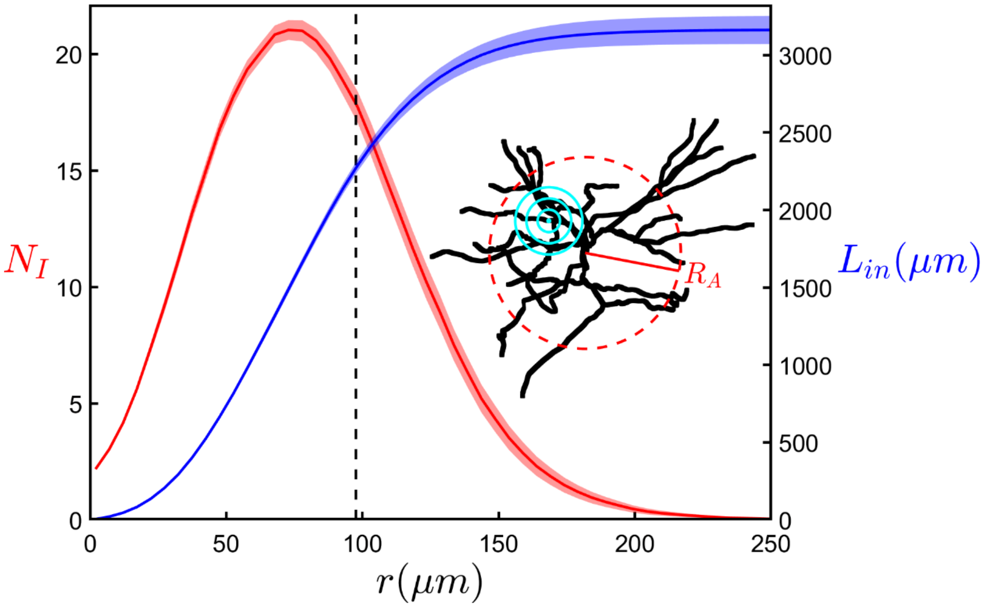

Figure 4-17. Comparison of modified Sholl and cumulative mass analyses. The results of a modified Sholl analysis (red) measuring the average number of intersections of an arbor's dendrites, N_I, with a sphere surface of radius r, and a cumulative mass analysis (blue) measuring the total length of all dendrites, L_{in}, within a sphere of the same radius. Each curve represents the mean behavior across a set of arbors and the shaded region around each curve shows the standard error from the mean. The inset shows an example neuron's arbor with its arbor radius, R_A, denoted by the red dashed ring and example sphere radii used in the analyses denoted by the concentric cyan rings. The black dashed line at 98 μm indicates the mean arbor radius.

analysis was also applied to the range of r used to measure D_M. Figure 4-19B shows how the fractal behavior of an arbor starts to break down outside of the range of L_{box} seen in Fig. 4-19A and provides distributions of the D_A values of both the apical and basal arbors of the neurons in Fig. 4-19C. The means of the distributions are $D_A = 1.42$ (basal) and 1.43 (apical), indicating that their branches have similar scaling characteristics despite the apical arbors having longer branches that typically feature more forks.

Although the cumulative mass and box-counting analyses yield fractal measurements that are in agreement with one another, it is clear from Fig. 4-18 that the results of the linear regression in the box-counting analysis, yielding $D_A = 1.40$, correspond to a better fit than the results of the cumulative mass analysis, yielding $D_M = 1.42$. It should be noted that both

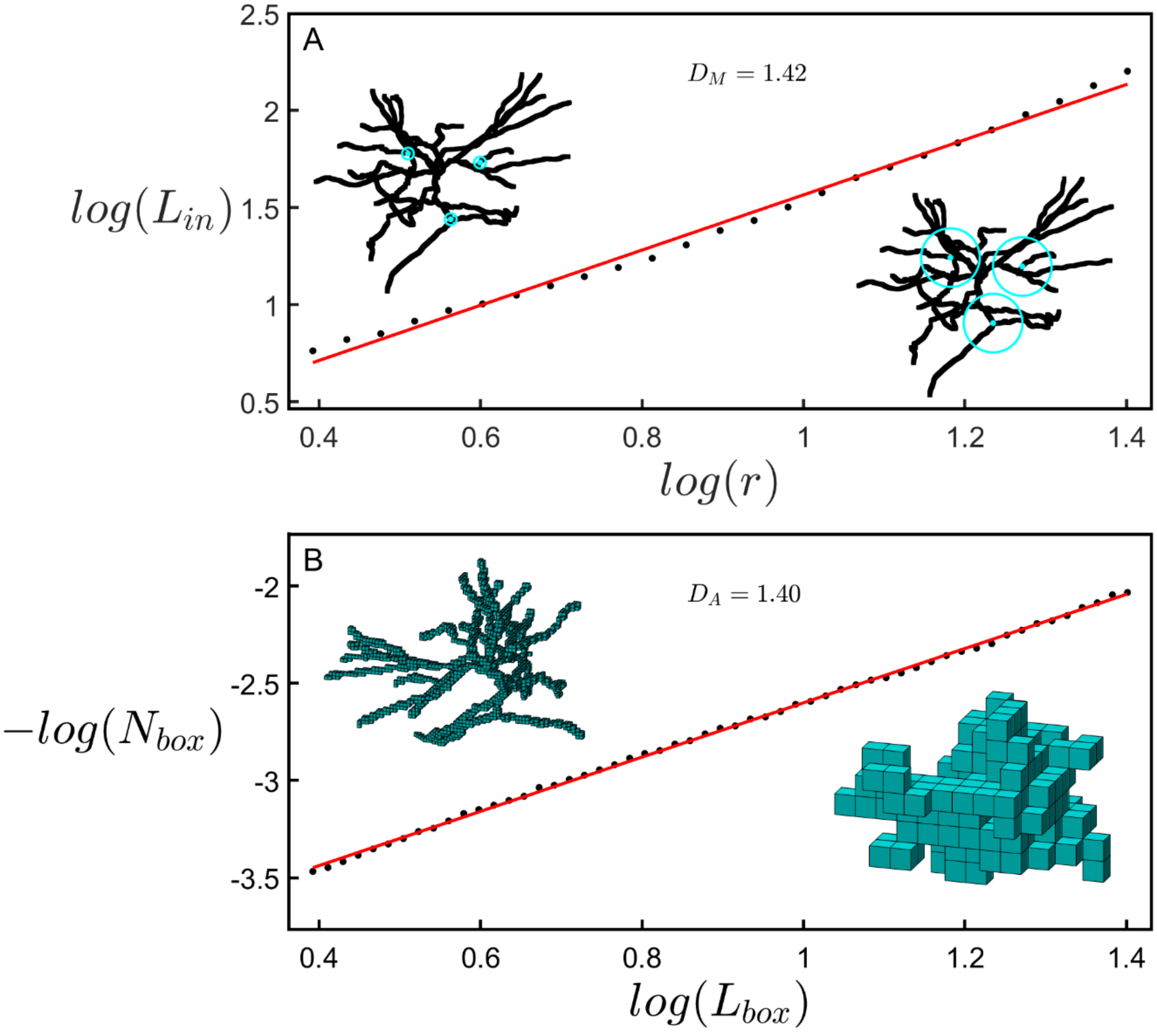

Figure 4-18. Comparison between mass and box-counting fractal analyses. (**A**) A scaling plot of the cumulative mass analysis showing the total dendritic length, L_{in}, within a sphere plotted against its radius r. The left inset shows rings with a radius of 5µm at 3 example locations on a neuron while the right inset shows spheres with a radius of 25 µm at the same locations. (**B**) A scaling plot of the number of boxes occupied by a neuron, N_{box}, plotted with respect to the size of the boxes, L_{box}. The left inset shows a representation of the space occupied by a neuron at a box size of 3.1 µm while the right inset shows the same neuron at a box size of 20.3 µm.

D_M and D_A belong to a spectrum of dimensions and their magnitudes can be compared using a multi-fractal analysis[223,224]. For the neuron arbors examined here, the box-counting analysis serves as a more global measure of fractality because it accommodates the whole arbor while the cumulative mass analysis is biased towards the central section (through its

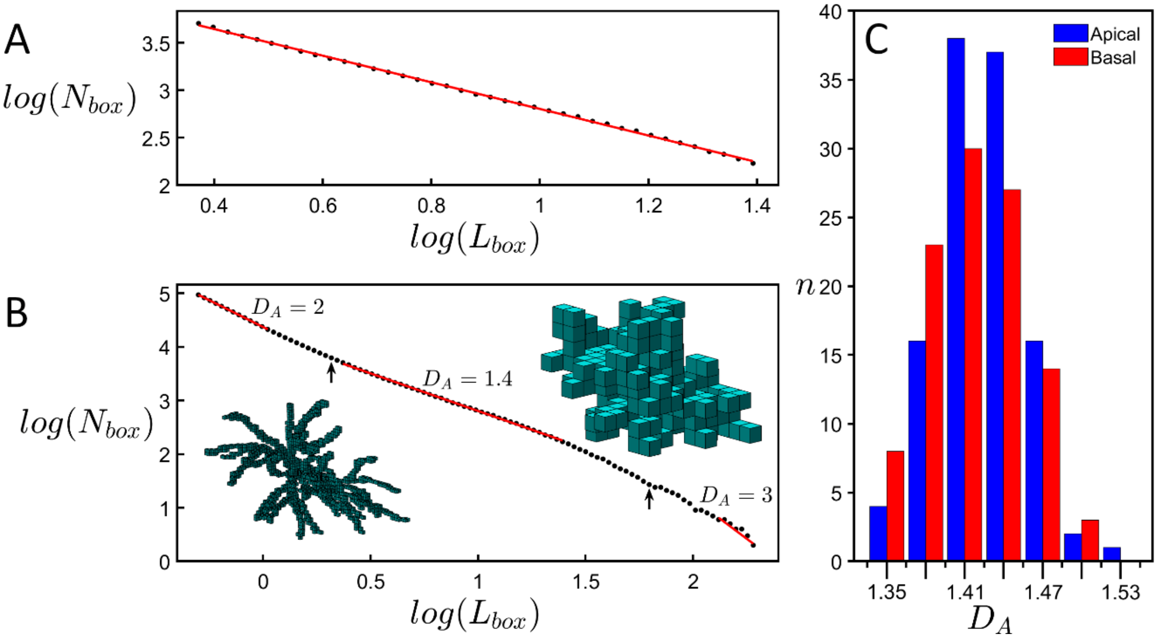

Figure 4-19. Box counting fractal analysis of a neuron's arbor. (**A**) Example log-log scaling plot of the number of boxes occupied by a neuron's arbor, N_{box}, versus the box size, L_{box}, used when measuring arbor fractal dimension, D_A. (**B**) Expanding the scaling plot in (**A**) to cover a larger range of L_{box} shows the size scales at which the scaling properties of the arbor transition to the Euclidean conditions, $D_A = 3$ at the large scale and $D_A = 2$ at the small scale. The transition to $D_A = 2$ at the small scale occurs because the reconstructed arbor models are made of hollow cylinders whose surface is two-dimensional. The insets show the boxes occupied by the arbor at small (4 µm) and large (20 µm) box sizes. The arrows indicate the limits used when determining the scaling range used to measure the arbor's D_A value. (**C**) Histogram of the number of arbors, n, with a given D_A value for both the apical and basal arbors.

restriction of the local sphere centers to be within $R_A/\sqrt{2}$ of the center of mass of the arbor). If the arbor's branches start to, for example, weave or fork less towards the arbor periphery, a dimension that measures the whole arbor would be expected to be lower than one that focuses on the central region.

While the observed differences between D_A and D_M are relatively small, based on this potential effect and also on the relative qualities of the associated fits, D_A will be focused on throughout the rest of this chapter because its associated functional parameters similarly quantify the neuron's whole arbor. However, both dimensions highlight two intriguing qualities: 1) the spatial interaction of the branches and gaps in the arbor generates a much greater fractal complexity than that displayed by the individual branches, 2) given that the arbor could assume a fractal dimension up to 3, the fractal complexity is nevertheless relatively low when compared to the capacity of some mathematical fractals to fill space.

Charting the Relationship Between Functionality and Fractal Dimension

Transitioning into an analysis of the dependence of a neuron's functionality on its fractal behavior, it is prudent to begin by clarifying the way in which functionality is measured here before examining how a neuron is impacted by distortions away from its natural morphology. The functionality of a neuron is tied to its ability to efficiently form a vast, connected network with other neurons. The connections within this network depend on the dendritic arbors of neurons forming synapses with the axonal arbors of other neurons. A useful proxy for measuring the connectivity of a neuron is its profile area[208], which captures the potential of a neuron's dendritic arbor to connect to passing axons. Large dendritic arbors have large profiles and therefore a better chance of connecting to passing axons. However, the metabolic costs of an arbor, which have been associated with both mass and surface area[79,225], also increase with size. As such, the morphology of a neuron's arbor must provide it with a delicate balance between connectivity and cost in order to effectively fulfill its functional role.

Given the relationship between a neuron's morphology and its functionality, it is useful to examine the impacts of distortions away from the neuron's natural morphology. By simultaneously changing the forking and weaving behavior of the branches within a neuron's arbor, the arbor is brought away from its natural self-avoiding state. Figure 4-20 demonstrates this by plotting D_A against the angle multiplier, α, and showing that both increasing and decreasing α results in a rise in D_A. This effect can be understood in terms of the interplay of the fractal branches and gaps. When α increases or decreases from 1 (i.e. the natural condition), the branches deviate away from their natural self-avoiding state and so move closer together. This generates an increase in the ratio of fine to coarse structure and a corresponding rise in D_A. This effect is visualized by the upper insets of Fig. 4-20, which show an example arbor for the natural case (middle) and for lower (left) and higher (right) α values.

Figure 4-20 also demonstrates that distortions in a neuron's arbor away from its natural state impact its ability to efficiently connect to axons passing through the arbor. Here, connectivity efficiency, P/A_s, is measured as the ratio of an arbor's average profile area, P, to the total surface area of all its branches, A_s. This metric has been adopted because previous studies have established that the arbor's physical structure is sufficient for describing the connection process, with chemical steering playing a relatively minor role[226,227]. In particular, the arbor's dendritic density[82,228–230] and resulting physical profile[231] are powerful indicators of its potential to connect to other neurons. When viewed from a particular orientation, P is measured as the total projected area of its arbor. Large profiles will therefore result in the increased exposure of synapses, which are responsible for receiving signals from other neurons. When calculating the profile from the arbor projections, an extra layer (colored orange in Fig. 4-20 upper inset and Fig. 4-7) is incorporated surrounding the branches (colored black) to account for outgrowth of dendritic spines - small protrusions which provide the majority of an arbor's synaptic connections. For each arbor shown in the upper insets of Fig. 4-20, P is therefore the sum of the projected black and orange areas. P has been normalized by A_s to accommodate for the range in neuron sizes and associated surface areas.

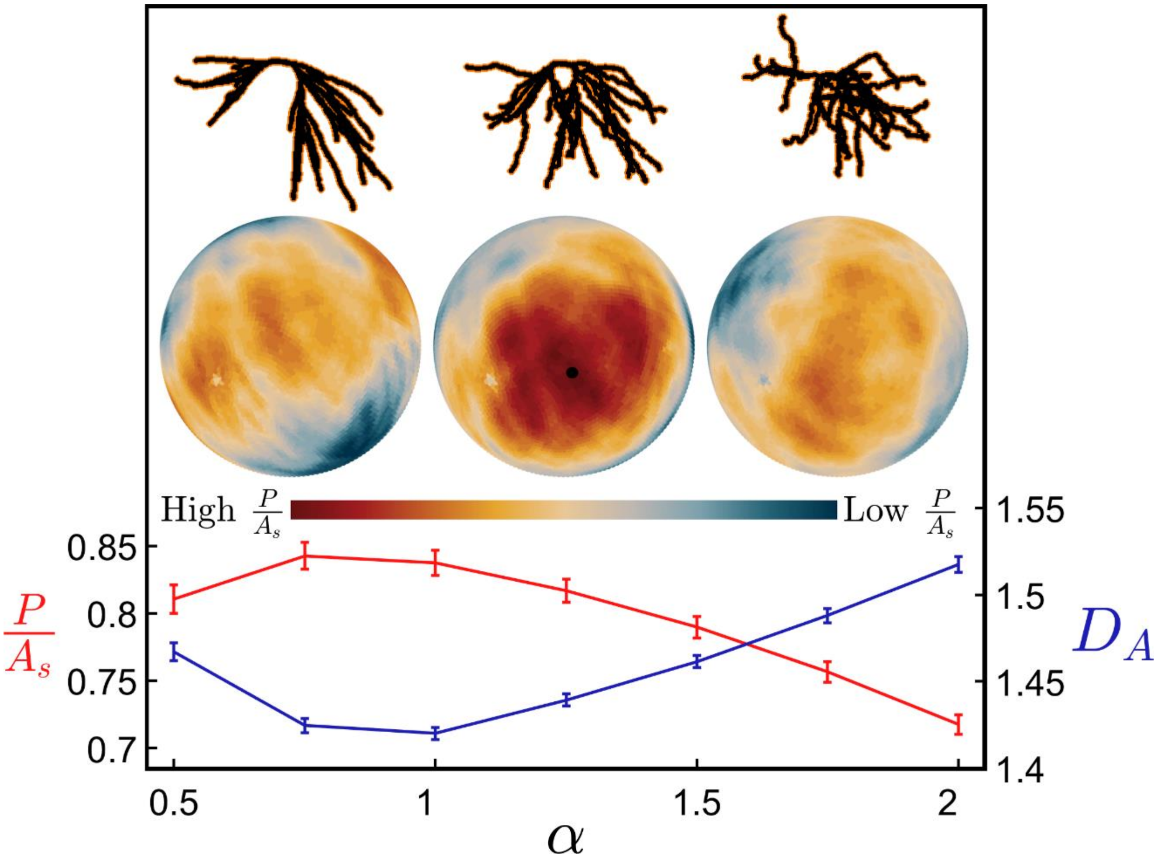

Figure 4-20. Examining the impact of the angle multiplier on neuron arbor fractal dimension and profile blocking. Plot of P/A_s (the arbor's profile, P, averaged over all orientations and normalized to the arbor's surface area, A_s) (red) and arbor fractal dimension, D_A, (blue) against α. Both the red and blue lines show the mean across all arbors and their variations are represented by the shown standard errors from the mean. The upper insets show an example neuron's arbor for $\alpha = 0.5$ (left), 1 (middle), and 1.5 (right). The lower insets show the profile spheres corresponding to the arbors they are under. The black dot on the middle profile sphere indicates the orientation with maximal P/A_s for the middle arbor. The color bar corresponds to the range of P/A_s values shown on the profile spheres and all three profile spheres have been plotted over the same range.

The general approach of averaging P/A_s across all orientations of the arbor has been adopted to allow for the fact that axons originating from within the CA1 region connect to the dendritic arbors from every direction[211]. The profile variation with orientation can be visualized by mapping the P/A_s values obtained from each orientation onto a spherical surface. The profile spheres and neurons shown in the insets of Fig. 4-20 have been viewed from a common direction which corresponds to the middle point on each profile sphere's surface. For the natural arbor, the orientation for which P/A_s peaks is marked by the black dot. Typically, this peak occurs in the direction that the Schaffer collateral axons enter from the CA2 region[76] and so maximizes the connectivity of the natural neurons to those incoming axons.

The inverse relationship between P/A_s and D_A observed when distorting the neuron arbors can be traced to the increased fine structure of high D_A neurons causing branches to block each other and so reduce the overall profile. Including this blocking effect is important for capturing the neuron's connectivity because multiple connections of an axon to the same dendritic arbor are known to generate redundancies[231]. Therefore, if a straight axon is connected to an exposed branch, subsequent connections to blocked branches wouldn't increase the connectivity and should be excluded. Figure 4-21A summarizes this blocking effect by plotting P/A_s directly against D_A for the natural and distorted arbors together. Figure 4-21B demonstrates that this blocking reduction in P/A_s is also seen for H-Trees (which have had a statistical weave incorporated their branches as seen in Fig. 4-8), highlighting that the blocking dependence on D_A is general to fractals. Figure 4-21C and D explore another well-known fractal effect that high D_A fractals increase the ratio of the object's surface area, A_s, to its bounding area, A_b,[16,86] (i.e. the surface area of the volume containing the arbor, as quantified by its convex hull). Figure 4-21E and F combines the 'increased surface area effect' seen in Fig. 4-21C and D with the 'blocking area effect' seen in Fig. 4-21A and B by plotting the connectivity density, P/A_b, (i.e. the multiplication of P/A_s and A_s/A_b) against D_A. In effect, P/A_b quantifies the large surface area of the arbor while accounting for the fact that some of this area will be blocked and therefore excluded from the profile P. Normalizing P using A_b serves the additional purpose of measuring the arbor's potential connectivity in a

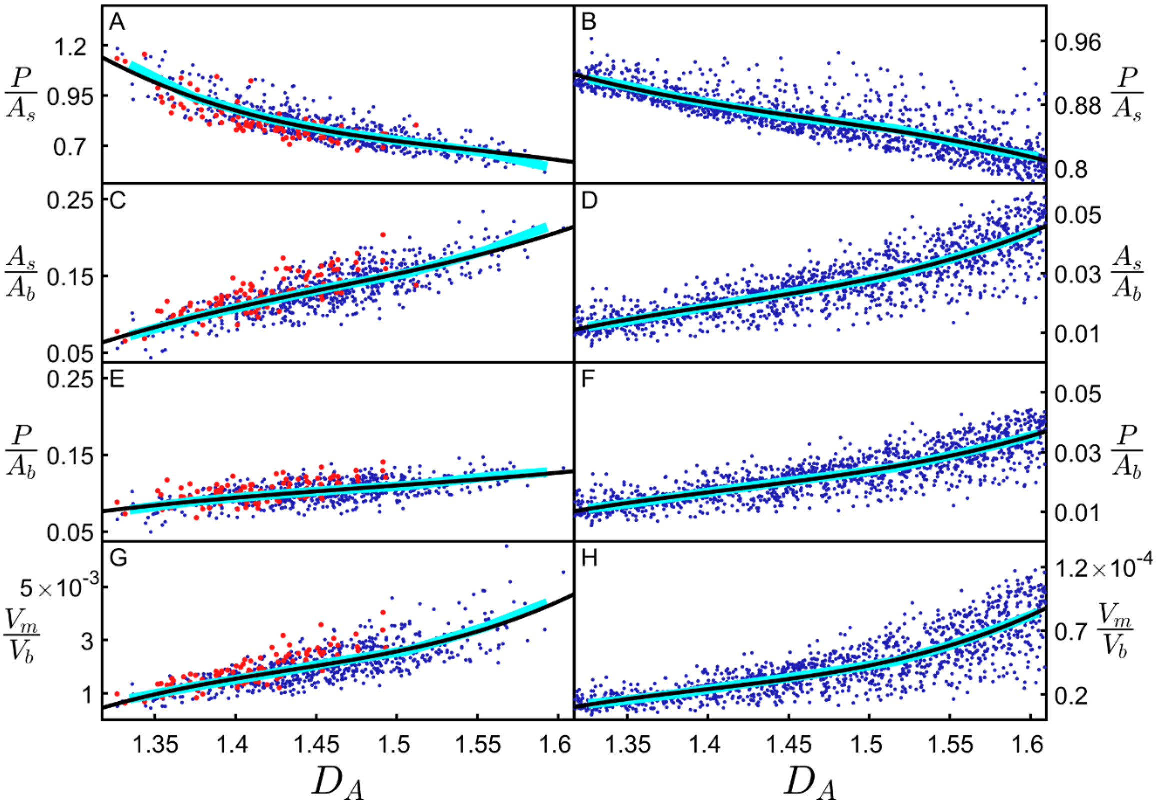

Figure 4-21. Study of the relationship between arbor fractal dimension and neuron functionality. Dependences of the functional parameters P/A_s, A_s/A_b, P/A_b, and V_m/V_b on arbor fractal dimension, D_A, for neurons (left column) and H-Trees (right column). For the data shown in the left column, the red scatter corresponds to the natural arbors while the blue scatter corresponds to the distorted arbors. For the data shown in the right column, all the scatter is blue and includes H-Trees with both straight and weaving branches. The cyan lines represent binned averages of the underlying data, and the black lines show 3rd degree polynomial fits to the data.

way that is independent of its size. Accordingly, P/A_b serves as an effective measure of the neurons' capacity to form a network.

The clear rise in P/A_b revealed by Fig. 4-21E and F highlights the functional advantage offered by high D_A arbors – incoming axons will experience the large connectivity density. Note that the plotted connectivity density is for individual neuron arbors. Because of the inter-penetrating character of the arbors of neighboring neurons, the collective connectivity density will be even larger due to their combined profiles. If this functionality was the sole driver of neuron morphology, then all neurons would therefore exploit high D_A values approaching 3. Yet, both the apical and basal arbors cluster around relatively low values of $D_A = 1.41$ suggesting that there are additional, negative consequences of increasing D_A. Figure 4-21G and H plots the ratio of the volume occupied by the branches, V_m, to the neuron's bounding volume, V_b, (i.e. the arbor's convex hull volume). The more densely packed structures associated with high D_A arbors produce the observed rise of V_m/V_b. Assuming constant tissue density, V_m is proportional to the neuronal mass, and the rise in V_m/V_b therefore quantifies the increase in mass density and associated 'building' costs of high D_A arbors. Aside from this, there is also an 'operational' cost. It is well-known from allometric scaling relationships that metabolic costs generally increase with mass[225,232]. Specifically, previous research proposed that the amount of ATP expended by neurons increases with A_s[79,231]. Revisiting Fig. 4-21A and C, A_s/A_b therefore charts how the normalized energy cost increases with D_A, and P/A_s measures how efficiently an arbor establishes a given connectivity.

Taken together, the panels of Fig. 4-21 summarize the competing consequences of increasing D_A for both the neurons and H-Trees: the benefits of enhanced connectivity density increase (Fig. 4-21E and F), but so does the cost of building (Fig. 4-21G and H) and operating (Fig. 4-21C and D) the arbor. The distinct forms of these three factors are highlighted using 3rd degree polynomial fits (black) which closely follow the binned average values of the data (cyan). This observation of neuron behavior across large D_A ranges provides a clear picture of their tolerances for the above factors and highlights both the shared behavior and subtle differences to standard mathematical fractals such as H-Trees. In particular, the high operating cost, the sharp increase in building cost, and the flatter gradient of the connectivity efficiency curve at high D_A could explain why the natural neurons (red) don't exceed $D_A = 1.51$. Nor do they occur below $D_A = 1.33$ because of the low connectivity density. To explore how the neurons' fractal structure balances these factors, Fig. 4-22 plots the ratios of the rates of change of connectivity density with operating cost

$$R_{PA} = \frac{\frac{d}{dD_A}\left(\frac{P}{A_b}\right)}{\frac{d}{dD_A}\left(\frac{A_s}{A_b}\right)} \qquad \text{(Eq. 4-12)}$$

and with building cost

$$R_{PV} = \frac{\frac{d}{dD_A}\left(\frac{P}{A_b}\right)}{\frac{d}{dD_A}\left(\frac{V_m}{V_b}\right)} \qquad \text{(Eq. 4-13)}$$

as proposed optimization indicators with the prediction that peaks in R_{PA} and R_{PV} indicate the D_A value near which the optimal balance occurs. By definition, R_{PA} and R_{PV} chart how changes in D_A impact the rate of change of connectivity density with respect to the rates of change of operating and building costs, respectively. Given that connectivity density, operating cost, and building cost all increase with D_A, a neuron must carefully develop its arbor in such a way to maximize increases in connectivity density (captured by the derivative of P/A_b) while minimizing increases in cost (captured by the derivatives of V_m/V_b and A_s/A_b). Larger values of R_{PA} and R_{PV} indicate that increases in D_A correspond to larger increases in connectivity density with respect to the associated increases in cost. For a neuron to have an arbor that optimally balances these functional constraints, it needs to achieve the largest values of R_{PA} and R_{PV}. Interestingly, though these proposed optimization indicators are fairly simple, Fig. 4-22 demonstrates that their associated connectivity-cost optimization curves generated peaks close to the natural neurons' mean D_A value of 1.42. This suggests that although high D_A structures offer superior connectivity density, the positive consequences of increasing D_A beyond the peaks in R_{PA} and R_{PV} rapidly diminish in terms of the increasing operating and building costs associated with those high D_A values.

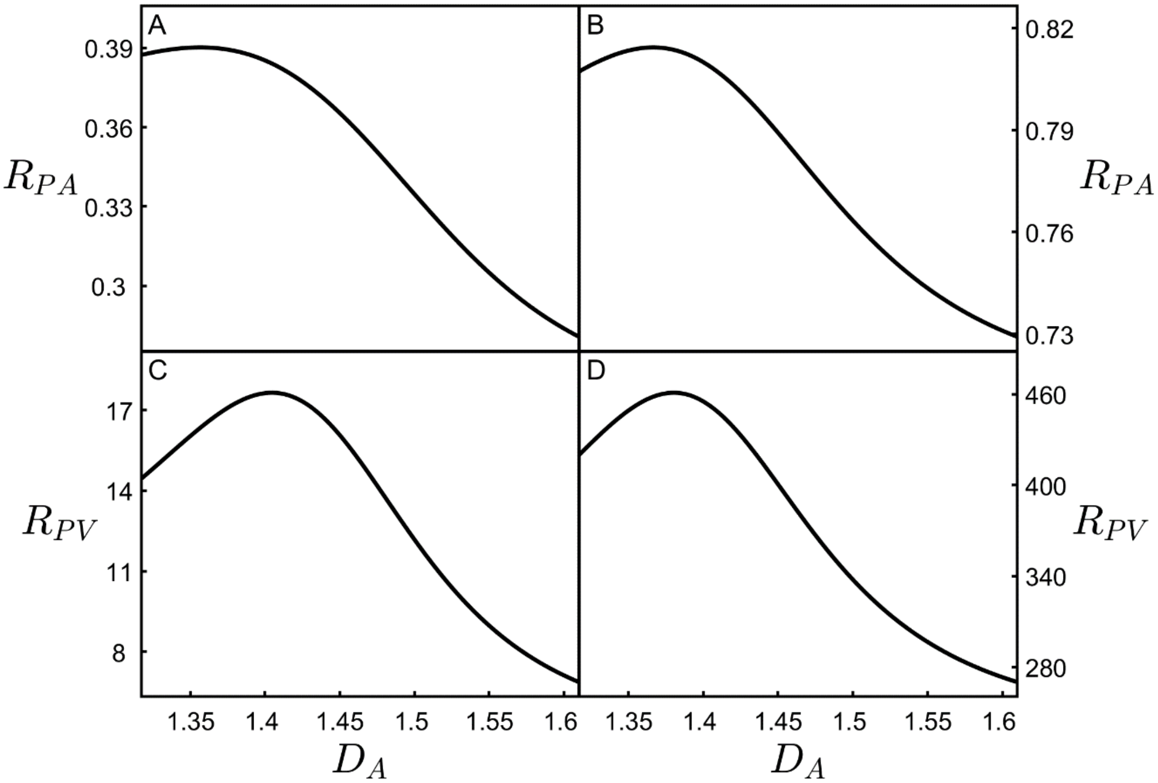

Figure 4-22. Examining the relationship between functionality optimization and arbor fractal dimension. The ratio, R_{PA}, of the derivatives of P/A_b and A_s/A_b for the neurons (**A**) and H-Trees (**B**), along with the ratio, R_{PV}, of the derivatives of P/A_b and V_m/V_b for the neurons (**C**) and H-Trees (**D**) plotted against arbor fractal dimension, D_A. The peaks of the solid curves in (**A**), (**B**), (**C**), and (**D**) occur at D_A = 1.36, 1.37, 1.40, and 1.38, respectively.

Although Eqs. 4-12 and 4-13 seem to be effective in quantifying the connectivity-cost optimization, another approach would be to consider if the neurons are sensitive to the rate of change of the ratios of connectivity density with operating cost

$$R^*_{PA} = \frac{d}{dD_A}\left(\frac{\frac{P}{A_b}}{\frac{A_s}{A_b}}\right) = \frac{d}{dD_A}\left(\frac{P}{A_s}\right) \qquad \text{(Eq. 4-14)}$$

and with building cost

$$R^*{}_{PV} = \frac{d}{dD_A}\left(\frac{\frac{P}{A_b}}{\frac{V_m}{V_b}}\right). \qquad \text{(Eq. 4-15)}$$

Adopting this approach, $R^*{}_{PA}$ reduces solely to the rate of change of connectivity efficiency, which as mentioned previously does not capture the ‘increased surface area effect’ (charted by A_s/A_b) shown in Fig. 4-21C. As seen in Fig. 4-23A, $R^*{}_{PA}$ does not contain a peak close to the natural neurons’ mean D_A value of 1.42, suggesting that the approach of using a derivative of the ratio of P/A_b to A_s/A_b is not effective because it ignores the importance of connectivity density. $R^*{}_{PV}$ similarly does not contain a peak. Although Eq. 4-15 doesn’t cancel component functional parameters in the way Eq. 4-14 does, it is also ineffective at predicting the behavior of the natural neurons, suggesting that the derivative of the ratio of P/A_b to V_m/V_b does not directly influence the optimization process. It will be interesting to see if the results of future research examining a broad range of neuron types find that R_{PA} and R_{PV} (as defined by Eqs. 4-12 and 4-13) remain effective at predicting the peak in the histogram of a neuron’s natural D_A value.

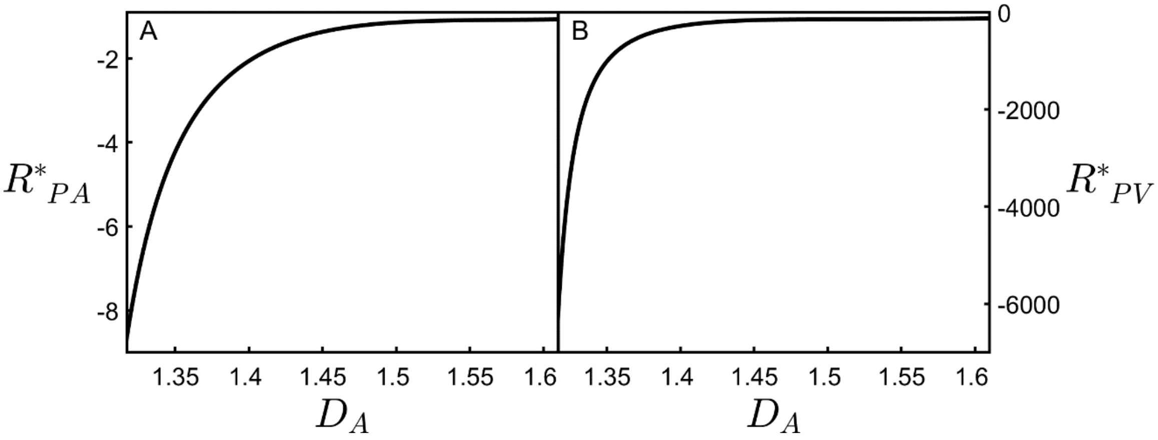

Figure 4-23. Examining alternative definitions of functionality optimization. (**A**) Plot of $R^*{}_{PA}$, the derivative of the ratio of P/A_b to A_s/A_b against arbor fractal dimension, D_A. (**B**) Plot of $R^*{}_{PV}$, the derivative of the ratio of P/A_b to V_m/V_b against arbor fractal dimension, D_A. Both (**A**) and (**B**) apply to the neuron arbors.

Having gained an understanding of the relationship between D_A and connectivity-cost optimization, it is informative to determine whether similar behaviors exist for branch fractal dimension, D_{BC}. Examining the relationship between the fractal properties of an arbor and its constituent branches is a clear first step towards this. Figure 4-24A plots D_A against mean branch fractal dimension, $\langle D_{BC} \rangle$, for seven values of the angle multiplier, α. While D_A is seen to rise as the arbors deviate away from the natural condition where $\alpha = 1$ (as expected from the results of Fig. 4-20), the same is not true for $\langle D_{BC} \rangle$, which increases or decreases as together with α. This difference stems from the fact that the fractality of a neuron's arbor depends on an interplay between its branches and the gaps between them. As there are no gaps present when examining an individual branch, straightening out the path taken by the branch can only cause it to approach the linear Euclidean condition. However, even though this different behavior exists between the arbor and its branches, the specific dependence of D_A on $\langle D_{BC} \rangle$ given in Fig. 4-24A can be used to investigate the relationship between $\langle D_{BC} \rangle$ and connectivity-cost optimization. Figure 4-24B shows a plot R_{PA} and R_{PV} against $\langle D_{BC} \rangle$ for seven values of α. This plot was generated by first using Fig. 4-24A to convert the $\langle D_{BC} \rangle$ values for each α value to their associated D_A values and then using Fig. 4-22A and C to convert these D_A values to their respective R_{PA} and R_{PV} values. As shown by the falling R_{PA} and R_{PV} values, the balance between connectivity and cost deteriorates as $\langle D_{BC} \rangle$ and D_A move away from their natural values.

Figure 4-24 emphasizes that even for neuron arbors composed of dendrites with very mild fractality (characterized by low dimensions close to those of Euclidean straight lines and charted over just one order of magnitude), $\langle D_{BC} \rangle$ nevertheless serves as a key parameter for charting the interplay between the arbor branches and their gaps, resulting in a systematic

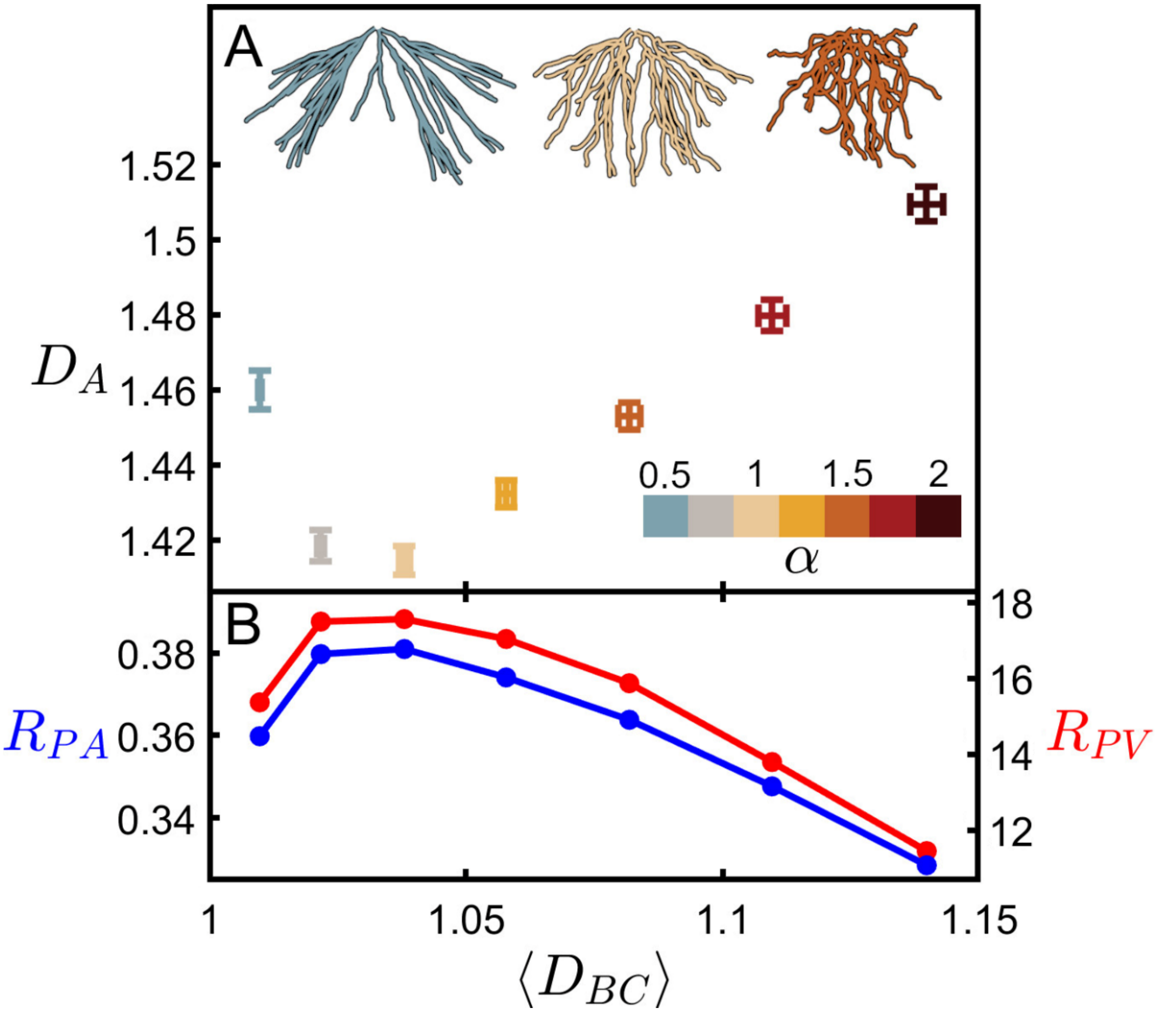

Figure 4-24. The impact of changing branch fractal dimension on arbor fractal dimension and functionality optimization. (**A**) Arbor fractal dimension, D_A, plotted against the mean coastline fractal dimension, $\langle D_{BC} \rangle$, for seven values of α as indicated by the lower-right color bar. The shown data represent the mean of D_A and $\langle D_{BC} \rangle$ across all arbors for each α value, with the error bars indicating the standard error from the mean. The three upper insets show an example neuron's arbor imaged from the same viewpoint for three values of α, as indicated by the color of the arbor. (**B**) The connectivity-cost optimization curves, R_{PA} (blue) and R_{PV} (red), plotted against $\langle D_{BC} \rangle$.

shift from natural to non-optimal D_A values. The asymmetry of the curves in Figure 4-24 draw attention to the sensitivity of neuron behavior to changes in their $\langle D_{BC} \rangle$ values. Distortions that increase the dendrites' weaving and forking angles lead to small increases in D_A compared to the sharper rises observed for distortions that reduce these angles. In particular, arbors featuring dendrites close to the Euclidean condition are highly sensitive to distortions. For example, the small reduction in $\langle D_{BC} \rangle$ from 1.02 ($\alpha = 0.75$) to 1.01 ($\alpha = 0.5$) is accompanied by an increase in D_A from 1.42 ($\alpha = 0.75$) to 1.46 ($\alpha = 0.5$) – relative to the dendrites, the arbor's dimension increases approximately fourfold. The associated reductions in R_{PA} and R_{PV} values exhibit similar sensitivities to D_{BC}.

CHAPTER V

CONCLUSIONS AND FUTURE EXPERIMENTS

Artificial electrode interfaces that are chemically and physically compatible with biological systems hold great promise for fundamental and applied research and could lead to significant advances in medical implants. Because of their role as the body's electrical wiring, neurons and the glial cells that serve as their life-support system have been a major focus of this field of research. In chapter III of this dissertation, the impact that variations in surface topography have on the morphology of neuronal and glial networks was studied using patterned VACNTs grown on a smooth SiO_2 surface. Specifically, *in vitro* co-cultures of mouse retinal neurons and glia were examined for a range of Euclidean and fractal electrode geometries. While the VACNT-SiO_2 material system was shown to have a powerful ability to 'herd' neurons onto the VACNTs and glia onto the SiO_2, subtleties in the behavior of the neurons and glia on the Euclidean and fractal electrodes were identified, demonstrating the importance of electrode geometry in combination with electrode material properties.

In particular, 'cluster' neuronal networks on the SiO_2 gaps surrounding the VACNT electrodes qualitatively displayed some of the structural characteristics of small-world networks: the neurons clustered into large groups of somas typically supported by glial coverage and connected to other clusters via bundled processes. This network was connected to neurons on the VACNTs through a 'boundary' region featuring a large density of smaller neuron clusters and processes close to the VACNT electrodes. The SiO_2 surfaces far away from any VACNTs were dominated by 'desert' regions characterized by sparse neuron clustering, limited process growth, and low glial coverage. Within the range of gap widths examined here (25 µm - 100 µm), the Euclidean Rows electrode design was in general found to be dominated by boundary regions. The 2-5 and 2-6 Fractal designs, which feature the most constricted gaps amongst the Fractal designs, were similarly dominated by boundary regions. In comparison, the 1.1-4 Fractal design's sparse electrode and very large SiO_2 gaps were dominated by desert regions. While the remaining 1.5-4 and 2-4 Fractal designs contained both cluster and boundary regions, they were in general dominated by cluster regions. For the group of fractal H-Tree electrode designs, it was accordingly found that electrodes characterized by a mid-to-high fractal dimension and repeating level optimized the cell response by inducing large glial coverage in the gaps and fueling the formation of cluster regions that were connected to nearby boundary regions which themselves connected to the dense network of neuron processes on the VACNT electrode surface. Lastly, the Grid electrode design was found to be boundary dominated and performed well at accumulating neurons on the VACNT surfaces. This was likely due to the close proximity of the neurons in the Grid's chambers to the VACNT sidewalls. However, the relative lack of nearby glia for the neurons on the Grid's VACNTs is expected to negatively impact their long-term survival and electrical activity[196].

It is hoped that the approach of studying the interaction of these regions can be used to inform other future electrode designs, along with other material systems and chemical treatments. For example, whereas the Euclidean Rows and Grid designs examined here closely matched the smallest scales of the Fractal designs, future experiments could consider wider gaps (or in the case of the Grid design a larger chamber size). The model presented here predicts that increasing the gap or chamber width enough to induce a significant increase in glial coverage for the Euclidean Rows and Grid designs will ultimately have a negative impact. Due to the single-scaled, disconnected character of the SiO_2 gaps in the Euclidean

Rows and Grid designs, an increase in the gap or chamber width sufficient to encourage more glial coverage will likely come at a detriment to the neurons, stemming from an overall decrease in the proximity of the electrode surfaces to the clusters of neurons in the surrounding SiO_2 gaps. This prediction is further suggested by the Grid design's significantly larger N_{CNT} and N_{Si} values when compared to the 2-5 Fractal design, which has a lower proximity between the electrode surfaces and clusters of neurons in the surrounding SiO_2 gaps than the Grid design.

Although the fundamental ability to herd neurons and glia has been demonstrated here, future studies will need to confirm the benefits of this herding in terms of neuronal health and electrical stimulation. Considering health consequences, the behavior of the neurons and glia on the electrode designs examined here appeared to operate within a regime in which the increased presence of nearby glia correlated with enhanced growth of neuron processes on the electrodes, pointing to a 'the more glia the better' approach for neuronal health. It should be cautioned that this operational regime is not expected to be universal and that upper limits of glial accumulation might need to be identified and quantified for some systems. In particular, although the *in vitro* studies presented here represent a simple, controlled model for *in vivo* behavior[233], differences between these environments will need to be accommodated in the long-term. For example, *in vivo* experiments will involve electrode interactions with three-dimensional, structurally intact tissue. Glia will then be present in both the electrode layer and in the tissue above the electrode. As such, it would be beneficial to guide the glia in the space above the electrode away from its surface and into its surrounding gaps to allow more neurons to be attracted towards the surface of the electrode. This increased proximity between the neurons and the electrode would thereby allow for easier electrical stimulation of the neurons.

Based on the results presented here, it is reasonable to hypothesize that there exists an optimized combination of electrode material and geometry that will maximize the positive responses of different cell types within the tissue interacting with the electrode. As an example, the 2-5 Fractal electrode design can be modified through branch elimination or rotation to remove barriers in the electrode's central gap region while connecting the pattern to a boundary rectangle to maintain a fully connected electrode. Such strategies increase the connectedness and accessibility of the SiO_2 gaps for the glia while keeping their proximity to the VACNT branches approximately the same (Fig. 5-1A and B). In contrast to these positive modifications, introducing extra branches into the 2-5 Fractal design to increase proximity will likely lead to negative consequences, in particular creating closed SiO_2 regions that reduce the connectedness of the geometry (Fig. 5-1C). In the long term, an optimized combination of material and geometry could be used to maximize the efficiency of implants for neuronal recording and stimulation.

Another useful direction for future studies is to define the cell characteristics of the boundary, cluster, and desert regions more precisely to allow their areas, their locations, and therefore their contributions to herding to be quantified. This includes analyzing the neuronal network topography (such as clustering coefficient and shortest pathlengths) of the cluster regions to potentially confirm their small-world characteristics[234,235]. While the experiments detailed in chapter III quantified neuron process length and glial coverage as morphological measures of the cells, future studies would benefit from considering refined morphological characteristics using more specific cell markers and additional measures such as Sholl analysis. This would allow for distinguishing between subcategories of cells, for example,

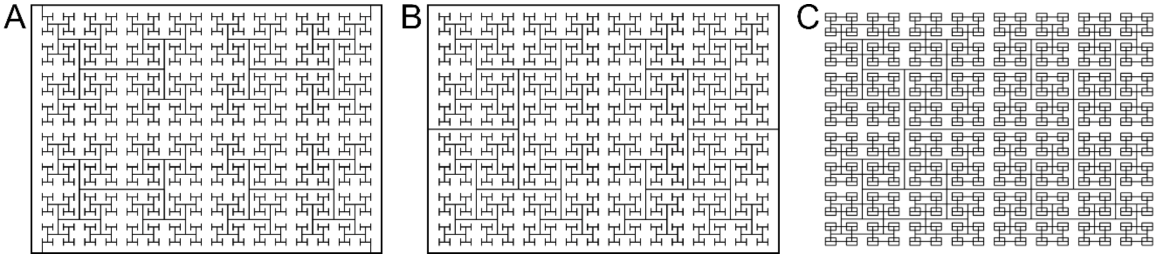

Figure 5-1. Examples of improved and worsened electrode geometries. (**A**, **B**) Improved electrode based on the 2-5 Fractal design enclosed within a rectangular boundary. For design (**A**), the first-order H has been removed from the tree and the four outer corners have been connected to the rectangular boundary. For design (**B**), the 2-5 Fractal design has been cut in half through the zeroth-order branch segment. Each half was then rotated through 180° and attached to the boundary. In this second design, the H-Tree branches spread from the boundary inwards rather than spreading out from the origin. By removing the branch occupying the central section of the design, both the (**A**) and (**B**) modifications create a completely connected SiO_2 gap region while keeping the proximity of the gaps to the electrodes roughly comparable to the original 2-5 Fractal design. (**C**) Worsened 2-5 Fractal design in which extra lines connect the top-left and top-right endpoints as well as the bottom-left and bottom-right endpoints within each H at every repeating level of the fractal. This modification increases the proximity between the gaps and the electrodes but decreases the gap connectedness drastically.

different glial cell types (Müller cells/astrocytes and microglia)[181] and different states of glial activation as well as different neuronal subpopulations such as bipolar and ganglion cells[236]. This will aid in quantifying differences in cell morphology between the boundary, cluster, and desert regions, and so allow them to be differentiated more accurately. Given the different functional roles of, for example, Müller cells/astrocytes and microglia, these distinguishing markers will also allow a greater understanding of the impact of electrode geometry on glial cell activation.

Whereas the morphology of the network of neurons and glia was the focus of chapter III, future studies targeting applications may benefit from analyzing the adhesive strength of the neuronal networks along with their electrical properties. Detection of cell-electrode anchor points by immunostaining (e.g. vinculin and focal adhesion kinase)[237,238] will provide both a better understanding of the process of network formation and a robust assessment of its attachment to the electrodes. Future studies examining the electrical properties of the networks may use calcium imaging and microelectrode array (MEA) systems to confirm neuronal stimulation. Such studies will help clarify the impact that the clustering and bundling observed here have on the connectivity efficiency associated with small-world networks[239,240].

Finally, the *in vitro* study examined here deliberately employed large-scale fractal electrodes to manipulate networks of cells. Practically, these large sizes are more applicable to brain stimulation techniques[10] than to retinal implants, which require individual electrodes to be near 20 μm in width in order to restore visual acuity to a level above legal blindness[241,242]. In future studies working towards the goal of improving the design of retinal implant electrodes, the electrode sizes examined here would need to be shrunk significantly. This reduction in size would of course have an impact on how the neurons interact with the electrode. Instead of manipulating the morphology of neuronal networks at the large scale, electrode designs on the scale of 20 μm would manipulate the morphology of individual neurons. Although the H-Tree electrode designs were shown to influence herding, their shapes are radically different to those of individual neurons (in particular, their straight lines and 90^o turns are strikingly unnatural in comparison to the branches of an individual neuron). Should the 'fractal resonance' hypothesis proposed in chapter I of this dissertation be correct, matching the electrode's geometry to the precise fractal characteristics of the neurons they interact with would result in increased neuron-electrode connectivity and allow the neuron to maintain a structure associated with its natural functionality.

Aiming towards the goal of testing the 'fractal resonance' hypothesis, the experiments detailed in chapter IV examined the precise fractal characteristics of the arbors and individual branches of pyramidal neurons from the CA1 region of the rat hippocampus and demonstrated that these fractal characteristics are tied to the neuron's functionality. First, to clarify the origin of the neurons' fractality, the relationship between the fractal scaling properties of a neuron's individual branches and its arbor as a whole was investigated by employing methods for measuring the fractal dimensions of both the neuron's arbor, D_A, and its branches, D_B. It was found that the underlying fractal scaling properties of a neuron's arbor arise from a combination of variations in the weave angle, forking angle, and length scaling distributions of its branches, highlighting the difference between the statistical self-similarity displayed by neurons and the 'perfect' self-similarity displayed by exact, mathematical fractals like H-Trees and Koch curves. Interestingly, though the fractal behavior of the neurons' branches was shown to be very mild (characterized by D_B values close to 1), it was found that the branches exhibit the same fractal behavior irrespective of the length of the branch within the measurable fractal range. Additionally, as the branches of an arbor spread out in space, the resulting arbor properties depend on two embedded fractal patterns – the branches and the gaps forming between them. This spatial relationship generates a much larger complexity for the arbors than that of their individual branches.

As noted at the end of the Fractal Analysis section within chapter II of this dissertation, the fractality of physical systems has seen a fair amount of debate that has stemmed from two main factors. Firstly, physical fractals are inherently limited in the ranges over which they display scale-invariance. Secondly, Benoit Mandelbrot's definition of fractal did not include a scaling range requirement. Surveys looking across many different examples of physical fractals have found that their scaling ranges are typically between 0.5 and 2 orders of magnitude, with the most common scaling range being 1.3 orders of magnitude[101,102]. In addition to discussing scaling ranges, previous debates that centered around the appropriateness of labelling physical systems as fractal have focused on two important questions: 1) Does fractal analysis provide a useful description of the system? 2) Does fractal analysis allow one to correlate some relevant property of the system to its structure? Many previous studies have employed fractal dimension as a useful characterization of the complexity of neuron arbors[17,21,89–91,93–96] and in doing so addressed the first question. However, the second question has gone largely unaddressed.

Within this dissertation, multiple fractal analyses have been applied to neurons to better understand the origin of the fractal properties of both their arbors and branches. Each of these analyses required a scaling range of at least one order of magnitude (which falls within the typical range measured for physical fractals) and found the arbors' mean D_A value to be 1.42, while their branches' mean D_B value was 1.04. Even though this notable difference exists between the fractal dimension of the arbors and branches, they both were found to relate to the neuron's ability to optimally balance the benefits of connectivity with building and operational costs (see Figs. 4-22 and 4-24). These results effectively address the second question. As such, while the analyses of the arbors and branches of the neurons examined within this dissertation have demonstrated limited-range fractal scaling, these analyses have proven useful in better understanding the morphology and functionality of the neurons, bolstering the appropriateness of labelling the arbor and branches of these neurons as fractal. However, it should be emphasized that the fractal dimension of the neuron branches are very close to 1, and so future work should be done test the degree to which these slightly non-linear branches behave differently from perfectly straight branches.

Examining the relationship between the fractal properties of a neuron's arbor and its branches further, it was found that distorted neuron models generated by altering the natural weaving and forking behavior of the neuron negatively impacted the branches' inherent, self-avoiding behavior. Regardless of whether the weaving and forking behavior was reduced or amplified, the distorted neuron models displayed an increase in D_A. For the neurons examined here, distortions that reduced the fractal weave of their branches, bringing them nearer to the Euclidean condition of straight lines (given by $D_B = 1$), induced relatively large changes in the fractal characteristics of their arbors. Based on this observation, it is anticipated that neuron types with naturally occurring low D_B values that are distorted in a manner that reduces their weaving and forking behavior will experience large changes in their arbor fractal characteristics. This however assumes a similar arbor density to the neurons examined here - this behavior may not be seen for sparsely branching neurons. It is also intriguing to consider neurons with large naturally occurring D_B values and examine whether distortions through increases in their weave and forking angles would experience a similar sensitivity to D_B. It is hoped that future studies across different neuron types will investigate these behaviors.

One inevitable but useful property associated with measurements of D_A and D_B is that they are sensitive to how all three branch parameters (weave angle, forking angle, and branch length) impact a neuron's morphology. Therefore, they can be related to more traditional parameters used to study specific consequences of the neuron's complexity. This was highlighted by comparisons between D_B and tortuosity, T. Whereas the method of measuring T employed here can be used to quantify the weave of an individual branch measured at a specific size scale, D_B captures a more comprehensive picture by accounting for the weave's power-law growth in tortuosity across increasingly large scales. This was demonstrated by deriving the mathematical relationship between branch tortuosity and a traditional measure of fractal scaling and using measurements of the neurons' branches to confirm the agreement between the two associated dimensions, D_{BT} and D_{BC}.

Having clarified the origin of the neurons' fractal characteristics, relationships between them and the functionality of the neurons were then investigated. Ultimately, it was demonstrated that the fractal scaling of the neurons' arbors, though limited in range, provides a morphology that efficiently establishes connections with other neurons while balancing the building and operating costs of their arbors. As such, the neurons' natural distribution of D_A values was found to occupy a range that provides most of the neurons with an optimal balance between connectivity and cost. Additionally, distorted neuron models with a forking and weaving behavior that deviates away from the natural (i.e. undistorted) condition displayed a deterioration in this optimal balance. It should be emphasized that many physical fractals are also limited in their scaling range[102], demonstrating the effectiveness of fractal-like behavior for optimizing essential processes ranging from oxygen transfer within the lungs[57], to light collection by trees[56], to connecting neuronal networks within the brain[58].

Based on this connectivity-cost optimization model, it is expected that different neuron types adopt different D_A values depending on the relative importance of connectivity and cost. Neurons with a greater need for connectivity are expected to optimize around higher D_A. For example, Purkinje neurons, characterized by a D_A value of approximately 1.8[17], feature planar dendritic arbors that are nearly space-filing, with the goal of ensuring thousands of synaptic connections with the axons of granule cells that project perpendicularly through the Purkinje neuron's arbor.

Future studies may also be able to apply this connectivity-cost optimization model to identify neurons associated with a pathological condition. For example, neurons impacted by Alzheimer's disease might have their fractal optimization altered. This may explain previous observations of Alzheimer's disease relating to changes in the scaling behavior of neurons[243]. In an initial attempt to test this hypothesis, a study comparing the impact that lesions in the anterior thalamic nucleus of rats had on the optimization of hippocampal CA1 pyramidal neurons was conducted[244]. The results of this study revealed no significant difference between the D_A value of neurons from lesioned and non-lesioned rats, suggesting that any morphological changes induced by lesions in the anterior thalamic nuclei are too small to be detected by fractal analysis of the neurons' arbors. Similarly, although the neurons from both groups of rats did display peaks in their optimization curves, no difference was found between the optimal D_A values extracted from these curves for the two groups of rats.

Another promising direction for future studies applying this connectivity-cost optimization model is to automate the analysis techniques and apply them to broad datasets of publicly available neuron reconstructions. In doing so, the specific fractal optimization of many different neuron types can be investigated. Working towards this goal, preliminary work has already shown the effectiveness of the model by applying modified versions of the techniques detailed in chapter IV to a dataset of mouse retinal bipolar neurons[245] publicly available on NeuroMorpho.Org[246]. The results of these preliminary analyses are shown in Figure 5-2. Ultimately, the connectivity-cost optimization curve (as measured by R_{PV}, Figure 5-2C) associated with these retinal bipolar neurons displays a peak within the range of the neurons' natural distribution of D_A (Figure 5-2D) values. Interestingly, the optimal D_A value associated with the peak in R_{PV} occurs at a slightly lower D_A value than the peak in the neurons' D_A distribution. This suggests that the functionality of retinal bipolar neurons likely requires an arbor that deviates slightly from the optimal condition, in favor of increased connectivity.

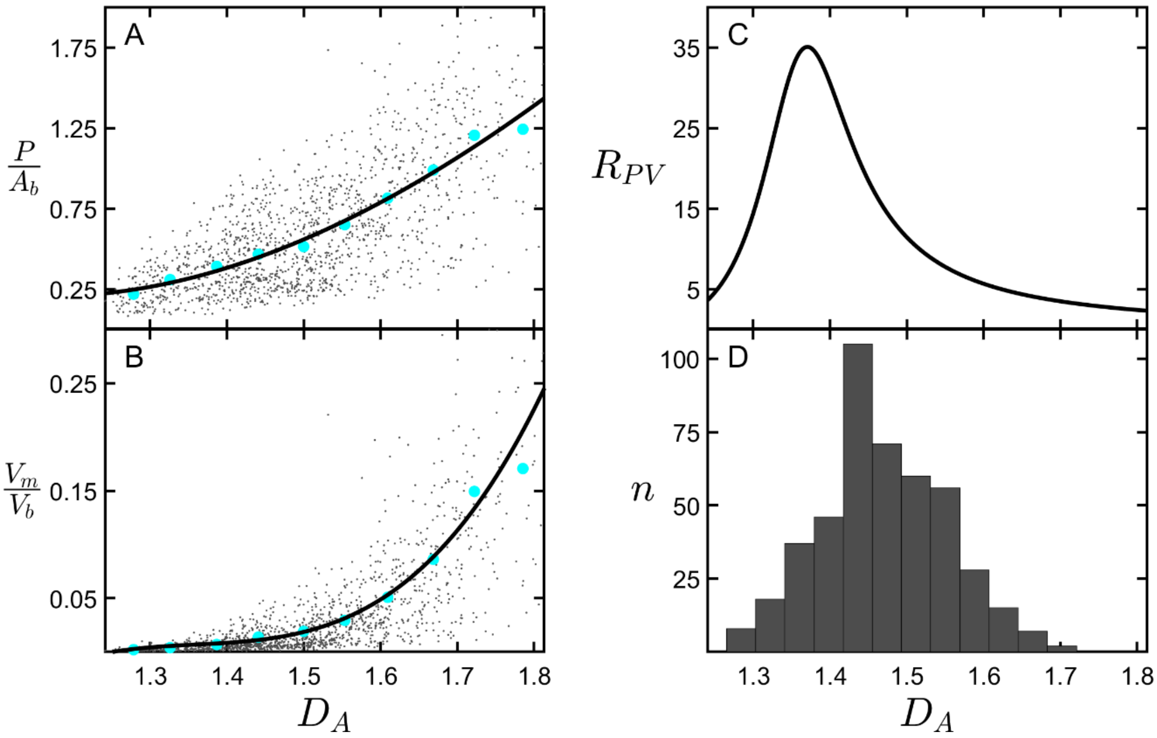

Figure 5-2. Preliminary results of the connectivity-cost optimization model applied to retinal bipolar neurons. The functional parameters P/A_b (**A**) and V_m/V_b (**B**) plotted against arbor fractal dimension, D_A. (**C**) The connectivity-cost optimization curve, R_{PV}, plotted against D_A. (**D**) The distribution of the neurons' natural D_A values.

Returning to the 'fractal resonance' hypothesis, these preliminary results on retinal bipolar neurons indicate that the fractal characteristics of these neurons are naturally suited to balance connectivity and cost. This has significant implications with respect to the design of the electrode interface of retinal implants. Should the interactions of retinal neurons with the electrode interface cause their morphology to deviate away from the naturally optimized condition, it is likely that there will be direct negative consequences regarding the functionality of the connecting neurons. However, designing the electrode to match the fractal characteristics of the neurons, thereby allowing it to maintain a naturally optimized morphology, will likely result in increased neuron-electrode connectivity and a preservation of the neurons' natural functionality.

REFERENCES CITED

1. Lewis, P. M. & Rosenfeld, J. V. Electrical stimulation of the brain and the development of cortical visual prostheses: An historical perspective. *Brain Research* **1630**, 208–224 (2016).

2. Jang, J. *et al.* Implantation of electronic visual prosthesis for blindness restoration. *Opt. Mater. Express, OME* **9**, 3878–3894 (2019).

3. Chenais, N. A. L., Airaghi Leccardi, M. J. I. & Ghezzi, D. Photovoltaic retinal prosthesis restores high-resolution responses to single-pixel stimulation in blind retinas. *Commun Mater* **2**, 1–16 (2021).

4. Prévot, P.-H. *et al.* Behavioural responses to a photovoltaic subretinal prosthesis implanted in non-human primates. *Nature Biomedical Engineering* **4**, 172–180 (2020).

5. Tong, W., Meffin, H., Garrett, D. J. & Ibbotson, M. R. Stimulation Strategies for Improving the Resolution of Retinal Prostheses. *Frontiers in Neuroscience* **14**, 262 (2020).

6. Lorach, H. *et al.* Photovoltaic restoration of sight with high visual acuity. *Nature Medicine* **21**, 476–482 (2015).

7. Palanker, D., Le Mer, Y., Mohand-Said, S., Muqit, M. & Sahel, J. A. Photovoltaic Restoration of Central Vision in Atrophic Age-Related Macular Degeneration. *Ophthalmology* **127**, 1097–1104 (2020).

8. Palanker, D., Le Mer, Y., Mohand-Said, S. & Sahel, J. A. Simultaneous perception of prosthetic and natural vision in AMD patients. *Nat Commun* **13**, 513 (2022).

9. Edwards, T. L. *et al.* Assessment of the Electronic Retinal Implant Alpha AMS in Restoring Vision to Blind Patients with End-Stage Retinitis Pigmentosa. *Ophthalmology* **125**, 432–443 (2018).

10. Hariz, M. My 25 Stimulating Years with DBS in Parkinson's Disease. *Journal of Parkinson's Disease* **7**, S33–S41 (2017).

11. Von Bartheld, C. S., Bahney, J. & Herculano-Houzel, S. The search for true numbers of neurons and glial cells in the human brain: A review of 150 years of cell counting. *Journal of Comparative Neurology* **524**, 3865–3895 (2016).

12. Fan, X. & Agid, Y. At the Origin of the History of Glia. *Neuroscience* **385**, 255–271 (2018).

13. Zhang, Y. & Barres, B. A. Astrocyte heterogeneity: an underappreciated topic in neurobiology. *Current Opinion in Neurobiology* **20**, 588–594 (2010).

14. Jelinek, H. F. & Fernandez, E. Neurons and fractals: how reliable and useful are calculations of fractal dimensions? *Journal of neuroscience methods* **81**, 9–18 (1998).

15. Mandelbrot, B. B. *Fractals: Form, Chance, and Dimension*. (WH Freeman, 1977).

16. Mandelbrot, B. & Pignoni, R. *The Fractal Geometry of Nature*. (WH Freeman, 1983).

17. Takeda, T., Ishikawa, A., Ohtomo, K., Kobayashi, Y. & Matsuoka, T. Fractal dimension of dendritic tree of cerebellar Purkinje cell during onto- and phylogenetic development. *Neuroscience Research* **13**, 19–31 (1992).

18. Neale, E. A., Bowers, L. M. & Smith Jr., T. G. Early dendrite development in spinal cord cell cultures: A quantitative study. *Journal of Neuroscience Research* **34**, 54–66 (1993).

19. Kniffki, K.-D., Pawlak, M. & Vahle-Hinz, C. Scaling behavior of the dendritic branches of thalamic neurons. *Fractals* **01**, 171–178 (1993).

20. Jelinek, H. F. & Elston, G. N. Dendritic branching of pyramidal cells in the visual cortex of the nocturnal owl monkey: a fractal analysis. *Fractals* **11**, 391–396 (2003).

21. Milošević, N. T. & Ristanović, D. Fractality of dendritic arborization of spinal cord neurons. *Neuroscience Letters* **396**, 172–176 (2006).

22. Jelinek, H. F., Ristanović, D. & Milošević, N. T. The morphology and classification of α ganglion cells in the rat retinae: a fractal analysis study. *J Neurosci Methods* **201**, 281–287 (2011).

23. Crawford, J. W. & Young, I. M. A multiple scaled fractal tree. *Journal of Theoretical Biology* **145**, 199–206 (1990).

24. Cieplak, M. *et al.* Models of Fractal River Basins. *Journal of Statistical Physics* **91**, 1–15 (1998).

25. Mandelbrot, B. How Long Is the Coast of Britain? Statistical Self-Similarity and Fractional Dimension. *Science* **156**, 636–638 (1967).

26. Wilson, T. H. & Dominic, J. Fractal interrelationships between topography and structure. *Earth Surface Processes and Landforms* **23**, 509–525 (1998).

27. Lovejoy, S. Area-Perimeter Relation for Rain and Cloud Areas. *Science* **216**, 185–187 (1982).

28. Tsonis, A. A. & Elsner, J. B. Fractal Characterization and Simulation of Lightning. *Beiträge zur Physik der Atmosphäre* **60**, 187–192 (1987).

29. Nittmann, J. & Stanley, H. E. Non-deterministic approach to anisotropic growth patterns with continuously tunable morphology: the fractal properties of some real snowflakes. *J. Phys. A: Math. Gen.* **20**, L1185 (1987).

30. Li, J. *et al.* Scale-invariant magnetic textures in the strongly correlated oxide NdNiO3. *Nat Commun* **10**, 4568 (2019).

31. Hallén, J. N., Grigera, S. A., Tennant, D. A., Castelnovo, C. & Moessner, R. Dynamical fractal and anomalous noise in a clean magnetic crystal. *Science* **378**, 1218–1221 (2022).

32. Kumar, S., Saha, D., Kohlbrecher, J. & Aswal, V. K. Interplay of interactions for different pathways of the fractal aggregation of nanoparticles. *Chemical Physics Letters* **803**, 139808 (2022).

33. Lieberman-Aiden, E. *et al.* Comprehensive mapping of long-range interactions reveals folding principles of the human genome. *Science* **326**, 289–293 (2009).

34. Ghorbani, M., Jonckheere, E. A. & Bogdan, P. Gene Expression Is Not Random: Scaling, Long-Range Cross-Dependence, and Fractal Characteristics of Gene Regulatory Networks. *Frontiers in Physiology* **9**, (2018).

35. Liebovitch, L. S., Scheurle, D., Rusek, M. & Zochowski, M. Fractal Methods to Analyze Ion Channel Kinetics. *Methods* **24**, 359–375 (2001).

36. Rudge, T. J., Federici, F., Steiner, P. J., Kan, A. & Haseloff, J. Cell Polarity-Driven Instability Generates Self-Organized, Fractal Patterning of Cell Layers. *ACS Synth. Biol.* **2**, 705–714 (2013).

37. Masters, B. R. Fractal Analysis of the Vascular Tree in the Human Retina. *Annual Review of Biomedical Engineering* **6**, 427–452 (2004).

38. Essey, M. & Maina, J. N. Fractal analysis of concurrently prepared latex rubber casts of the bronchial and vascular systems of the human lung. *Open Biology* **10**, 190249 (2020).

39. Ivanov, P. C. *et al.* Multifractality in human heartbeat dynamics. *Nature* **399**, 461–465 (1999).

40. Rasouli, G. *et al.* Fractal characteristics of human parkinsonian neuronal spike trains. *Neuroscience* **139**, 1153–1158 (2006).

41. Liu, J. Z., Zhang, L. D. & Yue, G. H. Fractal Dimension in Human Cerebellum Measured by Magnetic Resonance Imaging. *Biophysical Journal* **85**, 4041–4046 (2003).

42. Im, K. *et al.* Fractal dimension in human cortical surface: Multiple regression analysis with cortical thickness, sulcal depth, and folding area. *Hum Brain Mapp* **27**, 994–1003 (2006).

43. Varley, T. F. *et al.* Fractal dimension of cortical functional connectivity networks & severity of disorders of consciousness. *PLOS ONE* **15**, e0223812 (2020).

44. Bartumeus, F. Lévy processes in animal movement: an evolutionary hypothesis. *Fractals* **15**, 151–162 (2007).

45. SIVAKUMAR, B. Fractal analysis of rainfall observed in two different climatic regions. *Hydrological Sciences Journal* **45**, 727–738 (2000).

46. Balkissoon, S., Fox, N. & Lupo, A. Fractal characteristics of tall tower wind speeds in Missouri. *Renewable Energy* **154**, 1346–1356 (2020).

47. Cabrera-Brito, L. *et al.* Fractal Analysis of Deep Ocean Current Speed Time Series. *Journal of Atmospheric and Oceanic Technology* **34**, 817–827 (2017).

48. Li, J. & Ostoja-Starzewski, M. Edges of Saturn’s rings are fractal. *Springerplus* **4**, 158 (2015).

49. Kim, Y. *et al.* Structure of the Interstellar Medium around Cas A. *ApJ* **678**, 287 (2008).

50. Elia, D. *et al.* Multifractal analysis of the interstellar medium: first application to Hi-GAL observations. *Monthly Notices of the Royal Astronomical Society* **481**, 509–532 (2018).

51. Gaite, J. Fractal analysis of the large-scale stellar mass distribution in the Sloan Digital Sky Survey. *J. Cosmol. Astropart. Phys.* **2018**, 010 (2018).

52. Hentschel, H. G. E. & Procaccia, I. Relative diffusion in turbulent media: The fractal dimension of clouds. *Phys. Rev. A* **29**, 1461–1470 (1984).

53. Yahia, H. *et al.* Description of turbulent dynamics in the interstellar medium: multifractal-microcanonical analysis - I. Application to Herschel observations of the Musca filament. *A&A* **649**, A33 (2021).

54. Rinaldo, A., Rigon, R., Banavar, J. R., Maritan, A. & Rodriguez-Iturbe, I. Evolution and selection of river networks: Statics, dynamics, and complexity. *Proceedings of the National Academy of Sciences* **111**, 2417–2424 (2014).

55. Sapoval, B., Baldassarri, A. & Gabrielli, A. Self-Stabilized Fractality of Seacoasts through Damped Erosion. *Phys. Rev. Lett.* **93**, 098501 (2004).

56. Seidel, D. *et al.* How a measure of tree structural complexity relates to architectural benefit-to-cost ratio, light availability, and growth of trees. *Ecol Evol* **9**, 7134–7142 (2019).

57. Hou, C., Gheorghiu, S., Huxley, V. H. & Pfeifer, P. Reverse Engineering of Oxygen Transport in the Lung: Adaptation to Changing Demands and Resources through Space-Filling Networks. *PLoS Comput Biol* **6**, e1000902 (2010).

58. Gallos, L. K., Sigman, M. & Makse, H. A. The Conundrum of Functional Brain Networks: Small-World Efficiency or Fractal Modularity. *Front Physiol* **3**, 123 (2012).

59. Mirny, L. A. The fractal globule as a model of chromatin architecture in the cell. *Chromosome Res* **19**, 37–51 (2011).

60. Clark, P., Connolly, P., Curtis, A. S., Dow, J. A. & Wilkinson, C. D. Topographical control of cell behaviour: II. Multiple grooved substrata. *Development* **108**, 635–644 (1990).

61. Rajnicek, A., Britland, S. & McCaig, C. Contact guidance of CNS neurites on grooved quartz: influence of groove dimensions, neuronal age and cell type. *Journal of cell science* **110**, 2905–2913 (1997).

62. Smeal, R. M., Rabbitt, R., Biran, R. & Tresco, P. A. Substrate Curvature Influences the Direction of Nerve Outgrowth. *Annals of Biomedical Engineering* **33**, 376–382 (2005).

63. Goldner, J. S., Bruder, J. M., Li, G., Gazzola, D. & Hoffman-Kim, D. Neurite bridging across micropatterned grooves. *Biomaterials* **27**, 460–472 (2006).

64. Johansson, F., Carlberg, P., Danielsen, N., Montelius, L. & Kanje, M. Axonal outgrowth on nano-imprinted patterns. *Biomaterials* **27**, 1251–1258 (2006).

65. Lee, J. W. *et al.* Topographical guidance of mouse neuronal cell on SiO2 microtracks. *Sensors and Actuators B: Chemical* **128**, 252–257 (2007).

66. Khan, S. & Newaz, G. A comprehensive review of surface modification for neural cell adhesion and patterning. *Journal of Biomedical Materials Research Part A* **93A**, 1209–1224 (2010).

67. Belkaid, W. *et al.* Cellular response to micropatterned growth promoting and inhibitory substrates. *BMC Biotechnology* **13**, 86 (2013).

68. Li, W. *et al.* Large-scale Topographical Screen for Investigation of Physical Neural-Guidance Cues. *Sci Rep* **5**, 8644 (2015).

69. Piret, G., Perez, M.-T. & Prinz, C. N. Support of Neuronal Growth Over Glial Growth and Guidance of Optic Nerve Axons by Vertical Nanowire Arrays. *ACS Appl. Mater. Interfaces* **7**, 18944–18948 (2015).

70. Simitzi, C., Ranella, A. & Stratakis, E. Controlling the morphology and outgrowth of nerve and neuroglial cells: The effect of surface topography. *Acta Biomaterialia* **51**, 21–52 (2017).

71. Moslehi, S. *et al.* Physical Guidance of Cultured Retinal Neurons Using Zig-zag Surface Patterns. *American Journal of Biomedical Science & Research* **11**, 3 (2020).

72. Ramón y Cajal, S. *Texture of the Nervous System of Man and the Vertebrates*. (Springer, 1999). doi:10.1007/978-3-7091-6435-8.

73. Sanes, J. R. & Zipursky, S. L. Design Principles of Insect and Vertebrate Visual Systems. *Neuron* **66**, 15–36 (2010).

74. Masland, R. H. The Neuronal Organization of the Retina. *Neuron* **76**, 266–280 (2012).

75. Sanes, J. R. & Masland, R. H. The Types of Retinal Ganglion Cells: Current Status and Implications for Neuronal Classification. *Annual Review of Neuroscience* **38**, 221–246 (2015).

76. Andersen, P., Morris, R., Amaral, D., Bliss, T. & O'Keefe, J. *The Hippocampus Book*. (Oxford University Press, 2006).

77. Rye, C. *et al. Biology*. (OpenStax, 2016).

78. Laughlin, S. B., de Ruyter van Steveninck, R. R. & Anderson, J. C. The metabolic cost of neural information. *Nature Neuroscience* **1**, 36–41 (1998).

79. Attwell, D. & Laughlin, S. B. An energy budget for signaling in the grey matter of the brain. *J. Cereb. Blood Flow Metab.* **21**, 1133–1145 (2001).

80. Mitchison, G. & Barlow, H. B. Neuronal branching patterns and the economy of cortical wiring. *Proceedings of the Royal Society of London. Series B: Biological Sciences* **245**, 151–158 (1991).

81. Cherniak, C. Local optimization of neuron arbors. *Biol. Cybern.* **66**, 503–510 (1992).

82. Chklovskii, D. B. Synaptic Connectivity and Neuronal Morphology: Two Sides of the Same Coin. *Neuron* **43**, 609–617 (2004).

83. Rushton, W. A. H. A theory of the effects of fibre size in medullated nerve. *J Physiol* **115**, 101–122 (1951).

84. Rall, W. *et al.* Matching dendritic neuron models to experimental data. *Physiological Reviews* **72**, S159–S186 (1992).

85. Wen, Q. & Chklovskii, D. B. Segregation of the Brain into Gray and White Matter: A Design Minimizing Conduction Delays. *PLOS Computational Biology* **1**, e78 (2005).

86. Bassingthwaighte, J. B., Liebovitch, L. S. & West, B. J. *Fractal Physiology*. (Springer-Verlag, 1994).

87. Iannaccone, P. M. & Khokha, M. *Fractal Geometry in Biological Systems: An Analytical Approach*. (CRC Press, 1996).

88. The Petilla Interneuron Nomenclature Group (PING) *et al.* Petilla terminology: nomenclature of features of GABAergic interneurons of the cerebral cortex. *Nature Reviews Neuroscience* **9**, 557–568 (2008).

89. Smith Jr., T. G., Lange, G. D. & Marks, W. B. Fractal methods and results in cellular morphology — dimensions, lacunarity and multifractals. *Journal of Neuroscience Methods* **69**, 123–136 (1996).

90. Alves, S. G., Martins, M. L., Fernandes, P. A. & Pittella, JoséE. H. Fractal patterns for dendrites and axon terminals. *Physica A: Statistical Mechanics and its Applications* **232**, 51–60 (1996).

91. Wearne, S. L. *et al.* New techniques for imaging, digitization and analysis of three-dimensional neural morphology on multiple scales. *Neuroscience* **136**, 661–680 (2005).

92. Zietsch, B. & Elston, E. Fractal analysis of pyramidal cells in the visual cortex of the galago (Otolemur garnetti): Regional variation in dendritic branching patterns between visual areas. *Fractals* **13**, 83–90 (2005).

93. Rothnie, P., Kabaso, D., Hof, P. R., Henry, B. I. & Wearne, S. L. Functionally relevant measures of spatial complexity in neuronal dendritic arbors. *Journal of Theoretical Biology* **238**, 505–526 (2006).

94. Caserta, F. *et al.* Determination of fractal dimension of physiologically characterized neurons in two and three dimensions. *J. Neurosci. Methods* **56**, 133–144 (1995).

95. Werner, G. Fractals in the Nervous System: Conceptual Implications for Theoretical Neuroscience. *Front Physiol* **1**, (2010).

96. Di Ieva, A., Grizzi, F., Jelinek, H., Pellionisz, A. J. & Losa, G. A. Fractals in the Neurosciences, Part I: General Principles and Basic Neurosciences. *Neuroscientist* **20**, 403–417 (2014).

97. Isaeva, V. V., Pushchina, E. V. & Karetin, Yu. A. The Quasi-Fractal Structure of Fish Brain Neurons. *Russian Journal of Marine Biology* **30**, 127–134 (2004).

98. Kim, J. *et al.* Altered branching patterns of Purkinje cells in mouse model for cortical development disorder. *Scientific Reports* **1**, 122 (2011).

99. Ferrari, G. *et al.* Corneal confocal microscopy reveals trigeminal small sensory fiber neuropathy in amyotrophic lateral sclerosis. *Front. Aging Neurosci.* **6**, (2014).

100. Morigiwa, K., Tauchi, M. & Fukuda, Y. Fractal analysis of ganglion cell dendritic branching patterns of the rat and cat retinae. *Neuroscience Research Supplements* **10**, S131–S139 (1989).

101. Malcai, O., Lidar, D. A., Biham, O. & Avnir, D. Scaling range and cutoffs in empirical fractals. *Phys. Rev. E* **56**, 2817–2828 (1997).

102. Avnir, D., Biham, O., Lidar, D. & Malcai, O. Is the Geometry of Nature Fractal? *Science* **279**, 39–40 (1998).

103. Cogan, S. F. Neural Stimulation and Recording Electrodes. *Annual Review of Biomedical Engineering* **10**, 275–309 (2008).

104. Roach, P., Parker, T., Gadegaard, N. & Alexander, M. R. Surface strategies for control of neuronal cell adhesion: A review. *Surface Science Reports* **65**, 145–173 (2010).

105. Wang, K., Fishman, H. A., Dai, H. & Harris, J. S. Neural Stimulation with a Carbon Nanotube Microelectrode Array. *Nano Letters* **6**, 2043–2048 (2006).

106. Rousche, P. J. *et al.* Flexible polyimide-based intracortical electrode arrays with bioactive capability. *IEEE Trans Biomed Eng* **48**, 361–371 (2001).

107. Polikov, V. S., Tresco, P. A. & Reichert, W. M. Response of brain tissue to chronically implanted neural electrodes. *Journal of Neuroscience Methods* **148**, 1–18 (2005).

108. Kim, B. J. *et al.* 3D Parylene sheath neural probe for chronic recordings. *J. Neural Eng.* **10**, 045002 (2013).

109. Balgude, A. P., Yu, X., Szymanski, A. & Bellamkonda, R. V. Agarose gel stiffness determines rate of DRG neurite extension in 3D cultures. *Biomaterials* **22**, 1077–1084 (2001).

110. Flanagan, L. A., Ju, Y.-E., Marg, B., Osterfield, M. & Janmey, P. A. Neurite branching on deformable substrates. *Neuroreport* **13**, 2411–2415 (2002).

111. Fan, Y. W. *et al.* Adhesion of neural cells on silicon wafer with nano-topographic surface. *Applied Surface Science* **187**, 313–318 (2002).

112. Khan, S. P., Auner, G. G. & Newaz, G. M. Influence of nanoscale surface roughness on neural cell attachment on silicon. *Nanomedicine: Nanotechnology, Biology and Medicine* **1**, 125–129 (2005).

113. Gabay, T. *et al.* Electro-chemical and biological properties of carbon nanotube based multi-electrode arrays. *Nanotechnology* **18**, 035201 (2007).

114. Lin, C.-M., Lee, Y.-T., Yeh, S.-R. & Fang, W. Flexible carbon nanotubes electrode for neural recording. *Biosensors and Bioelectronics* **24**, 2791–2797 (2009).

115. Chen, Y.-C. *et al.* An active, flexible carbon nanotube microelectrode array for recording electrocorticograms. *Journal of Neural Engineering* **8**, 034001 (2011).

116. David-Pur, M., Bareket-Keren, L., Beit-Yaakov, G., Raz-Prag, D. & Hanein, Y. All-carbon-nanotube flexible multi-electrode array for neuronal recording and stimulation. *Biomedical Microdevices* **16**, 43–53 (2014).

117. Wong, E. W., Sheehan, P. E. & Lieber, C. M. Nanobeam Mechanics: Elasticity, Strength, and Toughness of Nanorods and Nanotubes. *Science* **277**, 1971–1975 (1997).

118. Cellot, G. *et al.* Carbon nanotubes might improve neuronal performance by favouring electrical shortcuts. *Nature Nanotechnology* **4**, 126–133 (2009).

119. Sorkin, R. *et al.* Process entanglement as a neuronal anchorage mechanism to rough surfaces. *Nanotechnology* **20**, 015101 (2009).

120. Nick, C., Yadav, S., Joshi, R., Thielemann, C. & Schneider, J. J. Growth and structural discrimination of cortical neurons on randomly oriented and vertically aligned dense carbon nanotube networks. *Beilstein Journal of Nanotechnology* **5**, 1575–1579 (2014).

121. Zhang, X. *et al.* Guided neurite growth on patterned carbon nanotubes. *Sensors and Actuators B: Chemical* **106**, 843–850 (2005).

122. Gabay, T., Jakobs, E., Ben-Jacob, E. & Hanein, Y. Engineered self-organization of neural networks using carbon nanotube clusters. *Physica A: Statistical Mechanics and its Applications* **350**, 611–621 (2005).

123. Mangione A, M. A. & Messina JC, B. L. Basic Research for Peripheral Neural Regeneration by CNTs, A Preliminary ‘in vitro’ Study. *Journal of Nanomedicine & Nanotechnology* **06**, (2015).

124. Johnen, S. *et al.* Properties of Retinal Precursor Cells Grown on Vertically Aligned Multiwalled Carbon Nanotubes Generated for the Modification of Retinal Implant-Embedded Microelectrode Arrays. *J Ophthalmol* **2016**, 2371021 (2016).

125. Mattson, M. P., Haddon, R. C. & Rao, A. M. Molecular functionalization of carbon nanotubes and use as substrates for neuronal growth. *Journal of Molecular Neuroscience* **14**, 175–182 (2000).

126. Liu, J. *et al.* Control of neuronal network organization by chemical surface functionalization of multi-walled carbon nanotube arrays. *Nanotechnology* **22**, 195101 (2011).

127. McKenzie, J. L., Waid, M. C., Shi, R. & Webster, T. J. Decreased functions of astrocytes on carbon nanofiber materials. *Biomaterials* **25**, 1309–1317 (2004).

128. Bareket, L. *et al.* Semiconductor Nanorod–Carbon Nanotube Biomimetic Films for Wire-Free Photostimulation of Blind Retinas. *Nano Lett.* **14**, 6685–6692 (2014).

129. Bareket-Keren, L. & Hanein, Y. Carbon nanotube-based multi electrode arrays for neuronal interfacing: progress and prospects. *Frontiers in Neural Circuits* **6**, (2013).

130. Fabbro, A., Bosi, S., Ballerini, L. & Prato, M. Carbon Nanotubes: Artificial Nanomaterials to Engineer Single Neurons and Neuronal Networks. *ACS Chem Neurosci* **3**, 611–618 (2012).

131. Voge, C. M. & Stegemann, J. Carbon nanotubes in neural interfacing applications. *Journal of neural engineering* **8**, 011001 (2011).

132. Pampaloni, N. P. *et al.* Sculpting neurotransmission during synaptic development by 2D nanostructured interfaces. *Nanomedicine: Nanotechnology, Biology and Medicine* **14**, 2521–2532 (2018).

133. Gabriel, G. *et al.* Easily made single-walled carbon nanotube surface microelectrodes for neuronal applications. *Biosensors and Bioelectronics* **24**, 1942–1948 (2009).

134. Shoval, A. *et al.* Carbon Nanotube Electrodes for Effective Interfacing with Retinal Tissue. *Frontiers in Neuroengineering* **2**, (2009).

135. Eleftheriou, C. G. *et al.* Carbon nanotube electrodes for retinal implants: A study of structural and functional integration over time. *Biomaterials* **112**, 108–121 (2017).

136. Watterson, W. J. *et al.* The Roles of an Aluminum Underlayer in the Biocompatibility and Mechanical Integrity of Vertically Aligned Carbon Nanotubes for Interfacing with Retinal Neurons. *Micromachines (Basel)* **11**, (2020).

137. Craighead, H. G. *et al.* Chemical and topographical surface modification for control of central nervous system cell adhesion. *Biomedical Microdevices* **1**, 49–64 (1998).

138. Fan, Y. W. *et al.* Culture of neural cells on silicon wafers with nano-scale surface topography. *Journal of neuroscience methods* **120**, 17–23 (2002).

139. Yang, I. H., Co, C. C. & Ho, C.-C. Spatially controlled co-culture of neurons and glial cells. *Journal of Biomedical Materials Research Part A* **75A**, 976–984 (2005).

140. Xu, X. *et al.* A patterned recombinant human IgM guides neurite outgrowth of CNS neurons. *Sci Rep* **3**, (2013).

141. Amani, H. *et al.* Controlling Cell Behavior through the Design of Biomaterial Surfaces: A Focus on Surface Modification Techniques. *Advanced Materials Interfaces* **6**, 1900572 (2019).

142. Piret, G., Perez, M.-T. & Prinz, C. N. Support of Neuronal Growth Over Glial Growth and Guidance of Optic Nerve Axons by Vertical Nanowire Arrays. *ACS Appl. Mater. Interfaces* **7**, 18944–18948 (2015).

143. Zuidema, J. M., Gilbert, R. J. & Gottipati, M. K. Biomaterial Approaches to Modulate Reactive Astroglial Response. *CTO* **205**, 372–395 (2018).

144. Xie, C. *et al.* Noninvasive Neuron Pinning with Nanopillar Arrays. *Nano Letters* **10**, 4020–4024 (2010).

145. Zamani, F., Amani-Tehran, M., Latifi, M. & Shokrgozar, M. A. The influence of surface nanoroughness of electrospun PLGA nanofibrous scaffold on nerve cell adhesion and proliferation. *J Mater Sci: Mater Med* **24**, 1551–1560 (2013).

146. Blumenthal, N. R., Hermanson, O., Heimrich, B. & Shastri, V. P. Stochastic nanoroughness modulates neuron–astrocyte interactions and function via mechanosensing cation channels. *PNAS* **111**, 16124–16129 (2014).

147. Hu, H., Ni, Y., Montana, V., Haddon, R. C. & Parpura, V. Chemically Functionalized Carbon Nanotubes as Substrates for Neuronal Growth. *Nano Letters* **4**, 507–511 (2004).

148. Moshayedi, P. *et al.* The relationship between glial cell mechanosensitivity and foreign body reactions in the central nervous system. *Biomaterials* **35**, 3919–3925 (2014).

149. Chapman, C. A. R. *et al.* Nanoporous Gold as a Neural Interface Coating: Effects of Topography, Surface Chemistry, and Feature Size. *ACS Appl. Mater. Interfaces* **7**, 7093–7100 (2015).

150. Georges, P. C., Miller, W. J., Meaney, D. F., Sawyer, E. S. & Janmey, P. A. Matrices with Compliance Comparable to that of Brain Tissue Select Neuronal over Glial Growth in Mixed Cortical Cultures. *Biophys J* **90**, 3012–3018 (2006).

151. Chapman, C. A. R., Chen, H., Stamou, M., Lein, P. J. & Seker, E. Mechanisms of Reduced Astrocyte Surface Coverage in Cortical Neuron-Glia Co-cultures on Nanoporous Gold Surfaces. *Cel. Mol. Bioeng.* **9**, 433–442 (2016).

152. Yiannakou, C. *et al.* Cell patterning via laser micro/nano structured silicon surfaces. *Biofabrication* **9**, 025024 (2017).

153. Ereifej, E. S. *et al.* Nanopatterning effects on astrocyte reactivity. *Journal of Biomedical Materials Research Part A* **101A**, 1743–1757 (2013).

154. Pajkossy, T. Electrochemistry at fractal surfaces. *Journal of Electroanalytical Chemistry and Interfacial Electrochemistry* **300**, 1–11 (1991).

155. Schulte, C. *et al.* Scale Invariant Disordered Nanotopography Promotes Hippocampal Neuron Development and Maturation with Involvement of Mechanotransductive Pathways. *Front Cell Neurosci* **10**, (2016).

156. Krukiewicz, K. *et al.* Fractal form PEDOT/Au assemblies as thin-film neural interface materials. *Biomed. Mater.* **13**, 054102 (2018).

157. Gentile, F. *et al.* Selective modulation of cell response on engineered fractal silicon substrates. *Scientific Reports* **3**, (2013).

158. Stoica, I., Barzic, A. I., Butnaru, M., Doroftei, F. & Hulubei, C. Surface topography effect on fibroblasts population on epiclon-based polyimide films. *Journal of Adhesion Science and Technology* **29**, 2190–2207 (2015).

159. Piret, G., Perez, M.-T. & Prinz, C. N. Neurite outgrowth and synaptophysin expression of postnatal CNS neurons on GaP nanowire arrays in long-term retinal cell culture. *Biomaterials* **34**, 875–887 (2013).

160. Sharma, R. K. & Netland, P. A. Early born lineage of retinal neurons express class III β-tubulin isotype. *Brain Research* **1176**, 11–17 (2007).

161. Zalis, M. C., Johansson, S. & Englund-Johansson, U. Immunocytochemical Profiling of Cultured Mouse Primary Retinal Cells. *J Histochem Cytochem* **65**, 223–239 (2017).

162. Radio, N. M. & Mundy, W. R. Developmental neurotoxicity testing in vitro: Models for assessing chemical effects on neurite outgrowth. *NeuroToxicology* **29**, 361–376 (2008).

163. Harrill, J. A., Robinette, B. L., Freudenrich, T. & Mundy, W. R. Use of high content image analyses to detect chemical-mediated effects on neurite sub-populations in primary rat cortical neurons. *NeuroToxicology* **34**, 61–73 (2013).

164. Wu, C., Schulte, J., Sepp, K. J., Littleton, J. T. & Hong, P. Automatic Robust Neurite Detection and Morphological Analysis of Neuronal Cell Cultures in High-content Screening. *Neuroinformatics* **8**, 83–100 (2010).

165. Gautam, V. *et al*. Engineering Highly Interconnected Neuronal Networks on Nanowire Scaffolds. *Nano Letters* (2017) doi:10.1021/acs.nanolett.6b05288.

166. Edmondson, J. C. & Hatten, M. E. Glial-guided granule neuron migration in vitro: a high-resolution time- lapse video microscopic study. *J. Neurosci.* **7**, 1928–1934 (1987).

167. Komuro, H. & Rakic, P. Modulation of neuronal migration by NMDA receptors. *Science* **260**, 95–97 (1993).

168. Schaar, B. T. & McConnell, S. K. Cytoskeletal coordination during neuronal migration. *PNAS* **102**, 13652–13657 (2005).

169. Nichols, A. J., Carney, L. H. & Olson, E. C. Comparison of slow and fast neocortical neuron migration using a new in vitro model. *BMC Neurosci* **9**, 50 (2008).

170. Fields, R. D. & Stevens-Graham, B. New Insights into Neuron-Glia Communication. *Science* **298**, 556–562 (2002).

171. Shein, M. *et al*. Engineered neuronal circuits shaped and interfaced with carbon nanotube microelectrode arrays. *Biomed Microdevices* **11**, 495–501 (2009).

172. Villegas, J. C. *et al*. Multiwalled Carbon Nanotubes Hinder Microglia Function Interfering with Cell Migration and Phagocytosis. *Advanced Healthcare Materials* **3**, 424–432 (2014).

173. Hatten, M. E. & Mason, C. A. Mechanisms of glial-guided neuronal migration in vitro and in vivo. 11 (1990) doi:10.1007/BF01939383.

174. Fishell, G. & Hatten, M. E. Astrotactin provides a receptor system for CNS neuronal migration. *Development* **113**, 755–765 (1991).

175. Delivopoulos, E. & Murray, A. F. Controlled Adhesion and Growth of Long Term Glial and Neuronal Cultures on Parylene-C. *PLOS ONE* **6**, e25411 (2011).

176. Fletcher, D. A. & Theriot, J. A. An introduction to cell motility for the physical scientist. *Phys Biol* **1**, T1-10 (2004).

177. Ananthakrishnan, R. & Ehrlicher, A. The Forces Behind Cell Movement. *Int J Biol Sci* **3**, 303–317 (2007).

178. Steinmetz, C., Buard, I., Claudepierre, T., Naegler, K. & W Pfrieger, F. Regional variations in the glial influence on synapse development in the mouse CNS. *The Journal of physiology* **577**, 249–61 (2006).

179. Bringmann, A. *et al*. Müller cells in the healthy and diseased retina. *Progress in Retinal and Eye Research* **25**, 397–424 (2006).

180. Alexei Verkhratsky & Butt, A. Morphology of Glial Cells. in *Glial Neurobiology* 21–28 (John Wiley & Sons, Ltd, 2007). doi:10.1002/9780470517796.ch3.

181. Vecino, E., Rodriguez, F. D., Ruzafa, N., Pereiro, X. & Sharma, S. C. Glia–neuron interactions in the mammalian retina. *Progress in Retinal and Eye Research* **51**, 1–40 (2016).

182. Shi, M. *et al.* Glia co-culture with neurons in microfluidic platforms promotes the formation and stabilization of synaptic contacts. *Lab on a Chip* **13**, 3008–3021 (2013).

183. Oppenheim, R. W. Cell Death During Development of the Nervous System. *Annual Review of Neuroscience* **14**, 453–501 (1991).

184. Chaum, E. Retinal neuroprotection by growth factors: A mechanistic perspective. *Journal of Cellular Biochemistry* **88**, 57–75 (2003).

185. Scott-Solomon, E., Boehm, E. & Kuruvilla, R. The sympathetic nervous system in development and disease. *Nat Rev Neurosci* **22**, 685–702 (2021).

186. Bosi, S. *et al.* Carbon based substrates for interfacing neurons: Comparing pristine with functionalized carbon nanotubes effects on cultured neuronal networks. *Carbon* **97**, 87–91 (2016).

187. Dowell-Mesfin, N. M. *et al.* Topographically modified surfaces affect orientation and growth of hippocampal neurons. *Journal of Neural Engineering* **1**, 78–90 (2004).

188. Moore, S. W. & Sheetz, M. P. Biophysics of substrate interaction: influence on neural motility, differentiation and repair. *Dev Neurobiol* **71**, 1090–1101 (2011).

189. Bassett, E. A. & Wallace, V. A. Cell fate determination in the vertebrate retina. *Trends in Neurosciences* **35**, 565–573 (2012).

190. Chen, X. *et al.* Evidence for a retinal progenitor cell in the postnatal and adult mouse. *Stem Cell Research* **23**, 20–32 (2017).

191. Ming, G. & Song, H. Adult Neurogenesis in the Mammalian Central Nervous System. *Annual Review of Neuroscience* **28**, 223–250 (2005).

192. Christopherson, G. T., Song, H. & Mao, H.-Q. The influence of fiber diameter of electrospun substrates on neural stem cell differentiation and proliferation. *Biomaterials* **30**, 556–564 (2009).

193. Chang, J. C., Brewer, G. J. & Wheeler, B. C. Neuronal network structuring induces greater neuronal activity through enhanced astroglial development. *J. Neural Eng.* **3**, 217–226 (2006).

194. Nam, Y., Brewer, G. J. & Wheeler, B. C. Development of astroglial cells in patterned neuronal cultures. *Journal of Biomaterials Science -- Polymer Edition* **18**, 1091–1100 (2007).

195. Bringmann, A. *et al.* Cellular signaling and factors involved in Müller cell gliosis: Neuroprotective and detrimental effects. *Progress in Retinal and Eye Research* **28**, 423–451 (2009).

196. Ramírez, A. I. *et al.* Quantification of the Effect of Different Levels of IOP in the Astroglia of the Rat Retina Ipsilateral and Contralateral to Experimental Glaucoma. *Investigative Ophthalmology & Visual Science* **51**, 5690–5696 (2010).

197. Keeley, P. W., Patel, S. S. & Reese, B. E. Cell numbers, cell ratios, and developmental plasticity in the rod pathway of the mouse retina. *J Anat* (2022) doi:10.1111/joa.13653.

198. von Bartheld, C. S., Bahney, J. & Herculano-Houzel, S. The search for true numbers of neurons and glial cells in the human brain: A review of 150 years of cell counting. *J Comp Neurol* **524**, 3865–3895 (2016).

199. de Hoz, R. *et al.* Retinal Macroglial Responses in Health and Disease. *Biomed Res Int* **2016**, 2954721 (2016).

200. Turner, J. N. *et al.* Cerebral Astrocyte Response to Micromachined Silicon Implants. *Experimental Neurology* **156**, 33–49 (1999).

201. Westermark, B. Growth control in miniclones of human glial cells. *Experimental Cell Research* **111**, 295–299 (1978).

202. Raos, B. J. *et al.* Patterning of functional human astrocytes onto parylene-C/SiO2substrates for the study of Ca2+ dynamics in astrocytic networks. *J. Neural Eng.* **15**, 036015 (2018).

203. Jordan, M. D. *et al.* Human astrocytic grid networks patterned in parylene-C inlayed SiO2 trenches. *Biomaterials* **105**, 117–126 (2016).

204. Marconi, E. *et al.* Emergent Functional Properties of Neuronal Networks with Controlled Topology. *PLOS ONE* **7**, e34648 (2012).

205. Neurolucida | Neuron Tracing Software | MBF Bioscience. https://www.mbfbioscience.com/neurolucida.

206. Altmann, S. L. *Rotations, Quaternions, and Double Groups*. (Oxford University Press, 1986).

207. Richardson, L. F. The problem of contiguity : An appendix to statistics of deadly quarrels. *General Systems Yearbook* **6**, 139 (1961).

208. Wen, Q., Stepanyants, A., Elston, G. N., Grosberg, A. Y. & Chklovskii, D. B. Maximization of the connectivity repertoire as a statistical principle governing the shapes of dendritic arbors. *Proceedings of the National Academy of Sciences* **106**, 12536–12541 (2009).

209. Milosević, N. T., Ristanović, D. & Stanković, J. B. Fractal analysis of the laminar organization of spinal cord neurons. *J Neurosci Methods* **146**, 198–204 (2005).

210. Mark, de B., M, van K., Overmars, M. & Schwarzkopf, O. *Computational Geometry: Algorithms and Applications, Second Edition*. (Springer, 2000).

211. Wheeler, D. W. *et al.* Hippocampome.org: a knowledge base of neuron types in the rodent hippocampus. *eLife* **4**,.

212. Gregory, M. J., Kimerling, A. J., White, D. & Sahr, K. A comparison of intercell metrics on discrete global grid systems. *Computers, Environment and Urban Systems* **32**, 188–203 (2008).

213. González, Á. Measurement of areas on a sphere using Fibonacci and latitude-longitude lattices. *Math Geosci* **42**, 49–64 (2010).

214. Murray, J. D. Use and abuse of fractal theory in neuroscience. *The Journal of Comparative Neurology* **361**, 369–371 (1995).

215. Vormberg, A., Effenberger, F., Muellerleile, J. & Cuntz, H. Universal features of dendrites through centripetal branch ordering. *PLOS Computational Biology* **13**, e1005615 (2017).

216. Ledderose, J., Sención, L., Salgado, H., Arias-Carrión, O. & Treviño, M. A software tool for the analysis of neuronal morphology data. *Int Arch Med* **7**, 6 (2014).

217. OGATA, Y. & KATSURA, K. Maximum likelihood estimates of the fractal dimension for random spatial patterns. *Biometrika* **78**, 463–474 (1991).

218. Hart, W. E., Goldbaum, M., Côté, B., Kube, P. & Nelson, M. R. Measurement and classification of retinal vascular tortuosity. *International Journal of Medical Informatics* **53**, 239–252 (1999).

219. Bullitt, E., Gerig, G., Pizer, S. M., Lin, W. & Aylward, S. R. Measuring Tortuosity of the Intracerebral Vasculature from MRA Images. *IEEE Trans Med Imaging* **22**, 1163–1171 (2003).

220. Lorthois, S., Lauwers, F. & Cassot, F. Tortuosity and other vessel attributes for arterioles and venules of the human cerebral cortex. *Microvascular Research* **91**, 99–109 (2014).

221. Barbará-Morales, E., Pérez-González, J., Rojas-Saavedra, K. C. & Medina-Bañuelos, V. Evaluation of Brain Tortuosity Measurement for the Automatic Multimodal Classification of Subjects with Alzheimer's Disease. *Computational Intelligence and Neuroscience* **2020**, e4041832 (2020).

222. Sholl, D. A. Dendritic organization in the neurons of the visual and motor cortices of the cat. *J Anat* **87**, 387-406.1 (1953).

223. Fernández, E., Bolea, J. A., Ortega, G. & Louis, E. Are neurons multifractals? *Journal of Neuroscience Methods* **89**, 151–157 (1999).

224. Jelinek, H. F., Milošević, N. T., Karperien, A. & Krstonošić, B. Box-Counting and Multifractal Analysis in Neuronal and Glial Classification. in *Advances in Intelligent Control Systems and Computer Science* (ed. Dumitrache, L.) vol. 187 177–189 (Springer Berlin Heidelberg, 2013).

225. West, G. B., Brown, J. H. & Enquist, B. J. A General Model for the Origin of Allometric Scaling Laws in Biology. *Science* **276**, 122–126 (1997).

226. Hill, S. L., Wang, Y., Riachi, I., Schürmann, F. & Markram, H. Statistical connectivity provides a sufficient foundation for specific functional connectivity in neocortical neural microcircuits. *PNAS* **109**, E2885–E2894 (2012).

227. Ooyen, A. van *et al.* Independently Outgrowing Neurons and Geometry-Based Synapse Formation Produce Networks with Realistic Synaptic Connectivity. *PLOS ONE* **9**, e85858 (2014).

228. McAssey, M. P. *et al.* A Morpho-Density Approach to Estimating Neural Connectivity. *PLoS ONE* **9**, e86526 (2014).

229. Stepanyants, A. & Chklovskii, D. Neurogeometry and potential synaptic connectivity. *Trends in Neurosciences* **28**, 387–394 (2005).

230. Kalisman, N., Silberberg, G. & Markram, H. Deriving physical connectivity from neuronal morphology. *Biological Cybernetics* **88**, 210–218 (2003).

231. Wen, Q., Stepanyants, A., Elston, G. N., Grosberg, A. Y. & Chklovskii, D. B. Maximization of the connectivity repertoire as a statistical principle governing the shapes of dendritic arbors. *Proceedings of the National Academy of Sciences* **106**, 12536–12541 (2009).

232. Banavar, J. R., Maritan, A. & Rinaldo, A. Size and form in efficient transportation networks. *Nature* **399**, 130–132 (1999).

233. Banker, G. & Goslin, K. *culturing nerve cells*. (Bradford Book, 1998).

234. Woiterski, L., Claudepierre, T., Luxenhofer, R., Jordan, R. & Käs, J. A. Stages of neuronal network formation. *New J. Phys.* **15**, 025029 (2013).

235. Santos-Sierra, D. de *et al.* Emergence of Small-World Anatomical Networks in Self-Organizing Clustered Neuronal Cultures. *PLOS ONE* **9**, e85828 (2014).

236. Piret, G., Perez, M.-T. & Prinz, C. N. Neurite outgrowth and synaptophysin expression of postnatal CNS neurons on GaP nanowire arrays in long-term retinal cell culture. *Biomaterials* **34**, 875–887 (2013).

237. Owen, G. R., Meredith, D. O., ap Gwynn, I. & Richards, R. G. Focal adhesion quantification - a new assay of material biocompatibility? Review. *Eur Cell Mater* **9**, 85–96; discussion 85-96 (2005).

238. Li, M. & Sakaguchi, D. S. Expression patterns of focal adhesion associated proteins in the developing retina. *Developmental Dynamics* **225**, 544–553 (2002).

239. Latora, V. & Marchiori, M. Economic small-world behavior in weighted networks. *Eur. Phys. J. B* **32**, 249–263 (2003).

240. Achard, S. & Bullmore, E. Efficiency and cost of economical brain functional networks. *PLoS Comput. Biol.* **3**, e17 (2007).

241. Watterson, W. J., Montgomery, R. D. & Taylor, R. P. Fractal Electrodes as a Generic Interface for Stimulating Neurons. *Scientific Reports* **7**, (2017).

242. Watterson, W. J., Montgomery, R. D. & Taylor, R. P. Modeling the Improved Visual Acuity Using Photodiode Based Retinal Implants Featuring Fractal Electrodes. *Frontiers in Neuroscience* **12**, (2018).

243. Mufson, E. J. *et al.* Hippocampal Plasticity During the Progression of Alzheimer's disease. *Neuroscience* **309**, 51–67 (2015).

244. Rowland, C. *et al.* Investigating Fractal Analysis as a Diagnostic Tool That Probes the Connectivity of Hippocampal Neurons. *Front Physiol* **13**, 932598 (2022).

245. Berning, M., Boergens, K. M. & Helmstaedter, M. SegEM: Efficient Image Analysis for High-Resolution Connectomics. *Neuron* **87**, 1193–1206 (2015).

246. Ascoli, G. A., Donohue, D. E. & Halavi, M. NeuroMorpho.Org: A Central Resource for Neuronal Morphologies. *J. Neurosci.* **27**, 9247–9251 (2007).